Very Large Telescope observations of nearby dwarf irregular galaxies

A dissertation submitted to the University of Manchester
for the degree of Master of Science by Research
in the Faculty of Science and Engineering

2017

By
Nicholas James Amos
School of Physics and Astronomy

Contents

List of Tables

List of Figures

The University of Manchester

ABSTRACT OF a dissertation submitted by Nicholas James Amos
for the Degree of Master of Science by Research and entitled
"Very Large Telescope observations of nearby dwarf irregular galaxies"
September 2017

Observations of the Local Group dwarf irregular galaxies Aquarius dIrr, IC 1613, LGS 3, NGC 6822, Pegasus dIrr, Phoenix dIrr, Sagittarius dIrr, and WLM were made, using the Visible Multi-Object Spectrograph (VIMOS) on the Very Large Telescope (VLT). The data consists of 198 V and 192 I-band images. A photometric point-source catalogue was made from 186 of these image pairs, with aperture photometry performed using a combination of PYTHON, ESOREX and SEXTRACTOR. Astrometric and photometric corrections were determined using the produced catalogue and external datasets.

For these eight dwarf irregular galaxies there were 241,999 source detections. The sensitivity limit was estimated to be $V \sim 24$ mag and $I \sim 22$ mag, in terms of depth: these observations are among the most sensitive of their type. Colour-magnitude diagrams were generated and relevant isochrones overlain to highlight stellar populations. The VLT data were also crossmatched with 3.6 and 4.5 μm *Spitzer* data from the DUSTiNGS survey's Good Source Catalogue. 68 DUSTiNGS variable sources were located in the VLT catalogue, with some notable variation in magnitudes, which was attributed to the large variability of these sources. Two of the variable sources located in the VLT catalogue for IC 1613 were found in a dataset from Menzies, Whitelock & Feast (2015).

This catalogue will be useful for those studying metal-poor environments and analogues for the early Universe. This data will also be useful for follow up studies attempting to separate carbon and oxygen-rich stars and studies using the upcoming *James Webb Space Telescope*.

Declaration

No portion of the work referred to in this dissertation has been submitted in support of an application for another degree or qualification of this or any other university or other institution of learning.

Copyright

Acknowledgements

I would like to thank my ever patient supervisor, Iain McDonald, for his increadibly useful guidance and advice which has helped to guide my career as a researcher. I would also like to thank the JBCA and the Univeristy of Manchester for their welcome during this year of study. They provided an intellectually creative atmosphere and a productive environment to work in the chaos of the outside world.

Finally, I would like to thank the people who provided emotional support during this challenging year. My partner, Emily, who was always there to listen even though I may have been talking complete nonsense. My parents and family who always offered a reasoned point of view to difficult situations. Last but not least I would like to thank my dog, Barney, whose perky attitude never failed to brighten my day.

The probability of success is difficult to estimate;

but if we never search the chance of success is zero.

– Giuseppe Cocconi and Philip Morrison

Chapter 1

Introduction

As a key contributor to the enrichment of metals of the interstellar medium (ISM), it is important to improve our understanding of the Asymptotic Giant Branch (AGB) (Karakas & Lattanzio 2014). The Universe has been evolving from a metal-poor to a more metal-rich state. Metal-poor stars are not abundant in our solar neighbourhood, meaning they are poorly studied. Yet, metal-poor stars are an important analogue, because they can help us to understand how stellar evolution is different at lower metallicity when compared to solar metallicity. Investigating stellar evolution at low metallicity can allow us to understand the physics of the early Universie when metallicity was poor. Dwarf galaxies are the most common type of galaxies in the Universe (Mateo 1998) and Dwarf irregular galaxies contain abundant metal-poor populations, that represent the early Universe, where stars can be individually resolved. A case will be made for the importance of observing these galaxies and a catalogue of stars will be produced for eight dwarf irregular galaxies.

1.1 Dwarf Galaxies

1.1.1 Metal-Poor Environments

The only environments that come to mind to observe the early Universe are high-redshift galaxies, especially when considering the extreme case of the first stars (population III stars). However, these are very poorly resolved, especially when considering individual stars. For example, it is often the case that the collective luminosity of a galaxy will obscure the light from individual stars. In attempting to probe deeper into the universe there has been observations of stars that are separate to galaxies or present in the intercluster medium. One such example is SDSS J122952.66+112227.8 which is a possible Blue Supergiant that has been spectroscopically resolved present in the trail of IC 3418, approximately 16.5 Mpc distant (Ohyama & Hota 2013). The spectra in this work is compared directly with the Sloan Digital Sky Survey (SDSS) images and it is clearly shown that in most of the photometric images the object is poorly resolved if at all.

It also may be possible to use simulations of the early universe to further contrain our understanding of these early stars. However, simulations that have the scale necessary to probe this, such as EAGLE (Schaye et al. 2015), do not have the resolution down to individual stars and so the same problem occurs when attempting to observe high-redshift galaxies. This is often due to a limitation on computer processing power and as the hardware becomes available this may become possible in the future.

In terms of understanding stellar evolution in the early Universe, we consider stars in stages of early chemical evolution i.e. those stars that have not been enriched by the metals produced by the stars that came before them. Fortunately, metal-poor conditions exist in the local Universe where these stars are easily resolvable and meaningful observations can be made.

The main aim of this project is to produce a catalogue of stars in the eight nearby dwarf irregular galaxies listed in Section 1.1.2. It is hoped that this catalogue of resolved point sources will provide an analogue to stars at high-redshift so that meaningful studies may be made of metal-poor environments. It may also be useful as a source for spectrosopic follow-up of specific groups of sources.

1.1.2 Classification of Dwarf Galaxies

There are three main types of dwarf galaxy found in the Local Group. These are; Dwarf Irregular (dIrr), Dwarf Spheroidal (dSph), and Dwarf Elliptical (dE). There are differences between these galaxy types beyond their obvious shapes and basic information on examples of these galaxy types can be found in Table 1.1.

Dwarf galaxies in general are, by definition, low-luminosity and metal-poor (Chattopadhyay et al. 2015). Despite their large abundance when comapred to other galaxy types we still know relatively little about their formaiton. It has been suggested that some dwarf galaxies may form as a result of galaxy collisions as they have been observed in the tidal tails of such collisions (Chattopadhyay et al. 2015). There is ongoing debate as to the morphological evolution realtioship between dIrr and dSph galaxys, if one exists (Grebel, Gallagher III & Harbeck 2003). It is clear that the dIrr galaxies are undergoing much slower cehmcial evolution compared to their dSph counter-parts (Grebel, Gallagher III & Harbeck 2003; Hunter & Elmegreen 2004). It is also theorised that dIrr galaxies may have been the first galaxies to have formed and became the basis of larger galaxies formation (Hunter & Elmegreen 2004). The average metallicity of local dIrr galaxies is approximately [Fe/H] = –1.9 to –1.0 *dex* (Boyer et al. 2015b). This makes them useful analogues for the early Universe where metal content was poor. Using observations of these environments we can see how the early Universe evolved from a metal-poor state to the metal abundances seen in later generations of stars (Boyer et al. 2009).

Table 1.1: Comparative Properties of selected Dwarf Galaxies in the Local Group. Data taken from Mateo (1998), Han et al. (1997), de Boer et al. (2012) and de Boer et al. (2014).

Name	Galaxy Type	Distance (*kpc*)	Bulk [Fe/H] (*dex*)	Star-formation rate ($M_\odot$ year^{-1})	Total Mass (10^6 $M_\odot$)
NGC 6822	Irregular (dIrr)	490 ± 40	-1.2 ± 0.3	0.06	1640
WLM	Irregular (dIrr)	925 ± 40	-1.5 ± 0.2	0.003	150
Fornax	Spheroidal (dSph)	138 ± 8	-1.3 ± 0.2	$\sim 2 \times 10^{-4}$	68
Carina	Spheroidal (dSph)	101 ± 5	-2.0 ± 0.2	$\sim 0.25 \times 10^{-4}$	13
NGC 147	Elliptical (dE)	725 ± 40	-1.1 ± 0.2	0.0	110
NGC 185	Elliptical (dE)	620 ± 25	-1.22 ± 0.15	0.0	130

The Asymptotic Giant Branch (AGB) stage of stellar evolution is not well understood in metal-poor stars. These galaxies contain the largest metal-poor AGB populations when compared to other local star-forming galaxies (Boyer et al. 2015b). The following dIrr galaxies are described briefly as these will be the focus of this study. These galaxies were chosen because of these factors and based upon their relative isolation from other galaxies.

1.1.3 Phoenix dIrr

The Phoenix dIrr galaxy is approximately 0.42 ± 0.06 Mpc distant (Tully et al. 2013). This galaxy has a mean [Fe/H] $= -1.87 \pm 0.06$ dex (Hidalgo et al. 2009). This value of [Fe/H] is in good agreement with most measurements in previous work, with some discrepancy most likely due to a sign error in calculations (Hidalgo et al. 2009).

This galaxy has had a star formation rate of $1.39 \times 10^{-9} \pm 0.01 \times 10^{-9} M_{\odot} yr^{-1} pc^{-2}$ star formation that has been gradually slowing for approximately 10.6 Gyr (Hidalgo et al. 2009). The colour-magnitude diagram (CMD) for Phoenix dIrr is shown in Figure 1.1 (see section 1.2 for specific description of features).

1.1.4 Aquarius dIrr

The distance to the Aquarius dIrr galaxy is $\sim 1.01 \pm 0.08$ Mpc (Tully et al. 2013). Its mean [Fe/H] $= -1.44 \pm 0.03$ dex (Kirby et al. 2013). This galaxy is isolated from many of the other galaxies in the Local Group, therefore it is unlikely to have undergone tidal interaction (Cole et al. 2014). The CMD for Aquarius is shown in Figure 1.2. Aquarius has seen a large delay in star formation, which increased dramatically $\simeq 6 - 8$ Gyr ago and has slowly declined since then (Cole et al. 2014).

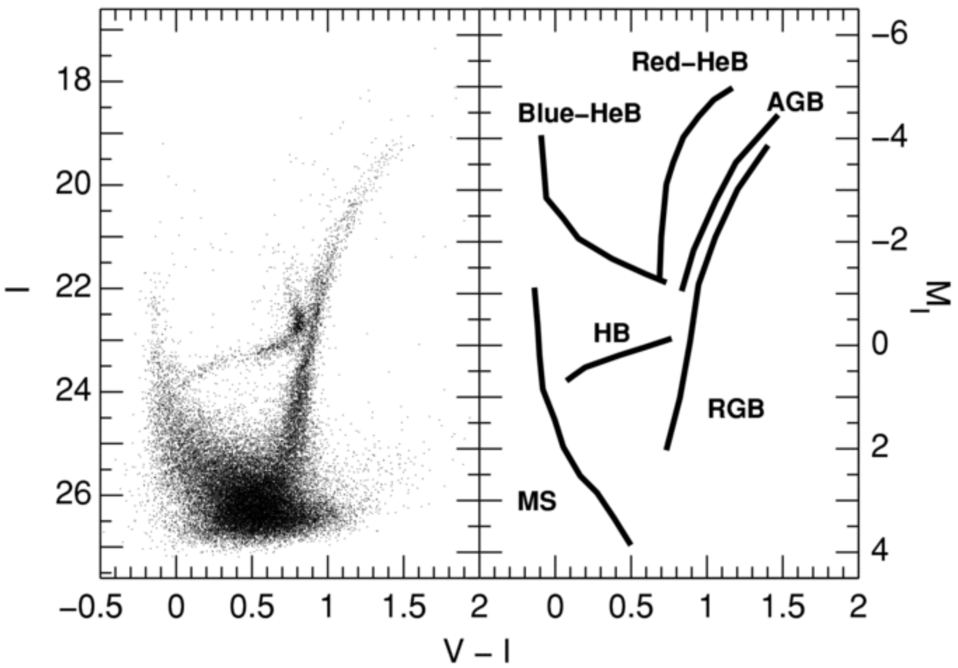

Figure 1.1: CMD for Phoenix dIrr. Also shown in the right panel are the main features of the CMD for convenience. Reproduced from Hidalgo et al. (2009).

1.1.5 Sagittarius dIrr

The Sagittarius dwarf irregular is at located 1.08 ± 0.1 Mpc away (Tully et al. 2013). Its approximate absolute magnitude is $\mathrm{M}_B^0 = -10.5$ (Young & Lo 1997). It is believed that the HI distribution in this galaxy is indicative of an unusual recent history (Young & Lo 1997). This is because the HI distribution is crescent shape so indicates an unusual recent evolution. It was found that this crescent shaped distribution of HI was not rotating together but was in fact two separate phases, a cold and warm phase. These two phases are receeding on both ends and approaching the middle (Young & Lo 1997). The cold phase shows evidence of star formation whereas the warm phase is too diffuse to do so. Sagittarius dIrr is the closest known galaxy to the Aquarius dIrr and as such is also isolated (Higgs et al. 2016). However, due to the large free-fall timescales of these galaxies it is unlikely any interaction between them has taken place. The CMD for Sagittarius dIrr is found in Figure 1.3.

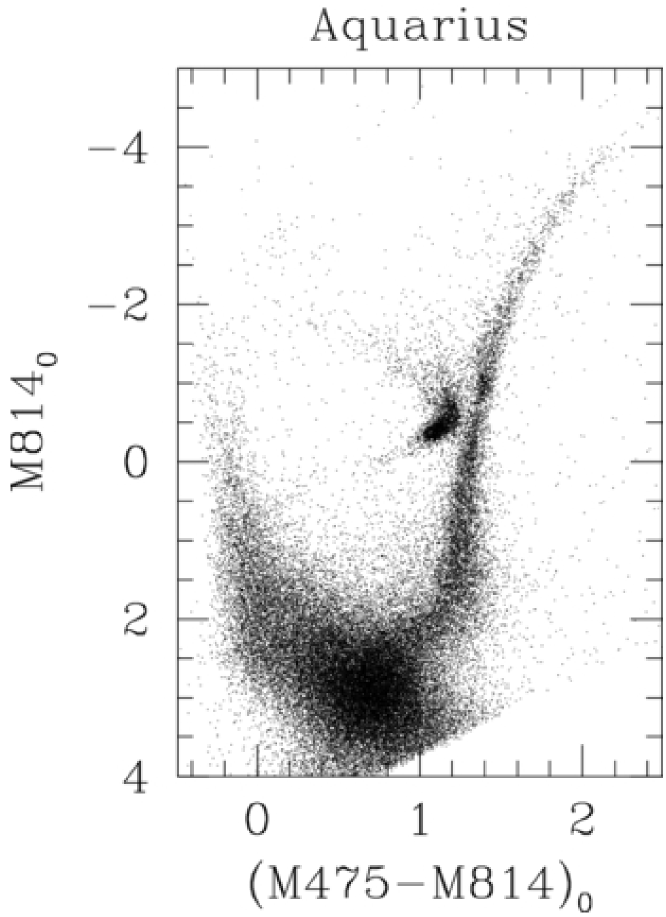

Figure 1.2: CMD for Aquarius dIrr. Reproduced from Cole et al. (2014).

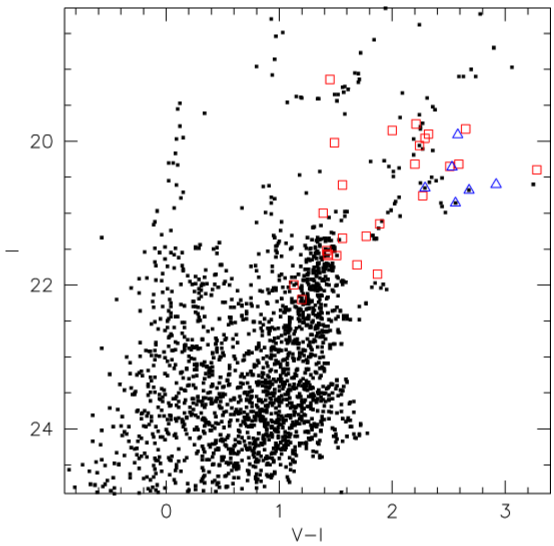

Figure 1.3: CMD for Sagittarius dIrr. The red squares and blue triangles indicate previously identified carbon stars. Reproduced from Momany et al. (2002).

1.1.6 WLM

WLM (Wolf-Lundmark-Melotte) resides at a distance of 932 ± 33 *kpc* (Tatton, Cioni & Irwin 2011). Due to this distance, and the distance to its nearest neighbour Cetus dSph at approximately 200 *kpc* away, WLM is one of the most isolated dIrrs in the Local Group (Leaman et al. 2009). Of stars detected in a photometric study in 2007, a C/M star ratio of 0.56 ± 0.12 was found, where C denotes carbon-rich and M denotes oxygen-rich AGB stars (Tatton, Cioni & Irwin 2011) (see section 1.3.1.5 for more information on carbon stars). However, this means that WLM has approximately twice as many oxygen rich stars than carbon stars. Tatton, Cioni & Irwin (2011) disagree with this value and suggest that this misagreement could be due to a high adoption of carbon stars in their foreground and sintead find values ranging from 0.36 to 1.43 for the inner region (Tatton, Cioni & Irwin 2011). As WLM is metal-poor, as are all the targets, it is unusual for it to have a high number of oxygen rich stars but these are likely clustered in the inner regions where most of the star formation is likely to have taken place.

1.1.7 LGS 3

LGS 3 is believed to be a transition dIrr/dSph (Grebel, Gallagher III & Harbeck 2003). These transition galaxies are important, as they show the internal changes that may occur between these two galaxy types and give more clues to how galaxies evolve over time. This galaxy has a star formation history (SFH) spanning at least 12 $Gyrs$ and shows a low recent star formation rate (SFR) (Hidalgo et al. 2011).

1.1.8 NGC 6822

The SFH of this dIrr has enhanced during the past $100 - 200$ Myr (Gallart et al. 1996). A CMD for NGC 6822 is shown in Figure 1.4. NGC 6822 is an active star forming galaxy with a $\sim 50\%$ gas mass fraction (Schruba et al. 2017). The galaxy has a SFR $\approx 0.015\ M_{\odot}yr^{-1}$ which is typical of a star-forming galaxy (Schruba et al. 2017).

1.1.9 IC 1613

IC 1613 is a gas-rich dIrr present in the Local Group (Dell'Agli et al. 2016) with a dynamical mass of $7.9 \times 10^{8}\ M_{\odot}$ and a HI gass mass of $6.3 \times 10^{7}\ M_{\odot}$ (Boyer et al. 2009). It is also easy to observe as there is little internal reddening and foreground contamination (Dell'Agli et al. 2016). There are large populations of AGB stars that are well studied and indeed there are ~ 200 carbon stars that have been identified (Dell'Agli et al. 2016). Figure 1.5 shows the population of AGB stars against a generated synthetic model for carbon and oxygen stars.

1.1.10 Pegasus dIrr

Figure 1.6 shows a Digitised Sky Survey (DSS) image for Pegasus dIrr. This dIrr has a comparable number of carbon stars to IC 1613 and WLM (Boyer et al. 2009). The Pegasus dIrr is also unusual as it can be seen to be rotating (Kirby et al. 2014).

1.2 Stellar Evolution

This section will lay out the stages of stellar evolution. Particular attention will be paid to the AGB. Many of the stages will be different depending on the metal content of the star. All of the stages laid out here will be concerned with low- to intermediate-mass stars.

1.2.1 Stellar Birth

Stars do not just come into being, they are formed by the condensation and collapse of molecular clouds within the interstellar medium (ISM). It is unlikely

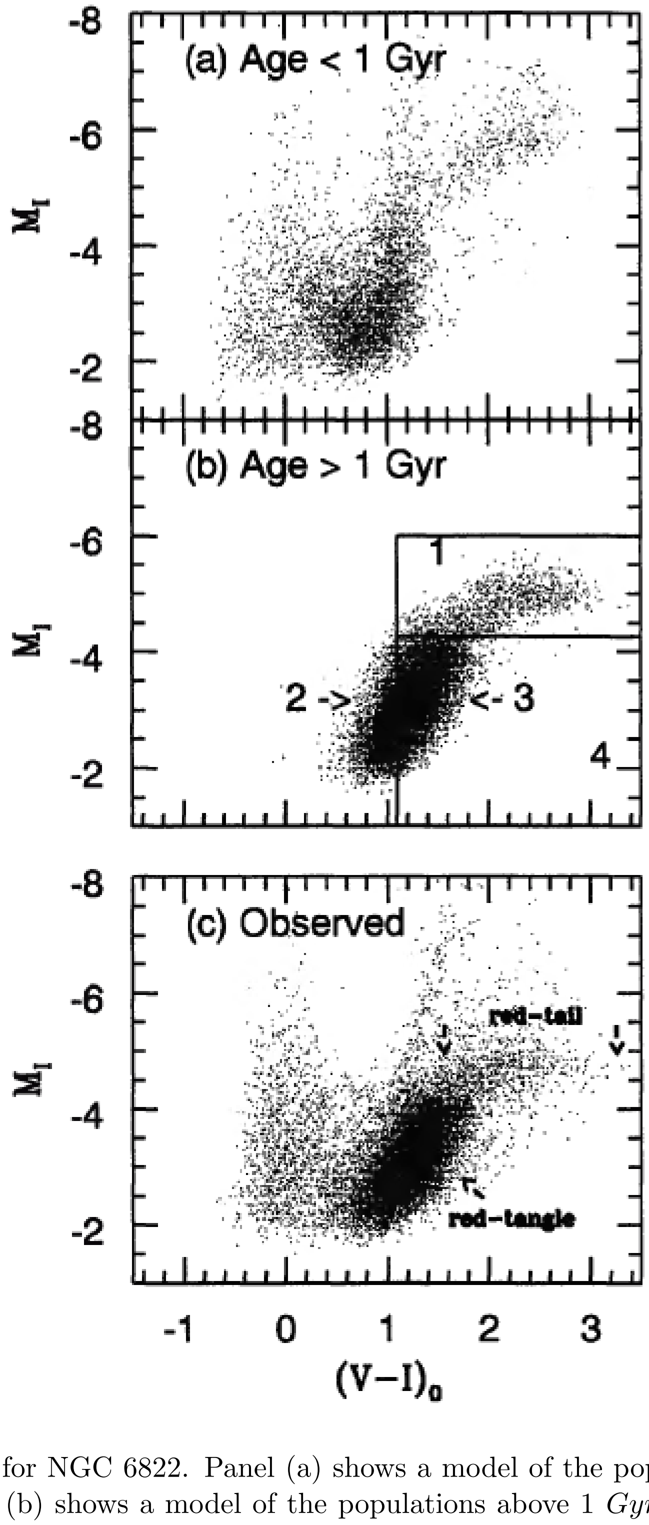

Figure 1.4: CMD for NGC 6822. Panel (a) shows a model of the populations of stars under 1 *Gyr* old. (b) shows a model of the populations above 1 *Gyrs* old. (c) shows the observed stellar populations of giant stars. Reproduced from Gallart et al. (1996).

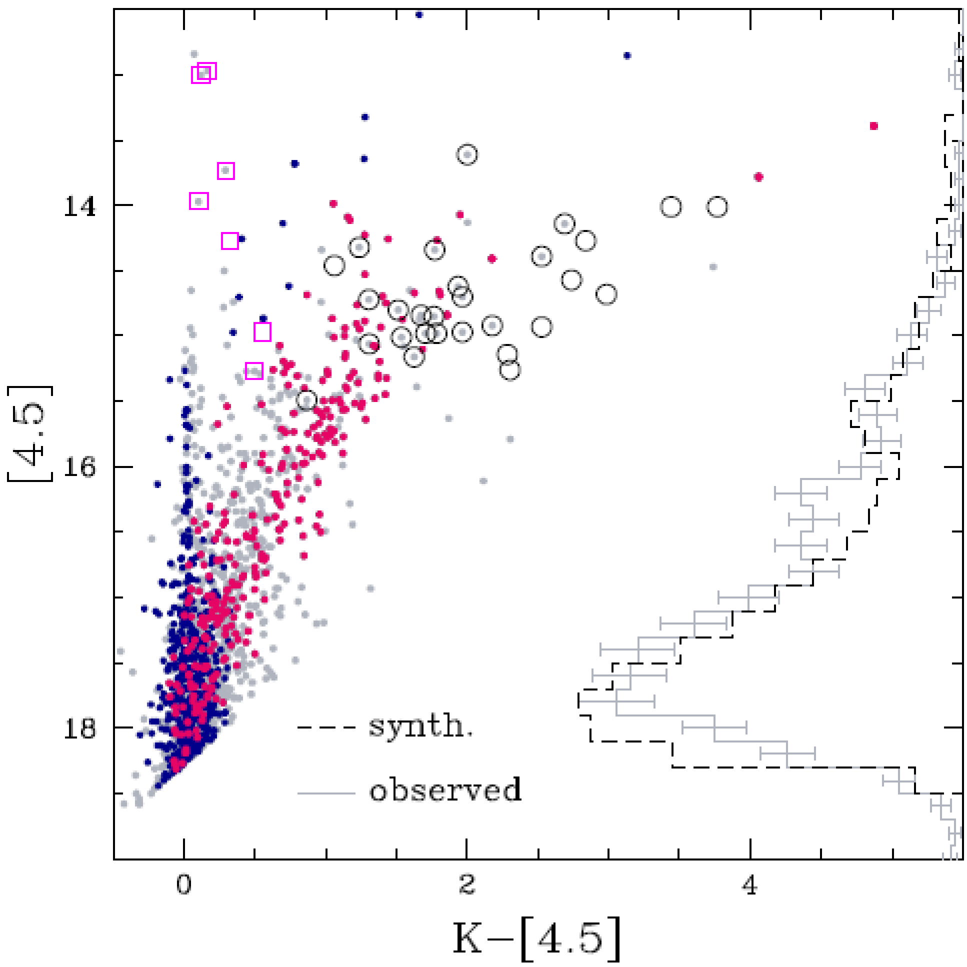

Figure 1.5: CMD for IC 1613. A sample of the population of AGB stars in IC 1613 are shown in grey. The stars shown in blue and red indicate synthetic O-rich and C-stars respectively. The histogram shows the distribution of the respective synthetic and observed populations. Reproduced from Dell'Agli et al. (2016).

that the whole cloud will collapse into one star. It is far more likely that, on partial collapse, the cloud will fragment and form smaller clumps of material which will have a range of masses, which may eventually accrete enough material to form individual stars (Prialnik 2009).

On collapse, the pressure and temperature in the core of the cloud will increase to the point where nuclear fusion can occur in the hydrogen present within the cloud. At this point, the clumps of interstellar matter have become protostars and will continue to collapse and heat up, increasing the radiation from the star

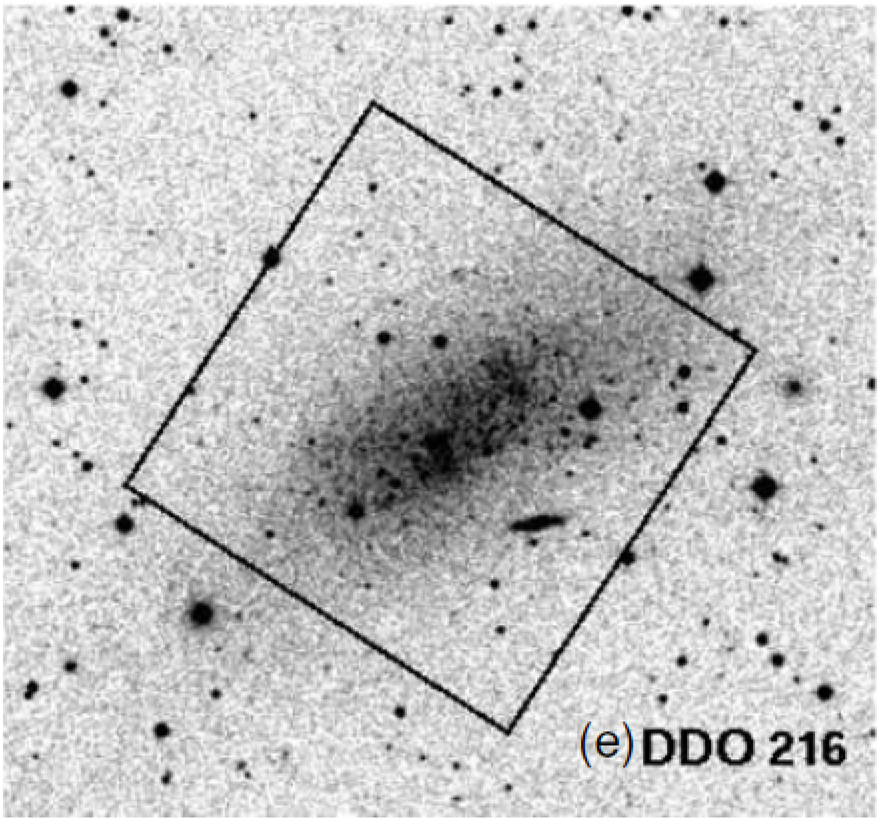

Figure 1.6: DSS image for Pegasus dIrr. Reproduced from Boyer et al. (2009).

(Prialnik 2009).

1.2.2 The Main Sequence

The transition from protostar to member of the main sequence (MS) is defined by the dominance of hydrogen fusion as the main source of energy for the star. For the stars discussed here, formation occurs on a timescale comparable to, but shorter than, the Kelvin–Helmholtz timescale (Prialnik 2009). If the mass of the contracting star exceeds $\sim 0.08\ M_{\odot}$, it becomes a zero-age main-sequence star (ZAMS). Once a star has reached this stage, it will remain on the MS for most of its life time. For a star with similar mass to our Sun this can be a MS time of the order 10^{10} yrs and, the larger the star, the shorter this lifetime (τ_{MS}) (Prialnik 2009):

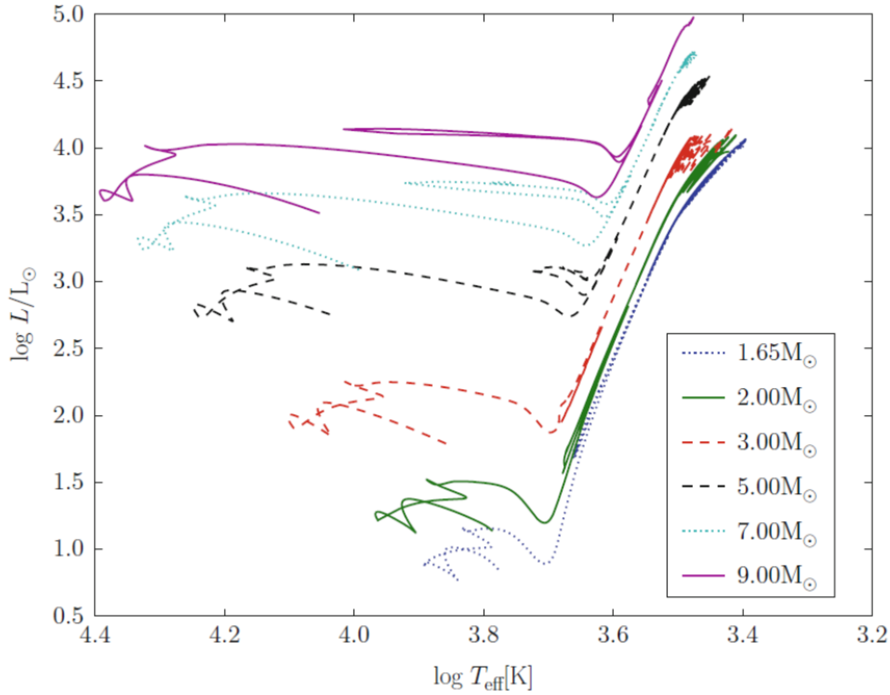

Figure 1.7: The tracks of various mass stars from the MS turnoff for stars with Z=0.02. Reproduced from Graham (2013).

$$\tau_{MS} \; \alpha \; \frac{M}{L} \; \alpha \; M^{-2}. \tag{1.1}$$

The position of a main-sequence star in the Hertzsprung-Russell diagram and any possible track it may take depends on its initial mass. The MS turnoff and later evolutionary stages for stars of various masses are shown in Figure 1.7 (for details on the specifics of each stage of stellar evolution see the remainder of Section 1.2).

1.2.2.1 Hydrogen Burning

Stars of different masses will process their hydrogen fuel in slightly different ways during their time on the MS. The tipping point for this change is $\sim$1.5 $M_\odot$.

For stars with $M < 1.5\ M_\odot$ the main fusion process is the proton-proton (p-p) chain, where hydrogen nuclei fuse to form helium nuclei via various isotopic pathways (Prialnik 2009).

Whereas, in stars with $M > 1.5\ M_{\odot}$, nuclear fusion mainly proceeds via the carbon-nitrogen-oxygen, CNO, cycle. This process has a secondary effect because the process uses these elements as catalysts for hydrogen fusion, which in turn slightly changes their relative abundances (Karakas & Lattanzio 2014).

1.2.2.2 Main-Sequence Nuclear Burning Processes

The burning processes that take place during the MS depend on the metal content of the star. For example, carbon burning will ignite at 8 $M_{\odot}$ with Z $\approx$ 0.014 but will occur at 7 $M_{\odot}$ at Z = 10^{-4} instead (Karakas & Lattanzio 2014). Here the burning processes are defined for Z $\approx$ 0.014.

1.2.3 The Red Giant Branch

The end of the MS phase is defined as the point where H burning in the core ends and starts to burn in a shell instead (Oswalt & Barstow 2013). This causes a contraction of the core due to the removal of the radiation pressure produced by H-core burning. However, due to the ignition of H-shell burning a new hydrostatic equilibrium must be established causing the outer layers to expand.

The star moves through its MS turn-off to the bottom of the RGB at almost constant luminosity during a timescale of $\sim 10^{6}$ yrs (Kippenhahn, Weigert & Weiss 2012). On entering the RGB the star cannot move any further to the right of the H–R diagram as this would mean entering the Hayashi forbidden zone.

Movement continues up the RGB until the hydrogen-burning shell reaches the boundary of the star's previously mixed material. At this point H-burning continues but with a reduced efficiency, causing a decrease in luminosity but also a slight increase in temperature. This point in the RGB is known as the RGB bump.

The position of the RGB bump is sensitive to a variety of conditions. For example a more metal-poor star will reach the RGB bump at the brighter part of the RGB compared to a more metal-rich counterpart (Valenti, Ferraro & Origlia 2004). Initial stellar mass is also important to consider as having an impact on RGB bump position as a higher initial mass will yield a star of higher luminosity and more rapid evolution. Therefore, its position may be used as an indication of the processes occurring in a star. A new equilibrium is reached and the star continues its track up the RGB. At this point the He-rich core is supported by electron degeneracy pressure and cannot be compressed. This, however, eventually breaks down and the star begins He burning at the RGB tip.

Low-mass stars of $\lesssim 0.5\ M_{\odot}$ do not contract enough to be able to burn helium. This is only important for time-scales greater than approximately 14 billion years (Hubble timescale) due to the slower burning rate in lower-mass stars.

There is some minor mass loss $\lesssim 0.2\ M_{\odot}$ on the RGB (McDonald & Zijlstra 2015). The mass loss is greater for lower-mass stars, i.e., the lower the MS mass, the more mass will be lost by the time it reaches the end of the RGB. This is primarily due to the fact that higher mass stars undergo a much faster stellar evolution, therefore will spend much less time on the RGB compared to low-mass stars. However, mass loss will also be greater in low-mass stars due to their lower surface gravity when compared to high-mass stars.

1.2.4 Horizontal Branch

At the start of CNO burning a star will move rapidly off the RGB and onto the Horizontal Branch (HB) in $\sim 1\ Myr$ (Kippenhahn, Weigert & Weiss 2012). At this point the core is burning He to CNO and outside the core conditions are still favourable for H-burning. The convective envelope is still present in cool HB stars but begins further out than in the RGB. It is mostly older stars that will make it onto the ZAHB. Intermediate-age stellar populations will remain around the red clump i.e., the area of the HB that is often observationally indistinguishable from

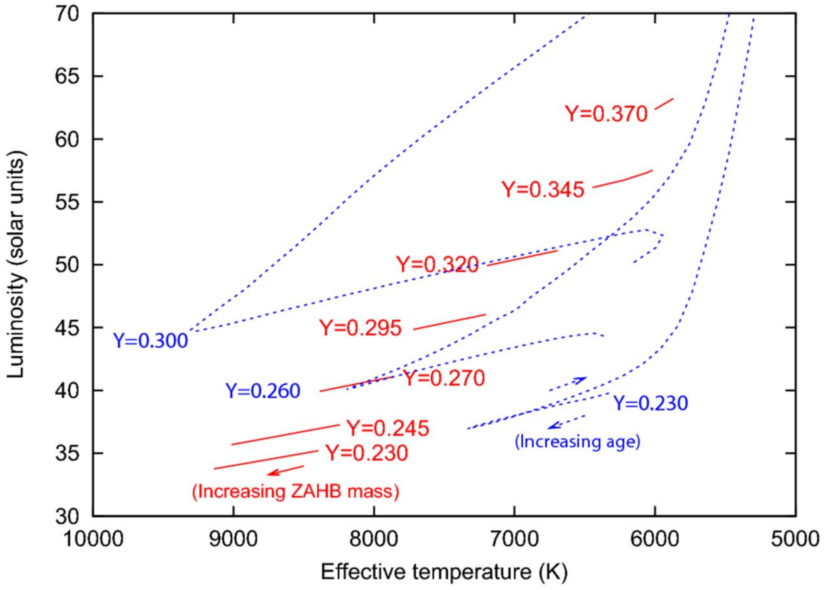

Figure 1.8: The position of the HB is dependent on Helium fraction, Y, with various positions shown on this diagram. Reproduced from McDonald & Zijlstra (2015).

the RGB bump. More massive populations above $\sim 2\ M_{\odot}$ cross the Hertzsprung gap above the RGB tip which avoids the HB completely.

The position on the HB is mostly dependent on the mass of the stellar envelope (Karttunen 2007) which is why the majority of stars end up in the red clump. Position dependence due to helium fraction is shown in Figure 1.8. The bluer and redder parts of the HB are separated by the instability strip (detailed in Section 1.2.4.1). This is where the RR-Lyrae variables sit on the diagram.

Metallicity has a secondary effect that dictates where a stellar population will sit on the diagram. For example, in a globular cluster with a metal-poor population, the horizontal branch will be predominantly blue (Karttunen 2007).

Stars will spend approximately 100 Myr on the HB. Once the He core is depleted the star will enter the AGB where He-shell burning begins.

1.2.4.1 Instability Strip

During the HB it is possible a star will cross the instability strip (Kippenhahn, Weigert & Weiss 2012). This strip crosses vertically on the HR diagram. Different

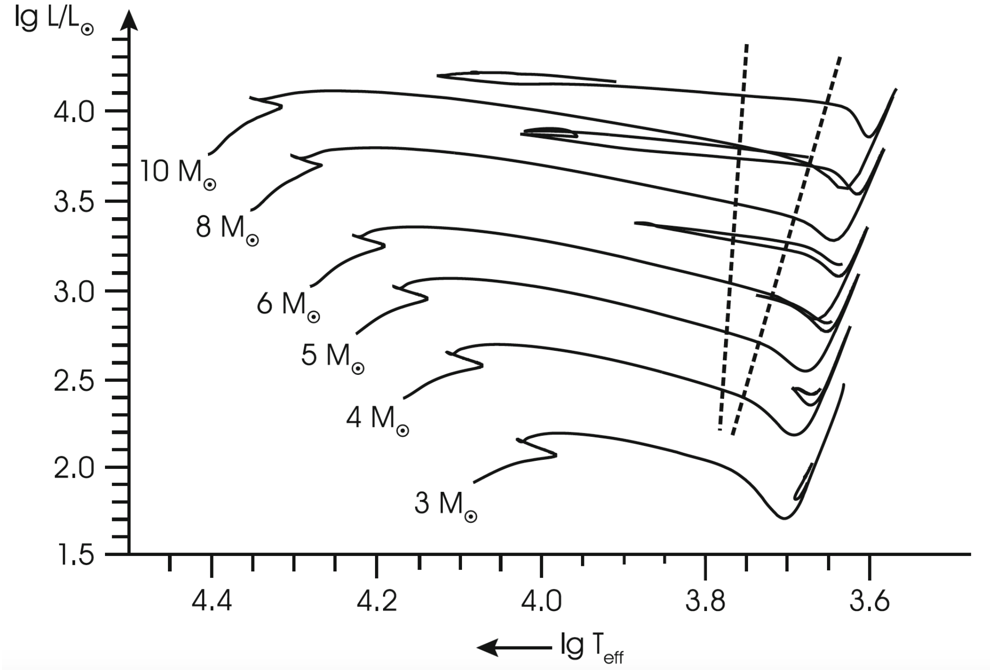

Figure 1.9: Evolutionary tracks for different solar masses from the MS turn-off. The instability strip is shown by the dashed lines. Reproduced from Kippenhahn, Weigert & Weiss (2012).

solar mass evolutionary tracks can be seen in Figure 1.2.4.1 with the instability strip illustrated. If the evolutionary track of a star crosses this strip during the HB it will become a variable star such as Cepheid or RR Lyrae. These pulsational instabilities are a result of how the outer stellar envelope reacts to purtubatoins and the resulting pulsations reaching observable amplitudes (Kippenhahn, Weigert & Weiss 2012).

1.2.5 The Asymptotic Giant Branch

The AGB is where most of the mass loss for low- and intermediate-mass ($\sim 1-10$ $M_{\odot}$) stars takes place. This is a relatively short phase of stellar evolution (2.5 $Myrs$ (Herwig 2005)) but is responsible for a large proportion of galactic luminosity due to the large increase in stellar luminosity during this phase (Karakas & Lattanzio 2014). It should be noted that the luminosity is determined by the core mass of the star in the AGB and not directly by the total stellar mass. The track taken by an AGB star can be seen in Figure 1.7.

The physical development of the star is similar as when it was on the RGB. This evolutionary stage contributes highly to chemical enrichment of the ISM (Karakas & Lattanzio 2014) due to dust and gas release via stellar mass loss. These elements include; C, N, F, Na, Ne, Mg. Other more massive elements are prduced in various supernovae (Karakas & Lattanzio 2014). The temperature of the AGB is dictated by the mixing processes occurring inside the star.

The beginning of this phase is marked by the helium-burning core running out of fuel, much like the hydrogen core at the beginning of the RGB phase. This again causes the core to contract and the formation of a helium-burning shell in between the contracting core and the hydrogen-burning shell. This double-mode nuclear burning becomes unstable and so leads to the generation of thermal pulses (Prialnik 2009; Karakas & Lattanzio 2014) which transitions the AGB to the thermally-pulsating AGB (TP-AGB).

Mass loss on the AGB is driven by the development of a strong stellar wind. This wind is created by a combination of pulsations and radiation pressure. The combined effect of the pulsations and pressure is great enough to overcome the gravitational attraction of the star and effectively blow mass from the star (Prialnik 2009). The gas from the stellar atmosphere is then released into the ISM (see Section 1.3.4).

1.2.6 Post AGB Evolution

After this highly active period of evolution, hydrogen and helium burning becomes unsustainable. For stars with an initial mass above $\sim 1\ M_\odot$ (Prialnik 2009), the stellar wind released during the AGB may be ionised by the contracting post-AGB star to form a planetary nebula. After the release of this stellar matter the temperatures required for nuclear burning cannot be sustained. All that remains

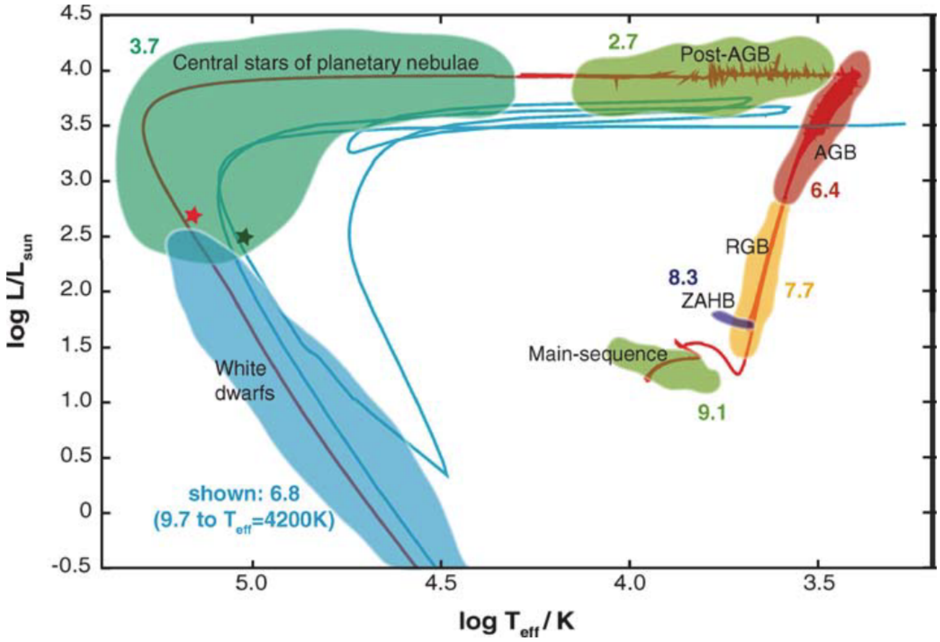

Figure 1.10: Stellar Evolution for a 2 $M_{\odot}$ from MS turnoff to the white dwarf cooling track. The numbers associated with each of the phases are the log of the approximate durations of the stages in years. Reproduced from Herwig (2005).

is the stellar core, which becomes a white dwarf and cools with the planetary nebula (Figure 1.10). The nebula expands and dissipates at a rate of $\sim$ a few 10 $km\ s^{-1}$ for the slow wind (Prialnik 2009), or up to $\sim$ 1000 $km\ s^{-1}$ (Kahn 1983).

1.2.7 Stellar Death

The stellar core that remains after post-AGB evolution is known as a white dwarf (WD). It will develop a degenerate carbon-oxygen core. This is generally the fate of low to intermediate-mass stars. The cooling track for a 2 $M_{\odot}$ ZAMS star are shown to the left of Figure 1.10.

The surface temperature and radius of the WD will be dependent on the initial stellar mass. However, the larger the initial mass of the star the smaller and denser the WD. The evolution of low-mass star is summarised in Figures 1.11 and 1.12.

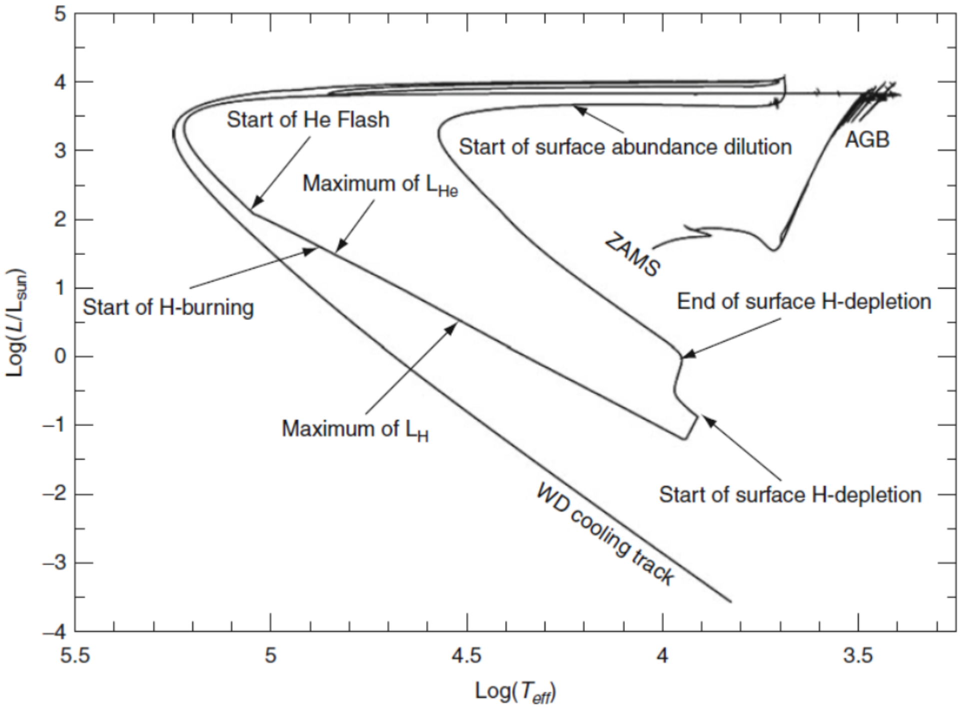

Figure 1.11: The track for a star of $\sim$ few $M_\odot$ and $T_{eff} \sim 10000$ K from the ZAMS to stellar death with important milestones indicated for each stage. The star here undergoes a late thermal pulse on the post-AGB track. Reproduced from Graham (2013).

1.3 Importance of Metallicity

The importance of metallicity (and in particular dust presence) during stellar formation has been known for many years. Metal content impacts the stages of chemical evolution within stars and the eventual enrichment of the surrounding galactic environment (Ryan, Norris & Beers 1996). The more metal-poor a star, the lower the mean atomic mass should be. The reduced metal content of the star will cause a decrease in radiation pressure as it can escape more easily. This causes stars to have smaller radii for a given mass which causes them to have a greater temperature for a given luminosity. This increased density also causes faster stellar evolution in metal-poor stars.

The mixing and metal processing pathways will be outlined here specifically for giant branch stars.

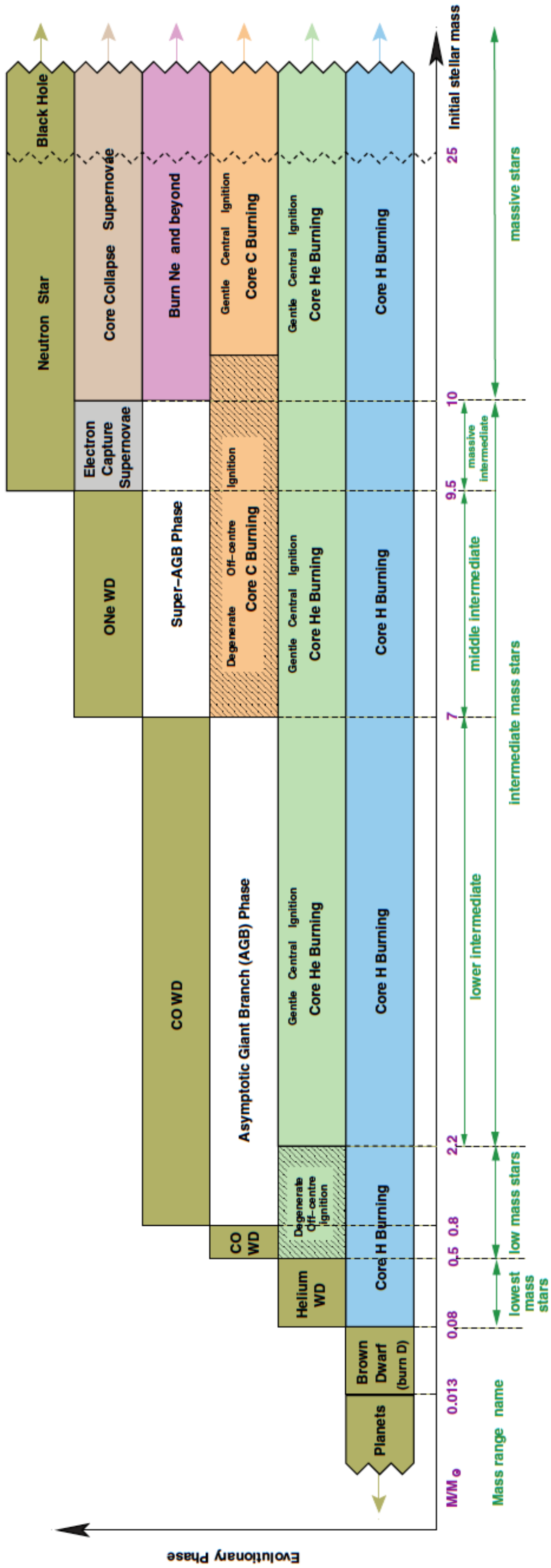

Figure 1.12: Burning stages for each evolutionary stage with mass estimates for each situation. Reproduced from Karakas & Lattanzio (2014).

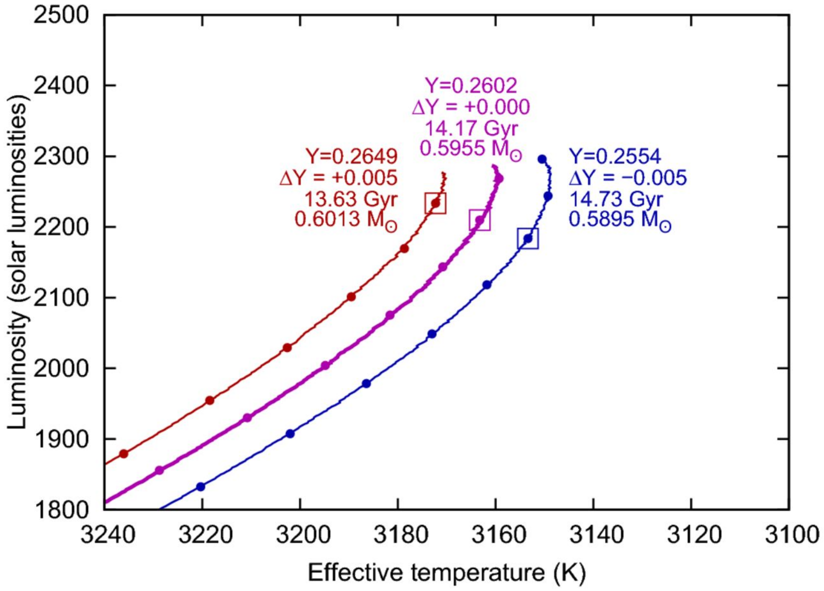

Figure 1.13: The three lines shown here indicate the position of the RGB tip for different helium fractions. For greater helium fraction the RGB tip moves to hotter temperatures. The increase in He fraction also causes an increase in density due to the greater molecular weight which in turn causes an increase in central pressure. The increase in temperature and pressure causes an increased burning rate compared to lower He fractions. Reproduced from McDonald & Zijlstra (2015).

1.3.1 Surface Metal Abundances

Many processes can impact the metal abundances at the surface and how metals are mixed throughout the star. The following processes do not directly contribute to metal production within the star but rather redistribute the existing metal content.

Dredge-up can occur in the RGB and AGB stages (detailed in sections 1.3.1.2 to 1.3.1.4). A star can undergo several of these processes during its lifetime. Dredge-up can change the chemical abundances in the stellar envelope by mixing material from the stellar core.

1.3.1.1 RGB Position

The position of the RGB on a Hertzprung–Russell diagram is dictated by several processes. For example, stellar populations that are more metal-rich will see the

RGB shifted to lower effective temperature (or redder colour). This is due to a greater opacity caused by the higher metal content. The star is able to retain a higher internal temperature which in turn causes it to expand and display a smaller surface temperature. There is usually a more minor shift depending on He fraction, detailed elemental composition and mixing processes. In particular, higher helium content increases mean atomic weight but provides little extra opacity, so causes higher densities and temperatures, increasing burning rates and speeding up evolution (Figure 1.13).

For higher-mass stars the MS turn-off is at a much higher luminosity. The star will cross the Hertzsprung gap much quicker than lower-mass stars. These higher-mass stars will also have a much lower RGB tip luminosity and in some cases they almost skip the entire RGB stage, as they cross the gap with luminosities higher than that of the RGB tip. This leads to a much more gradual beginning to He burning and as such will not undergo a He flash.

1.3.1.2 First Dredge-up (1DU)

1DU occurs during the RGB stage and is largely triggered by deeper convection occuring during the stars H-shell burning. Nuclear processed material is moved into the convective zone of the star. It is still hydrogen-rich, but also contains some of the products of many CNO cycle processes. 1DU occurs prior to any He burning in the star and so the impact on metallicity is minimal.

1.3.1.3 Second Dredge-up (2DU)

This dredge-up process occurs at the end of He-core burning in stars more massive than 4 $M_\odot$ or, more specifically, a star with a H-exhausted core of mass $\gtrsim 0.8$ $M_\odot$ (Karakas & Lattanzio 2014). This is because the convective envelope extends much deeper into the exhausted hydrogen-burning region. This is largely similar to the 1DU but in this case the deeper convective envelope causes mixing with complete H-burning products. This causes an increase in He content and ^{23}Na abundance (Karakas & Lattanzio 2014).

1.3.1.4 Third Dredge-up (3DU)

The 3DU only occurs in thermally pulsating AGB (TP-AGB) stars. A TP-AGB star is much like an early-AGB star in that it has long periods of H-shell burning. However, at some point during this shell burning, the pressure and temperature conditions become conducive to helium burning. This is much faster than hydrogen burning and quickly reaches the H-burning shell and ceases. This occurs in a shell just outside the degenerate core of the star, and causes a large expansion and increase in luminosity during the burning known as the Thermal Pulse. This has the secondary effect of reducing the pressures and temperatures in the star to below what is necessary for H-shell burning and so this ceases during the pulse. Once this explosive He-shell burning has ended the star contracts to conditions that are once again favourable to quiescient H-shell burning, so this resumes (Prialnik 2009).

The pulses last $\sim$ centuries (Karakas & Lattanzio 2014) with a long interpulse phase lasting approximately $\sim 10^4$ to 10^5 years (Graham 2013; Karakas & Lattanzio 2014). It is during the pulses that the convective envelope dredges material from the core. The core comprises of degenerate carbon and oxygen, however, 3DU mix material from the stellar core into the envelope which in turn can increase carbon abundance in the stellar envelope.

1.3.1.5 Carbon Star Formation

A carbon star (C-star) is simply one which has a carbon-to-oxygen ratio greater than unity. There are many processes that occur in a star that may favour, such as 3DU, or hinder the formation of these stars which will be conducive to carbon star formation.

In general, for conditions to be favourable for C-star formation, metallicity should be low. Therefore a lower oxygen abundance would be required. This could be achieved by a greater number of 3DU events or more efficient 3DU events. There are several mixing processes that will impact C-star formation, many of which are outlined in later sections.

1.3.2 Extra Mixing Processes

It is largely unclear how efficient the following mixing processes are. Without quantifying these efficiencies it is unclear how much of an impact each process has on the evolution of a star.

1.3.2.1 Convective Overshoot

Convection is the most effective mixing process. The convective overshoot process was conceived as a theoretical parametisation that extends the convective envelope deeper into the star. This process is used in various theoretical stellar evolution models to allow these models to match observations (Herwig 2000). This process sees the mixing of the material in the convective zone close to the boundary to the nuclear-burning shell over the boundary (Herwig 2000).

1.3.2.2 Thermohaline Mixing

This process occurs when high-density material sits on top of lower-density material. The higher-density material sinks across the boundary in discrete lines perpendicular to the boundary. These lines then proceed to mix with the surrounding material (Karakas & Lattanzio 2014). This process is analogous to the mixing that occurs when salt water meets fresh water and represents any interaction between two fluids with different specific densities. In terms of a stellar mixing process, thermohaline mixing is one possible explanation for changes in surface abundances for Li, ^{12}C, ^{13}C, and ^{14}N (Szigeti et al. 2018). During the RGB stage, the ^{3}He(^{3}He,2p)^{4}He reduces the mean molecular weight just above the hydrogen burning shell. This will cause denser material from the core to mix across to just above the H-burning shell (Matrozis & Stancliffe 2017).

1.3.2.3 Rotational Mixing

Internal rotation of a star may cause what is known as *meridional* mixing (Sweigart & Mengel 1979). This mixing is primarily caused by the deviation of a rotating star from spherical symmetery. The deviation from spherical causes difficulty in fulfilling the conditions of hydrostatic and thermal equilibrium. This causes the star to set up circilation currents that compensate for this at each point on the surface (Sweigart & Mengel 1979). This usually occurs during the start or just before the RGB.

This extra internal circulation may cause the mixing of CNO material close to the H-shell into the convective envelope of an RGB star (Sweigart & Mengel 1979). This has also seen to be largely observationally consistent with stars that have low C^{12}/C^{13} ratios (Sweigart & Mengel 1979).

Meridional mixing also has an impact on the internal distribution of metals in a star. Significantly, it could lead to a reduction in C^{12}/C^{13} ratio and could have a significant impact on CNO processing in the convective envelope if the MS angular velocity is large enough (Sweigart & Mengel 1979).

As a point of comparison, Figure 1.15 represents the evolutionary tracks for very low metallicity stars of various solar masses for both rotating and non-rotating stars.

1.3.2.4 Magnetically-Driven Mixing

In order to move nuclear material from the H-burning region to the convective envelope, Busso et al. (2007) and others have suggested that some magnetically driven mixing, namely a so-called stellar dynamo, may be a contributor.

A stellar dynamo forms from the differential rotation below the convective envelope. This is turn drives toroidal magentic fields near the H-burning shell. This is a possible mechanism for the extra mixing within both RGB and AGB

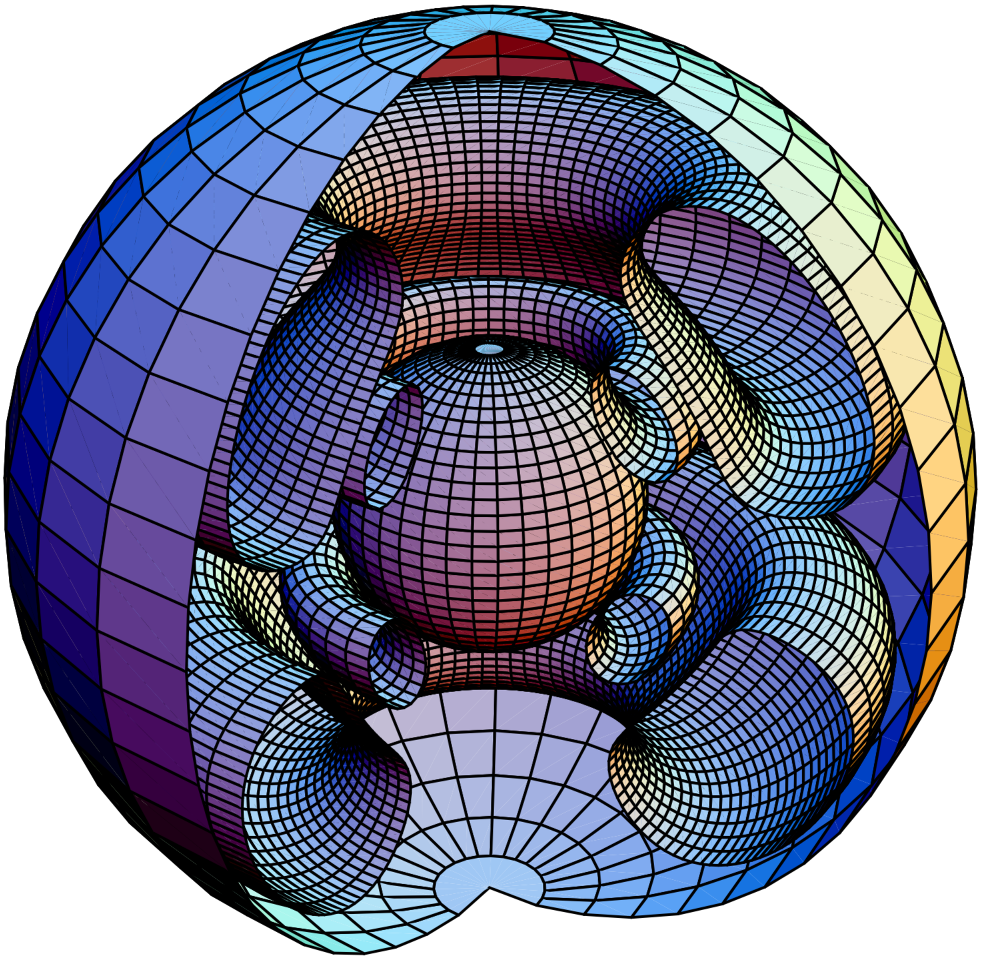

Figure 1.14: This Figure demostrates the process of meridional mixing that would occur in stellar convective layers. Specifically it shows the stream lines for a 20 $M_{\odot}$ star with solar metallicity at the beginning of the H-burning phase. The inner sphere represents the boundary to the inner convective core in this ZAMS star. Reproduced from Meynet & Maeder (2002).

stars. Busso et al. (2007) placed estimates of $B_0 \sim 5 \times 10^4 - 4 \times 10^5$ G for RGB stars and $B_0 \sim 5 \times 10^6$ G for AGB stars.

1.3.3 Metal Production

The processes considered in the previous section were concerned largely with the redistribution of the metal content and with little impact on total metal abundance. This section will discuss processes that have a direct impact on the

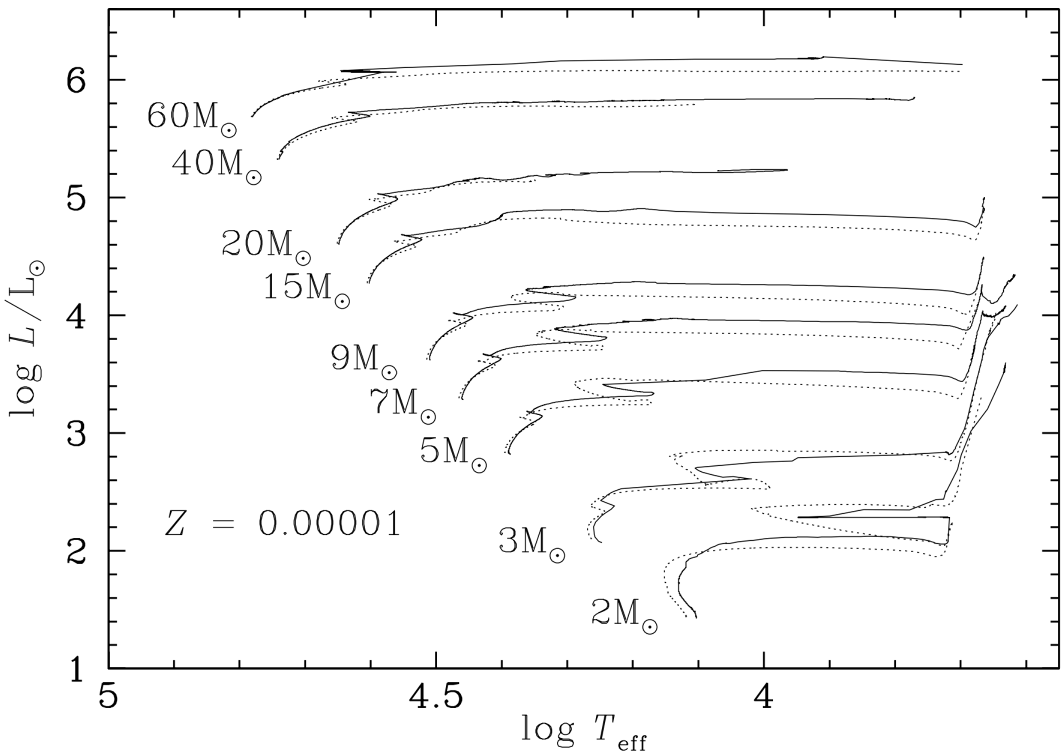

Figure 1.15: Various stellar masses are represented in these evolutionary tracks for metal-poor stars. The solid lines represent non-rotating stars and the dotted lines represent rotating stars with an initial rotation velocity of 300 $km\ s^{-1}$. These tracks were computed using stellar models. Reproduced from Meynet & Maeder (2002).

elemental abundance ratios of the star.

1.3.3.1 The *s*-process

In order to obtain heavy metals in a star, neutrons must be added to the nucleus. This can occur via two processes: the *s*-process, or slow neutron-capture process, and the *r*-process, or rapid neutron-capture process. However, it is largely considered that the extreme conditions required for the *r*-process to proceed may only be found within supernovae therefore we will only consider the *s*-process as being important in stellar evolution during the AGB phase (Karakas & Lattanzio 2014).

For the *s*-process, neutron densities of $N_n \gtrsim 10^8$ $neutrons\, cm^{-1}$ would be required. For AGB stars the source of these neutrons can be seen in two important processes:

1. ^{14}N$(\alpha,\gamma)^{18}$F$(\beta^{+}\nu)$ ^{18}O$(\alpha,\gamma)^{22}$Ne$(\alpha,n)^{25}$Mg.
2. ^{12}C$(p,\gamma)^{13}$N$(\beta^{+}\nu)^{13}$C$(\alpha,n)^{16}$O.

Due to the temperatures required for the ^{22}Ne$(\alpha,n)^{25}$Mg reaction to occur, process (1) is more effective in AGB stars that have initial masses in excess of $\sim 4\ M_{\odot}$. In stars of $\lesssim 4\ M_{\odot}$ the ^{13}C$(\alpha,n)^{16}$O mechanism is most important. This, therefore, requires ^{13}C to be present in between the He-shell and H-shell. Some of this can be mixed in from the CNO cycle but not enough for this process to proceed in any appreciable quantity. Pockets of ^{13}C can be formed through the CN cycle with the abundant ^{12}C present (Karakas & Lattanzio 2014). The *s*-process takes place in between thermal pulses and as such its products can be mixed into the outer layers via 3DU.

1.3.3.2 The *i*-process

Following on from the *s*-process we should also consider various *intermediate* neutron capture processes or *i*-processes. These processes are triggered by the rapid transfer of H in the He-burning regions (Roederer et al. 2016). ^{12}C captures the H that is ingested and produces ^{13}N, this in turn decays to ^{13}C and the ^{13}C$(\alpha,n)^{16}$O reaction activates. This process can be found in numerous environments including; post-AGB stars and, importantly for this work, in low-mass/metal-poor stars in the He-core and He-shell flashes (Roederer et al. 2016).

These processes generally proceed with neutron densities of $\sim 10^{15} cm^{-3}$. This is due to the processes being largely dependent on the timescales of two processes: convective turnover at approximately 10-20 minutes, and the β^{+} decay timescale of ^{13}N at approximately 9.6 minutes (Roederer et al. 2016).

1.3.3.3 The α-process

This process adds a helium nucleus to more massive nuclei and occurs after the exhaustion of He burning and does not produce heavy metals. The nuclei produced are shown as a logarithmic ratio of a star's iron abundance as [α/Fe]. The nuclei produced include: ^{28}Si, ^{24}Mg, ^{32}S, ^{36}Ar, ^{40}Ca, ^{48}Ti and ^{44}Ca, in order of decreasing relative abundance (Burbidge et al. 1957). This process also does not contribute large amounts to the star's luminosity in isolation. This series of nuclear reactions requires high tempertatures mainly found in high mass stars and supernovae.

1.3.3.4 Proton Ingestion Episodes (PIEs)

PIEs are caused in stars more massive than 1 $M_{\odot}$ (Karakas & Lattanzio 2014) by the He-rich convective zone coming into contact with the H-rich envelope during the core flash (Karakas & Lattanzio 2014). This is more prevalent in metal-poor stars for two reasons. The first is that, in these metal-poor stars, the core flash is offset from the stellar centre, and is closer to the H-rich envelope. Secondly, the entropy gradient that normally helps to keep the two regions separate is much reduced in metal-poor stars.

1.3.3.5 Hot Bottom Burning (HBB)

This process takes place during the inter-pulse phase in TP-AGB stars. During HBB, the base of the outer convective envelope enters the H-burning shell and gets hot enough to cause proton-capture. This causes ^{12}C and ^{16}O to transmute primarily into ^{14}N, which effectively decreases the ^{12}C abundance in the envelope, in turn preventing carbon-star formation (Fishlock, Karakas & Stancliffe 2014; Busso, Gallino & Wasserburg 1999), provided that 3DU does not continue after the end of HBB (Busso, Gallino & Wasserburg 1999). At the very least the onset of HBB will delay carbon star formation and may cause lower ^{12}C/^{13}C ratios than seen in normal C-stars (Busso, Gallino & Wasserburg 1999). HBB ends due to a reduction in envelope mass, therefore lowering temperature and pressure in the nuclear burning zones. HBB occurs in stars of mass $\gtrsim 4\ M_{\odot}$, however, it is known to be metallicity dependent (Lattanzio & Wood 2004).

1.3.4 Mass Loss

Mass loss is important when considering the enrichment of the surrounding. Enrichment occurs by transportation of synthesised elements from the core into the stellar atmosphere via various mixing processes. These elements are then driven out of the atmosphere through the stellar wind. Mass loss primarily occurs during the RGB and AGB phases of evolution (McDonald & Zijlstra 2016) and is dependent on the initial mass of the star.

1.3.4.1 Mass Loss on AGB

During the TP-AGB, mass loss becomes very intensive. Thermal pulses are expected to increase the mass loss rate by causing significant changes in luminosity and stellar radius. However, as the thermal pulses are very short the impact of these on mass loss are reduced. Work performed by Maercker et al. (2012) suggests that the thermal pulses enhance mass loss rate significantly. There are more gradual increases in mass loss rate through slow increase of these parameters as the star progresses along the AGB.

The mass lost during this phase is primarily pushed into a circumstellar envelope by the surface pulsations (Bladh et al. 2013). As convection occurs on specific timescales it is possible for the period of the convective envelope to become synchronised with the fundamental period of the star's pulsations which causes an amplification of this process. This material is now located at temperatures where it can cool, heavier elements can condense out as dust, and be released into the surrounding medium.

As CO has the highest binding energy of these molecules it is the first to form out followed by molecules such as TiO, SiO, H_2O, CO_2, VO, ZrO and Al_2O_3 for oxygen-rich stars, and CN, C_2, SiC and HCN for carbon stars. This increase in molecular opacity causes a blanket-like effect as it shrouds the star which will impact any observations of the star. This insulates the star and reduces heat loss. Indeed, the spectroscopic signature of cool CO in the stellar envelope of a star is used as a tracer for mass loss at this stage (McDonald & Zijlstra 2015). Around this stage it becomes difficult to define a physical surface for the star and they become more difficult to observe in the optical due to this increase in opacity.

The dust grains that begin to form are slowly pushed away from the star due to the absorption and scattering of radiation by the dust from the star (Bladh et al. 2013; Norris et al. 2012). This radiation driven wind expands at a relatively slow velocity of the order of $\sim$ few kms^{-1} (Willson 2000; Danilovich et al. 2015). The pulsation of the AGB star not only initiates mass loss wind but can also enhance this radiation-driven wind and increase the outflow velocity (Willson 2000). This enhancement is achieved by providing a source of mechanical energy while also levitating the atmosphere so it partially overcomes the gravitational potential of the star (Willson 2000). When considering a metal-poor star it is important to understand how this process impacts the enrichment of the surrounding ISM. This is because material must be levitated further from a metal-poor star before it can condense into dust, due to the higher tempertures at a given luminosity. This, coupled with the fact there is less dust per unit gas, means it is harder for radiation pressure to drive the wind into the surrounding ISM.

1.3.4.2 Observational Impact of Circumstellar Dust

Circumstellar dust is found around most giant branch stars and is a side effect of material released from the star to altitudes where it is able to condense. The observatinal impact of this dust has been studied for many years as it impacts any study of these stars that is undertaken.

The main observational impacts of circumstellar dust occur when observing AGB stars. This impact is in the form of obscuring the star behind the dust in optical wavelengths and re-emitting the absorbed photons at mid- and far-infrared (Marigo et al. 2008). The main impact on this data is a reddening of the observed stars. The amount of observed reddening is improtant to quantify as it is mainly controlled by mass-loss rate and dust opacity. Specifically, the luminosity at which the reddening begins is of interest as this is the point where the conditions are favourable for dust production. An undesirable side effect of this observational reddening is that the source will become dimmed in the optical due to the reprocessing of this light. This could move stars to below the sensitivity limit for the observations.

The amount of observed reddening is important in various ways. Dust is made up of different molecules and is dependent on the chemistry of the star that produced it. These different dust types will process radiation differently and have different reddening laws. If we assume that mass-loss is as efficient as at solar metallicity, then reddening caused by circumstellar dust should start at similar evolutionary stages. Work carried out by McDonald et al. (2011) with globular cluster stars indicates that this is indeed likely the case, at least for low-mass stars.

1.4 Project Aims

In order to generate a catalogue of point-sources for the dIrr galaxies, observations of these galaxies made in 2016 were reduced into a useful dataset. This data was primarily taken with the Visible MultiObject Spectrograph (VIMOS) instrument on the Very Large Telescope (VLT). Further data has been gathered from work that is published taken by the *Spitzer Space Telescope* and will be used as a comparison to the VLT data obtained.

Chapter 2 of this work will concentrate primarily on the raw observations and prelimernary data reduction and calibration steps. Chapter 3 will focus on the reduced data and produce CMDs to define observed stellar populations. Chapter 4 will attempt to bring these previous chapters together and bring together contemporanious work in order to place these observations into the proper context.

Chapter 2

Observations and Data Reduction

The primary data used in this survey was obtained by the VLT using the VIMOS instrument in imaging mode. This instrument has an angular resolution of $0.205''$ per pixel in imaging mode (ESO 2015). The data was taken in 2016 and consists of V and I-band images of the eight dIrrs previously outlined in Chapter 1. Also contained within the data set are the bias and sky flat frames required for calibration purposes. The science frames consist of 198 V-band and 192 I-band images. The reduction and processing of this large set of images occupied the bulk of the time available for this project and presented its own challenges that would ordinarily not be an issue for smaller sets of data. In particular, efficient programs were needed to reduce the data sets in a reasonable timescale.

2.1 Data Pipeline

In order to use the data for meaningful analysis, it must first be calibrated. To that end, the European Southern Observatory (ESO) data reduction pipelines were used. Specifically, the ESOREX program was used to apply specific reduction recipes to the data and a PYTHON program was written in order to perform each stage of the calibration. The dataset contains images taken in four CCD quadrants so each stage of the calibration was carried out separately for each quadrant.

All of the image calibration techniques are described in detail within the VIMOS pipeline manual (ESO 2016)[1].

2.1.1 Bias

The first step of the calibration is to generate a master bias frame to subtract from the science images. The bias frames were added to a set-of-frames (SOF) file to be passed to the ESOREX recipe *vmbias*. This recipe generates the master bias image to be used in further recipes and the final calibration. At this stage the *vmbias* recipe was also instructed to search and clean cosmic rays and to use the "Average" method to stack the frames. By using the average method, each combined frame pixel is the average of all the corresponding pixel values from the input frames (ESO 2016).

2.1.2 Sky Flat

In order to generate a master sky flat, the sky flat frames in this dataset were isolated and listed in a SOF file. Additionally, a bias calibration must also be performed on the master flat so this file was also included in the SOF file. Finally, as there are bad pixels present in the images it was necessary to attempt cleaning of these: bad pixel tables for each CCD were included. Therefore, the final parameters given to the ESOREX recipe *vmimflatsky* were: the SOF file containing all of the relevant sky flats, a request for bad pixel cleaning, a request for cosmic ray cleaning and the instruction to stack the images using the "Median" method. By using the median of frames each combined frame pixel is the median of all the corresponding pixel values from the input frames.

The order in which this process occurs for the calibration of this data is as follows;

[1]VIMOS pipeline user manual: `http://www.eso.org/sci/facilities/paranal/instruments/vimos/doc/VLT-MAN-ESO-14610-3509_v98.pdf`

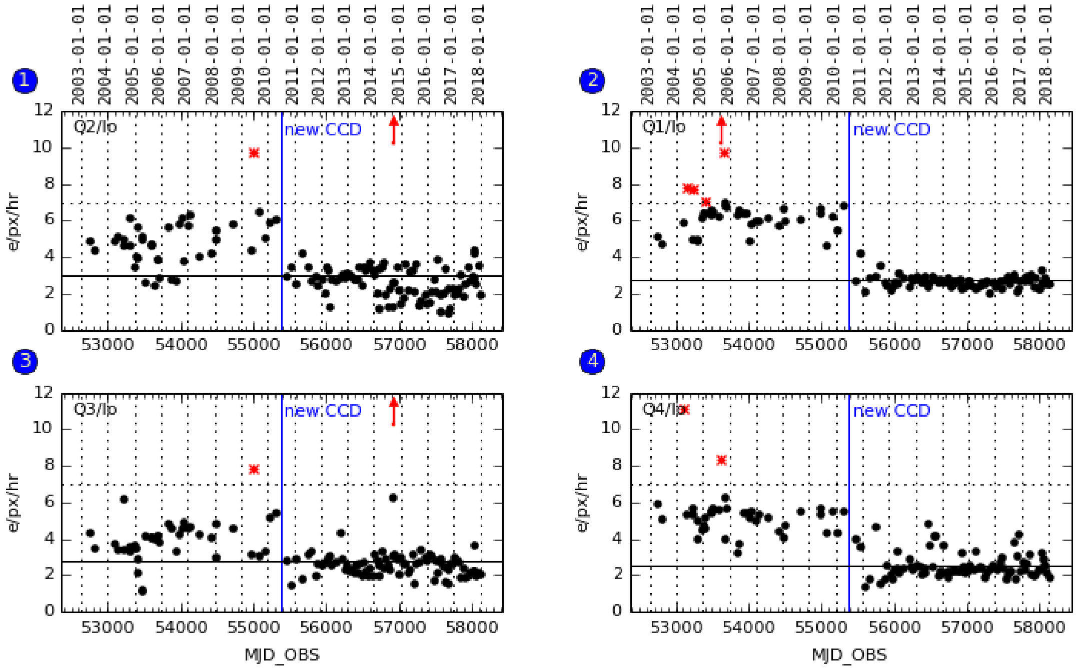

Figure 2.1: This data shows the level of the dark current for the 4 VIMOS detectors both before and after the CCD upgrade in 2010. The solid black line indicated the median level of the dark current. Reproduced from ESO (2018).

1. Bias subtraction.
2. Cosmic ray removal.
3. Combination of input sky flat frames.
4. Creation of master sky flat.
5. Bad pixel cleaning of master sky flat.

2.1.3 Dark Current

For the purposes of this data reduction and calibration the dark current for VIMOS will be ignored as it is stable over periods of several months and has a negligible impact on the data. As this data was gathered in imaging mode, only the low gain dark current is relevant (ESO 2018). Figure 2.1 shows the stability of the dark current over long periods, from before and after the CCD upgrade in 2010. As this data was taken in 2016 only the upgraded CCD data is relevant. The trends for each detector show the low values median values of the dark current over long periods and the values quoted in the VIMOS user manual ESO (2016) show that the dark current can be considered as $\lesssim 7e^{-}/px/hr$ (ESO 2016).

2.1.4 Science Calibration

Once these master calibration frames were generated, they must be applied to each science image for each corresponding quadrant. In order to achieve this the ESOREX recipe *vmimobsstare* was used. Each science image must be calibrated separately. In order to obtain a table of detected objects, the recipe was also given the relevant standard photometric table provided for the correct CCD quadrant and observing band. Therefore, the recipe was instructed to perform bias correction, sky flat correction, clean bad pixels, clean cosmic rays and to produce a table of detected objects and their parameters. The two outputs of this recipe are the final reduced image and detected object table.

The order in which each stage of the final calibration occurs, along with the section that describes the process, is as follows;

1. Bias subtraction (2.1.4.1),
2. Flat field correction (2.1.4.2),
3. Bad pixel cleaning (2.1.4.3),
4. Cosmic ray removal (2.1.4.4),
5. Source detection (2.1.4.6).

In order to perform source detection the recipe uses SEXTRACTOR, the process of which is described in section 2.1.4.6.

2.1.4.1 Bias Subtraction

A CCD is made up of many individual pixels that take the overall image. These pixels do not have zero initial values; in order to prevent individual pixels from having a value below zero ADU a bias voltage is intentially inserted. However, the bias for individual pixels is relatively stable over long periods and so it can be easily removed.

This is accomplished by taking many zero-exposure frames with the shutter closed. This way only the bias in each pixel value is exposed. In the case of this calibration these individual bias frames are then averaged and stacked into a master bias frame. The master bias frame is then subtracted from every subsequent science image or calibration product, including the master flat field.

2.1.4.2 Flat Field Correction

Using flat fields corrects for the fact that not all CCD pixels have the exactly the same sensitivity. This may be due to vignetting, or the presence of dust in some part of the optics. In order to correct for this many sky flat frames were captured. This involved taking images of the twilight sky as this is a useful source of even illumination. Exposures are set to provide a significant signal level.

New flat fields were generated for the V and I-band filters used. Each flat field was corrected for bad pixels, cosmic rays and a bias subtraction was performed. Once these master sky flats were generated they were divided from the science images to correct for these deviations.

2.1.4.3 Cleaning Bad Pixels

During the calibration, bad pixel cleaning was requested in the ESOREX recipes *vmimflatsky* and *vmimobsstare*. A bad pixel table was included in the calibration recipes for VIMOS. It was not possible to produce a new bad pixel table based on the existing data due to a lack of required data. For details on the bad pixel cleaning algorithm see ESO (2016).

2.1.4.4 Cosmic Ray Cleaning

Once any cosmic rays have been identified they are cleaned by using the interpolation procedure described in section 2.1.4.3. It should be noted that the use of the combination of frames using the median method will also effectively remove most cosmic ray events. For details of the identification proceedure see ESO (2016).

2.1.4.5 Image Vignetting

Image vignetting is a problem in some of these images due to pixel saturation close to the border. This would ordinarily cause false detections in the saturated region. However, the impact of this effect is reduced because a reduced selection area is used during source detection. This box is selected excluding the outer edge of the image to reduce false positive detections where appropriate. This has the detrimental effect of excluding sources outside of the detection window.

2.1.4.6 Source Detection (SExtractor)

Source detection occurs during the ESOREX recipe *vimobstare*. In order to accomplish this the recipe uses SEXTRACTOR for a rapid source detection method. This source detection is requested during the final stage of image calibration during the calibration recipe *vmimobsstare* (ESO 2016). When requested this recipe was given the instruction to clean bad pixels, clean cosmic rays. A photometric table was also provided in order to transfer the relevant zero points into the resulting fits header. This process produces a table of the detected objects along with their respective instrumental magnitudes, both celestial and image coordinates, and their stellarity index. Where stellarity index is defined as 0 for a galaxy, 1 for a star, and non-integer values in-between these for ambiguous objects (Bertin & Arnouts 1996). Stellarity index can be considered as a measure of being "point-source-like" or "extended". The detected objects are written to a corresponding FITS table upon image reduction along with those parameters previously outlined.

One of the most useful additions to the SExtractor input is a “window” parameter which is not present in the normal use of SExtractor. This parameter defines a box in the image in which the detections occur. This helps to reduce false detections from vignetted regions, which was a problem in some of the images used. Typical seeing for these images ranged from $0.64''$ to $1.39''$ with a mean value of $0.92''$ and median of $0.91''$. Also important to consider is any deblending carried out by SExtractor. Blending occurs when two bright objects are so close to each other that they are not easily distinguishable. Deblending is done by taking a provided threshold and assessing which pixels, or parts of pixels, are part of which object detected. This is especially important when considering the crowded fields contained within this data. With the esorex implementation of SExtractor, this is taken from the relative background RMS for each image. Further to this SExtractor defines a fraction of thresholds in a tree-type manner in order to separate close objects within a contrast limit.

2.2 Photometric Offset

In order to calibrate the magnitudes provided by SExtractor, the data for each galaxy should be compared to an external dataset. The V and I-band magnitudes (Table 2.1) were simply subtracted from the crossmatched VLT data to provide an offset which was then plotted (Figures 2.2 to 2.9) to determine an approximate offset. This offset was calculated with crossmatched extenal datasets.

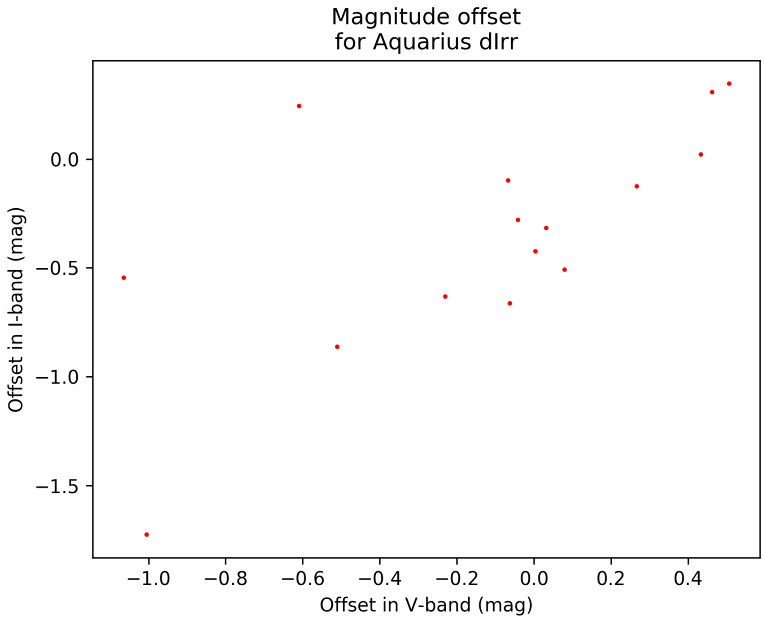

Figure 2.2: Photometric offset for Aquarius dIrr.

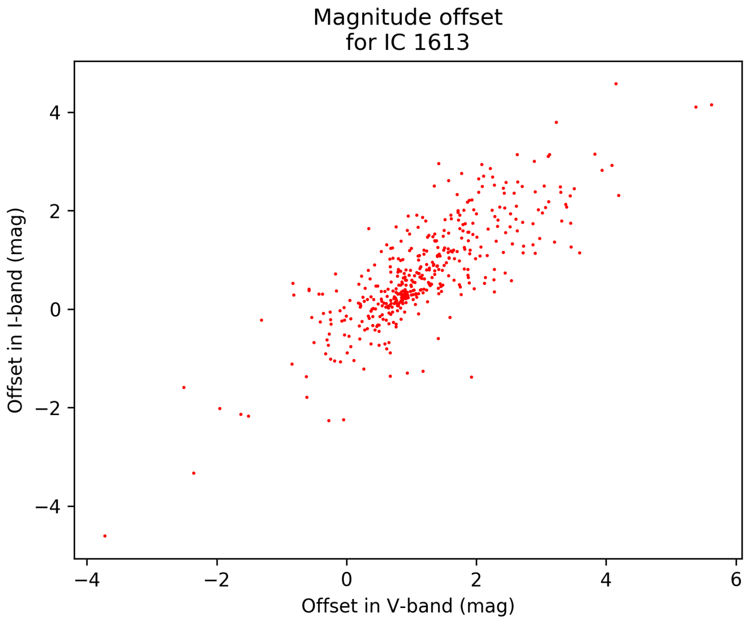

Figure 2.3: Photometric offset for IC 1613.

The small number of matched sources and scatter in the Aquarius dIrr galaxy made it difficult to find a magnitude offset however, there is good agreement on comparison to the offsets found for the remaining dataset.

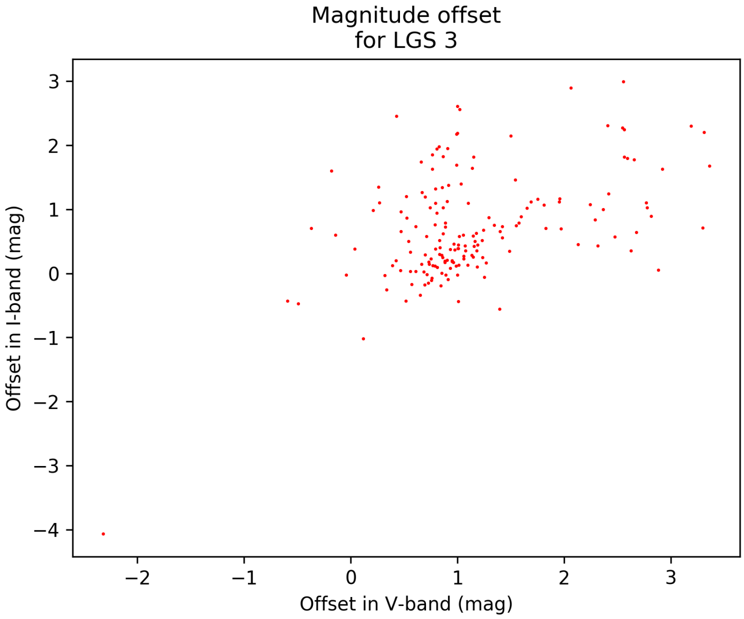

Figure 2.4: Photometric offset for LGS 3.

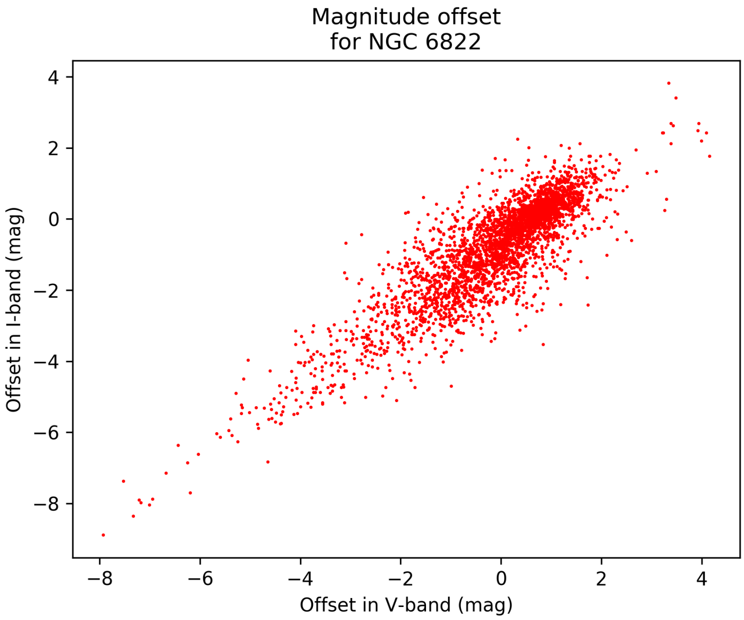

Figure 2.5: Photometric offset for NGC 6822.

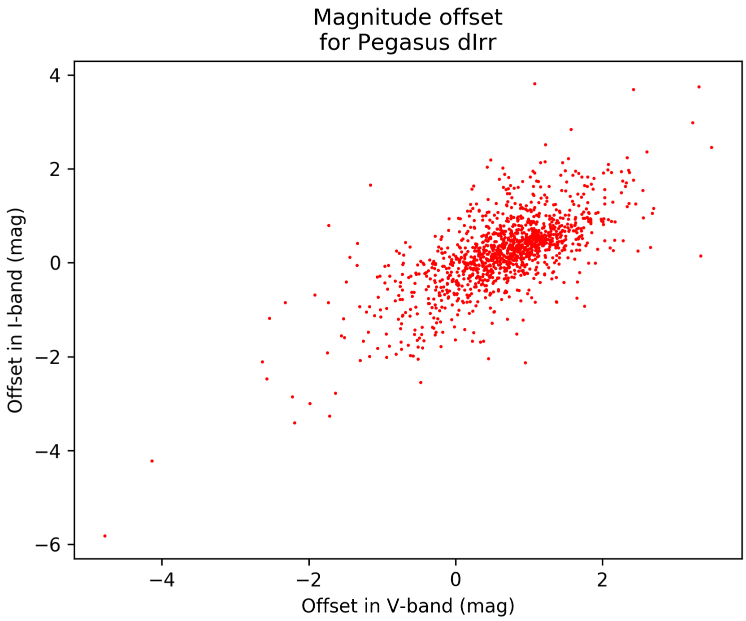

Figure 2.6: Photometric offset for Pegasus dIrr.

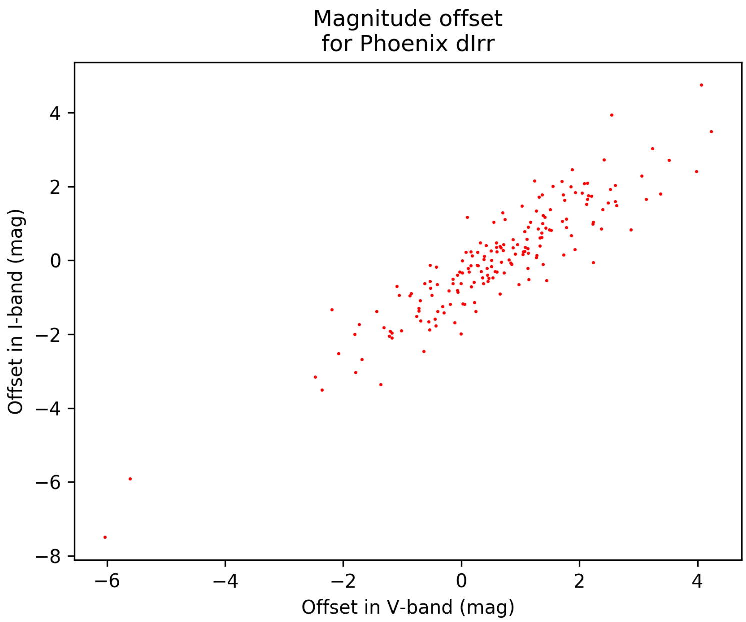

Figure 2.7: Photometric offset for Phoenix dIrr.

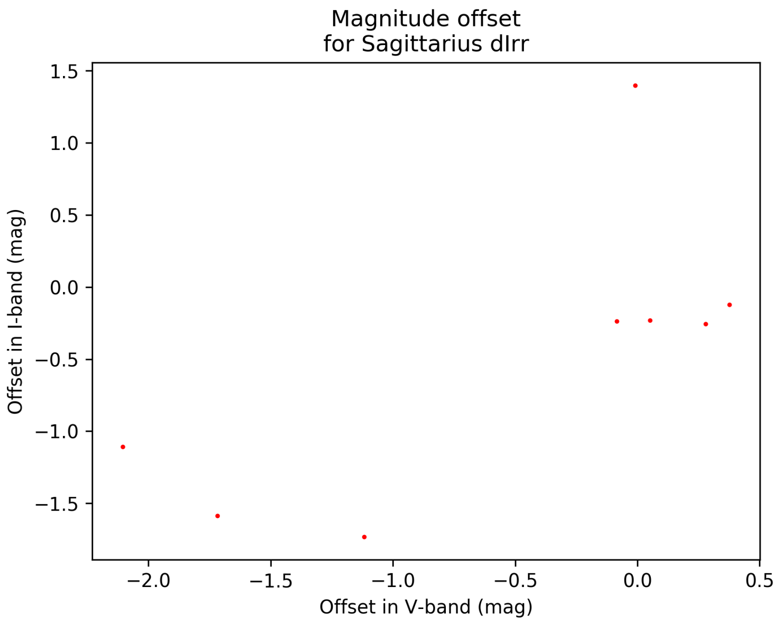

Figure 2.8: Photometric offset for Sagittarius dIrr.

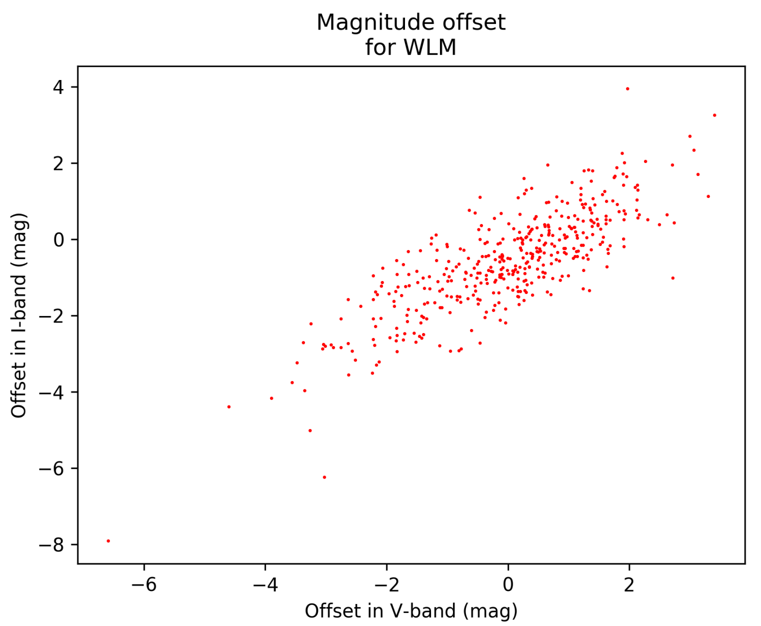

Figure 2.9: Photometric offset for WLM.

As with the Aquarius dIrr, the magnitude differences for Sagittarius dIrr show a large scatter (Figure 2.8) but it was still possible to produce a reasonable correction from the data.

The sources of these data and the offsets derived from them are shown in Table 2.1. The catalogue was then corrected by these offsets for the remainder of the analysis.

Table 2.1: Derived photometric corrections from crossmatched catalogues. The source for each dataset is quoted with its corresponding correction.

Galaxy	V-band correction (mag)	I-band correction (mag)	Average offset error ($''$)	Source of data
Aquarius dIrr	0.1	-0.5	0.503	Kirby et al. (2016)
IC 1613	1.0	0.2	0.462	Udalski et al. (2001)
LGS 3	1.0	0.2	0.503	Alam et al. (2015)[a]
NGC 6822	0.8	0.2	0.412	Bianchi et al. (2012)
Pegasus dIrr	0.8	0.25	0.395	Bianchi et al. (2012)
Phoenix dIrr	0.8	0.2	0.444	Bianchi et al. (2012)
Sagittarius dIrr	0.2	-0.2	0.514	Kirby et al. (2016)
WLM	-0.5	0.5	0.441	Bianchi et al. (2012)

[a] Data was first converted to V and I-bands using the method provided at the following source: http://www.sdss.org/dr13/algorithms/sdssUBVRITransform/#Lupton2005

Chapter 3

Colour-Magnitude Diagrams

In order to generate CMDs for these galaxies the V and I-band images must first be paired up in as many unique matches as possible. As there are more V-band images, it is not possible to generate unique matches with all of the images. However, using a simple PYTHON script it was possible to make 186 unique coordinatenpairings. These pairings encompass all of the galaxies previously mentioned and have no offset between them.

3.1 Astrometry

The coordinates provided by the SExtractor output are given using the world-coordinate-system (WCS). However, depending on exactly what assumptions are made during this part of the analysis will determine the accuracy of these provided coordinates. In order to establish the presence of any potential offset the RA and DEC were plotted against each other along with various datasets. An offset between the V and I-bands may also be expected which has been examined in Figures 3.1 and 3.2. The usefulness of Figure 3.2 is questionable but it is possible to see an estimated offset of approximately $0.2''$ from Figure 3.1.

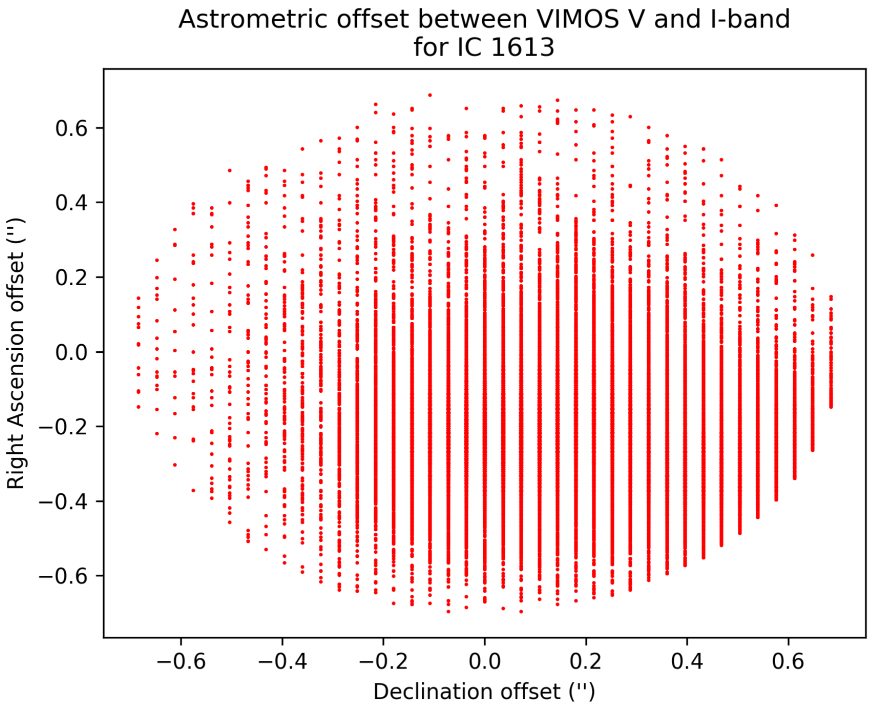

Figure 3.1: Astrometric offset comparison for VIMOS V and I-band source coordinates for IC 1613. Both axes are represented in arcseconds.

3.2 Ideal Image Matches

During this stage of the data reduction, only images that were found to be an exact match with coordinates were used. Note that WLM consists of two separate pointings and for the purposes of this analysis they will be combined into one dataset.

3.3 Observing band Crossmatching Radii

In order to perform a cross-correlation between the V and I-band detected sources STILTS was used (Taylor 2006). STILTS obtains the RA and DEC of each input table and performs a comparison between them. Using the input search radius, STILTS minimises the separation between each potential match and rejects those outside of the required radius.

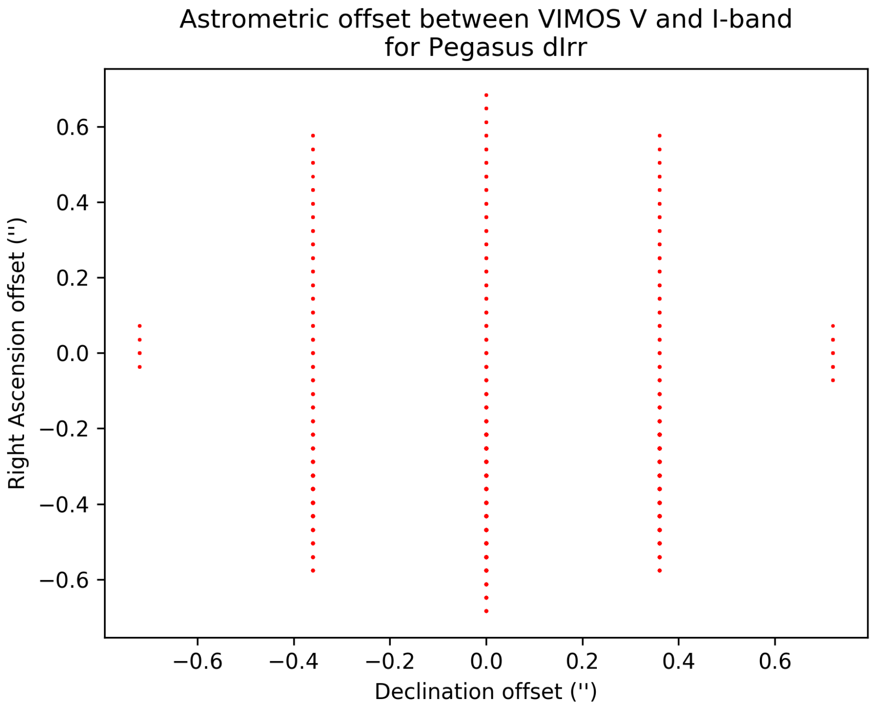

Figure 3.2: Astrometric offset comparison for VIMOS V and I-band source coordinates Pegasus dIrr. Both axes are represented in arcseconds.

A small PYTHON script was written to take the 186 ideal image matches, call STILTS, and request a cross-correlation of these image pairs. The matching radius was specified as $0.7''$ as this was deemed restrictive enough not to cause an unreasonable amount of mismatching in such crowded fields. This radius was also chosen after careful consideration of the seeing for the observations, which was found to be between $\sim 0.63'' - 1.31''$ for the images used.

As most of these images are such crowded fields choosing the most efficient cross-matching radius is crucial so as to reduce the impact of incorrect matches but also reduces the number of stars that go unmatched.

3.4 Results

The output for each of these image matches were separated into their respective galaxies and plotted into CMDs using PYTHON. It should be noted that the magnitudes used are those described as "MAG AUTO" by SExtractor. This magnitude choice was made in preference to the other magnitude outputs provided by SExtractor as this provides an automatic aperture for the detections and is considered by the software developers to be the most reliable for this kind of observation. This magnitude uses an elliptical apperture through which magnitude is collected around a detected source.

3.4.1 Duplicates

Taking the initial output from the calibration pipeline and the source detection tables, initial CMDs were plotted. From these it was possible to see that there are likely duplicate observations of each star. This is due to overlapping image observations in each band. In order to not skew the statistics towards these duplicate detecitons, an effort was made to reduce the data further and, rather than just remove these duplicate points, merge them.

A PYTHON script was written to accomplish this on the entire data set. The code searches through the dataset for each star for any other coordinates within a predefined limit. In order to increase the reliability of the duplicate removal, a comparison to the I and V-band magnitudes should be made. This is carried out by using a limit on these magnitudes defined by the errors provided in the dataset. Comparing these magnitudes against the error limit will indicate if the duplicate is real or coincidental. If all of these conditions are met, the data point is assumed to be a duplicate, each duplicate is added to a list where the coordinates and magnitudes are mean-averaged and put back into the catalogue. This process in itself introduces a new source of error. This comes from potential mis-association of duplicates which is difficult to quantify. It should also be noted that this method of duplicate removal did not remove all of the duplicates present in the dataset. On further investigation it is likely this is due to the magnitude restriction during the removal process.

3.4.2 Selection Effects

During this data analysis there are several stages that will impact the accuracy of these results. Although some errors have been quantified and quoted with their relevant results, others are harder to quantify.

3.4.2.1 Initial Detection

For the specifics of the initial source detection with SExtractor see Section 2.1.4.6. The initial source detection is arguably the most important for defining the statistical reliability of the final catalogue. During this stage, aperture photometry was carried out. As some of these images are of very crowded fields, it is likely that aperture photometry is not the best method of source detection for these observations. The impact of the crowded fields on aperture photometry is likely skewed towards false negatives, meaning there are likely many sources that remain undetected. This will cause an incomplete catalogue compared to the objects actually being observed.

However, other detrimental selection effects are mitigated by the execution of the software by the pipeline. For example, the use of a windowed detection area outlined in Section 2.1.4.5, although this does have the detrimental effect of causing further false negatives. On balance, it is favourable to have more false negatives than false positives, as we at least have confidence that the sources we are seeing are real.

3.4.3 Hess Diagrams

Due to the large number of sources present in these observations, the initial CMDs are very densely populated diagrams, and it can be difficult to see all of the structure in some of the diagrams. Therefore, Hess (density) diagrams were plotted in an attempt to pick out as much structure as possible (Figures 3.3 to 3.10). Stellar population checks are performed against these diagrams in Section 4.1.

The Aquarius dIrr (Figure 1.2) is amongst one of the more sparsely populated galaxies. It is possible to see the tip of the RGB located at $(V - I) \sim 1$ mag and $I \sim 21$ mag. There is a lack of an obvious blue main sequence, although there is a strong foreground population.

IC 1613 (Figure 3.4) is a denser diagram and certainly benefits from a density plot. We can see the main sequence at $(V - I) \sim 1$ mag and $I \sim 23$ mag. The path of the RGB is quite clear in the density plot. There are also multiple AGB sequences seen at $(V - I) \sim 2$ mag.

The populations of LGS 3 (Figure 3.5) in the dense regions of the diagram we can see two major populations at I-band ~ 23 to 24 mag. It is likely that this is a side effect of varying completeness across the images used to generate this plot. Whilst not much structure can be seen there are a large number of foreground stars that cross the AGB region.

Extra structure can be seen in the densest regions of the diagram for NGC 6822 (Figure 3.6), other than the position and the intrinsic width of the RGB. There are multiple AGB sequences at $(V - I) \sim 3$ and 4 mag. There may also be a short blue main sequence at $(V - I) \sim 0$ mag.

Pegasus (Figure 3.7) and Phoenix (Figure 3.8) are not among the densest diagrams in these observations but the tracks of the RGB can be seen more clearly in the densest regions. For Pegasus we can also see a much brighter sequence of foreground stars. With Phoenix we can see that the analysis samples far below the RGB tip.

The Sagittarius dIrr (Figure 3.9) is not very useful as it shows mainly foreground stars. Therefore, we do not see almost any internal structure for this galaxy.

The diagram for WLM (Figure 3.10) shows a poorly populated foreground sequence at $(V - I) \sim 2.5$. This diagram is particularly red which may indicate that the V-band correction for this galaxy may not be correct or that there is a greater amount reddening due to dust than is taken into account.

Generally speaking the observed populations in these diagrams show the RGB tip and in some cases, i.e. Figure 1.3, also show an extent of the AGB populations quite clearly. Due to the direct nature of these observations there will also be a collection of foreground and background objects shown in these diagrams. The foreground objects will likely have a brighter I-band magnitude compared to their dIrr counterparts and therefore should be clustered at the higher I-band regions of the diagrams. The impact of forground contamination could be minimized by using a cut on RA and DEC to isolate the targets. This would not be helpful in the case of the Sagittarius and Aquarius dIrr as source detections are quite diffuse across the target fields, as can be seen in Figures 3.11 and 3.17. In this case a cut on a density of sourced might prove more useful however, neither of these methods have been employed at this stage and would be carried out in future work. Any background galaxies in the observing path may be difficult to differentiate due to the crowded nature of the observations. If neccesary, further quantification of this and removal of potential background galaxy sources could be accomplished through an analysis of the "stellarity" property calculated by SExtractor.

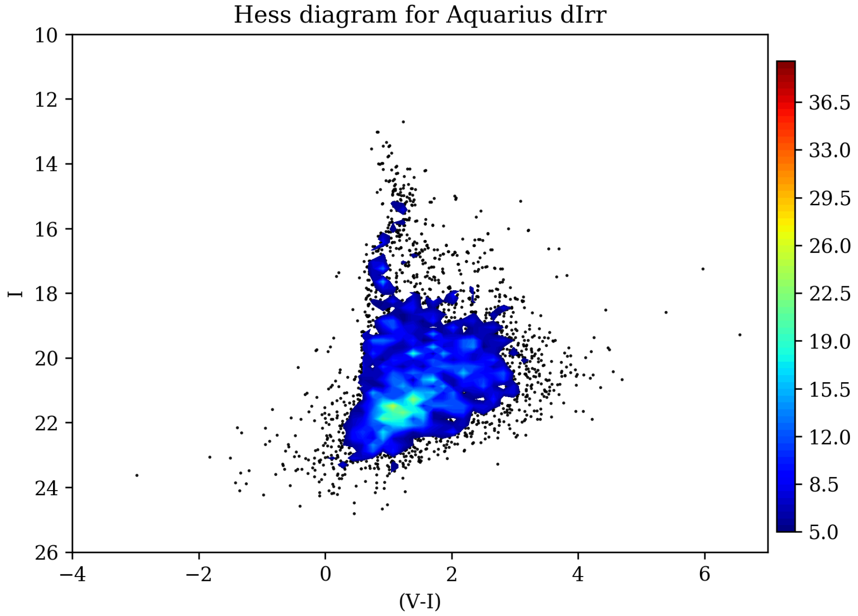

Figure 3.3: Hess diagram for Aquarius dIrr using VLT data.

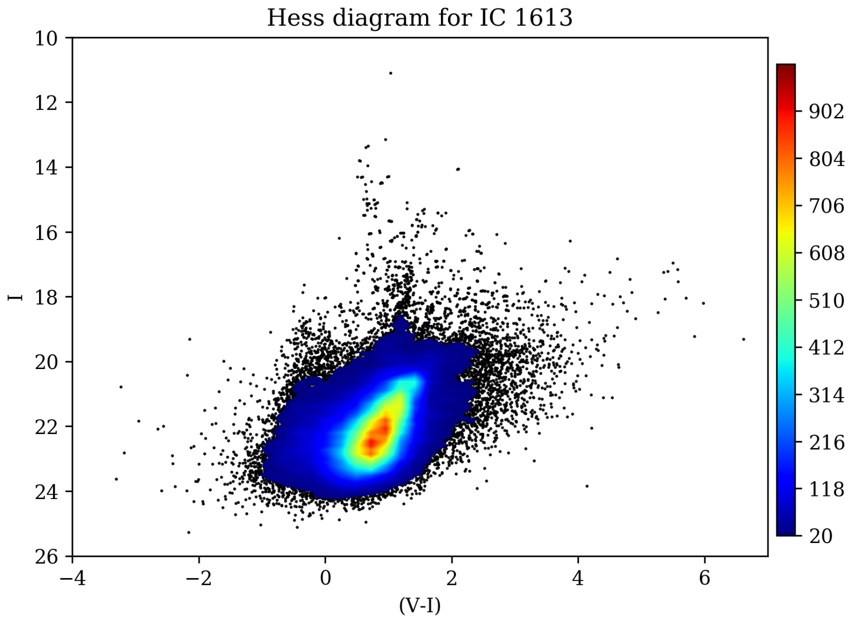

Figure 3.4: Hess diagram for IC 1613 using VLT data.

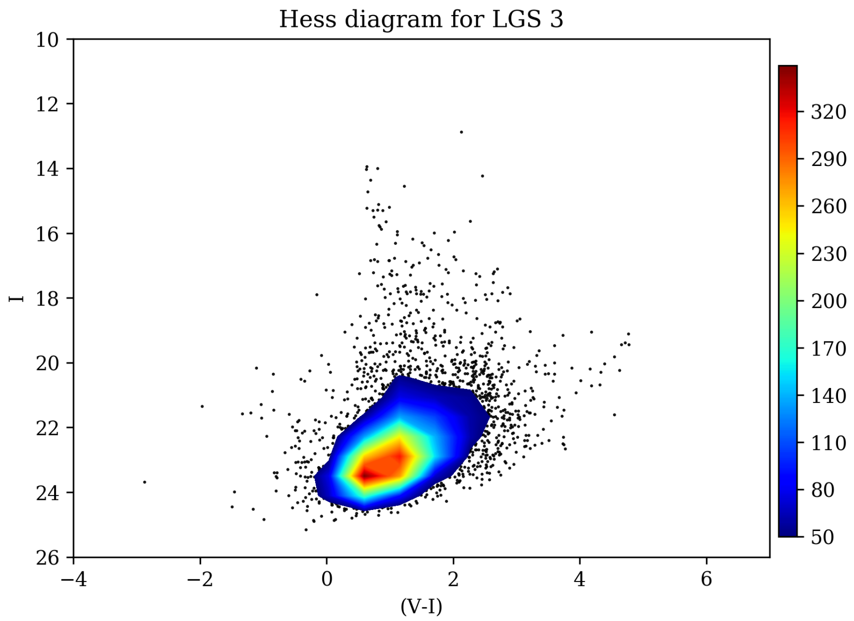

Figure 3.5: Hess diagram for LGS 3 using VLT data.

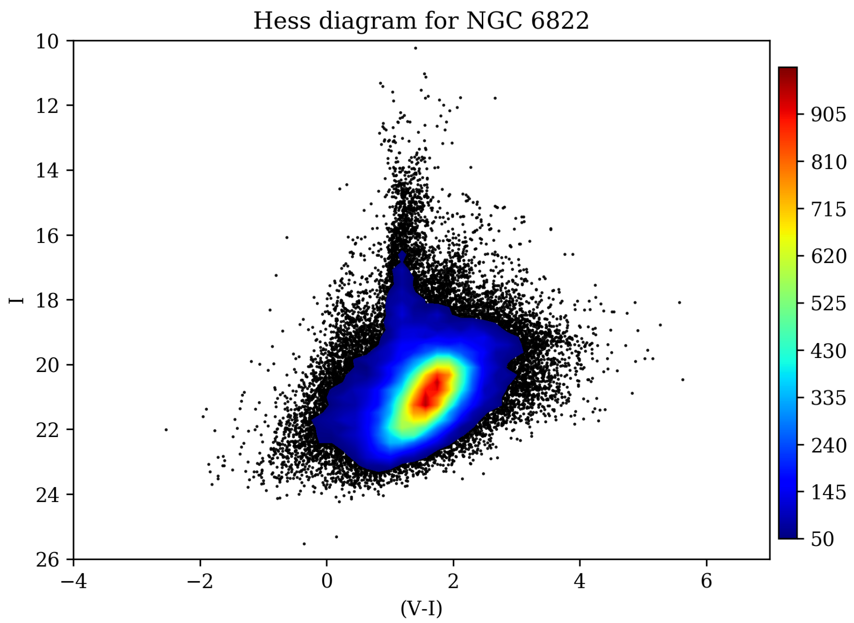

Figure 3.6: Hess diagram for NGC 6822 using VLT data.

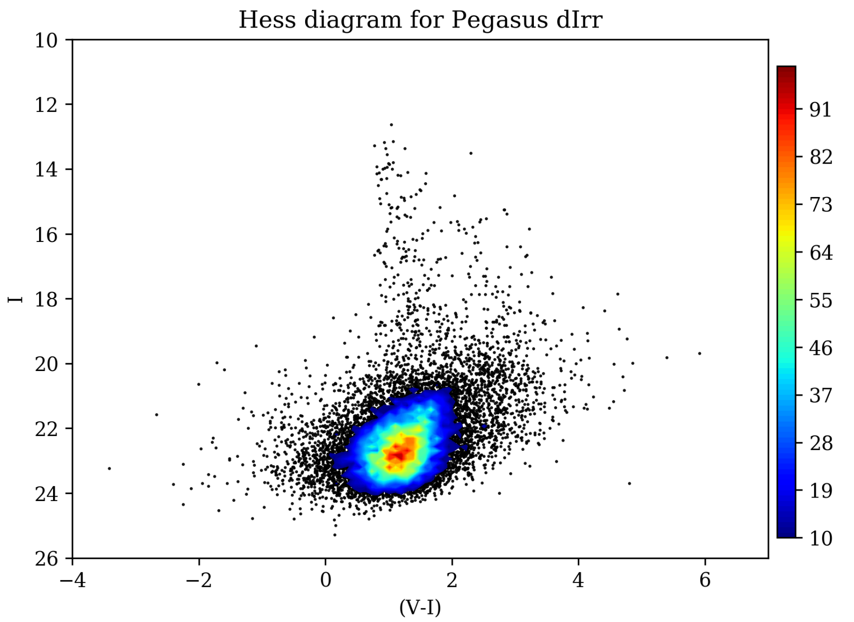

Figure 3.7: Hess diagram for Pegasus dIrr using VLT data.

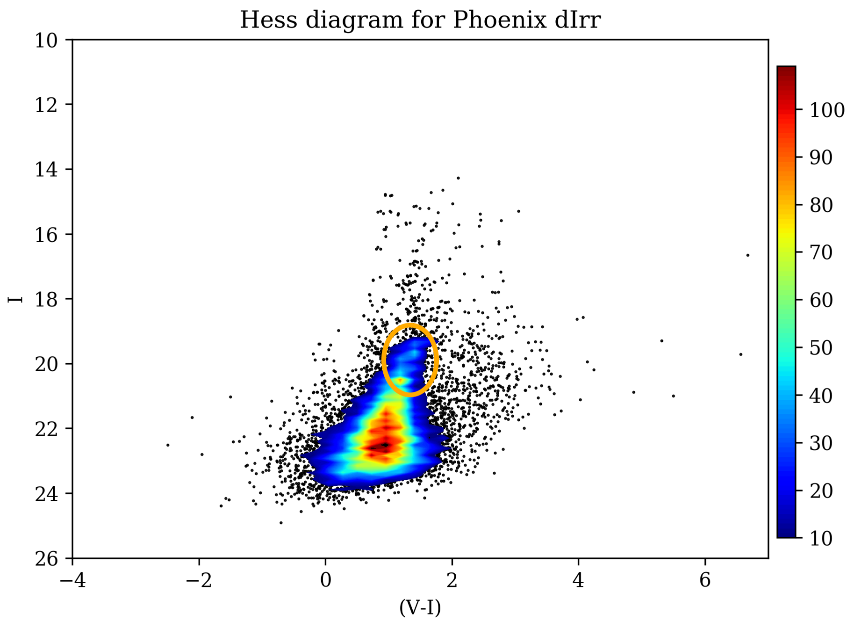

Figure 3.8: Hess diagram for Phoenix dIrr using VLT data. The circle highlights the RGB tip.

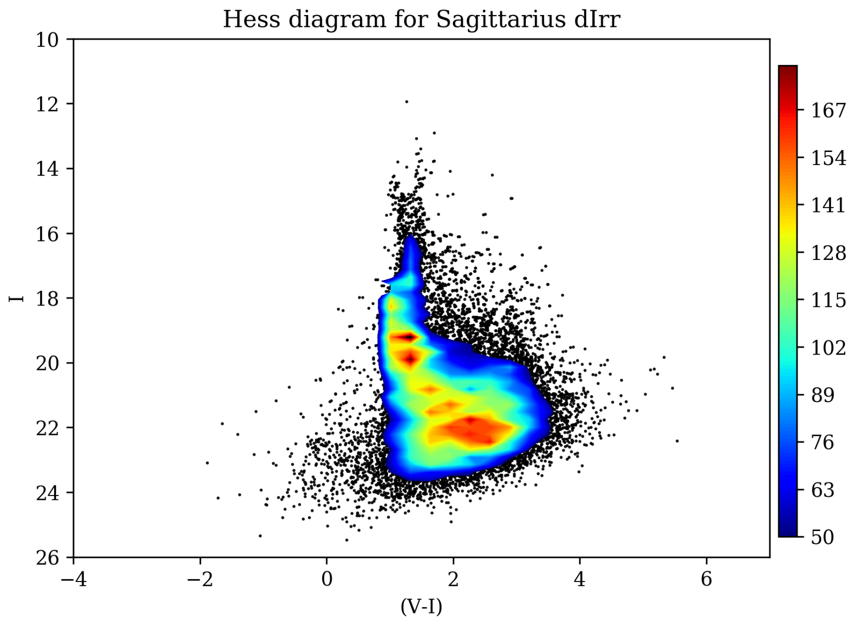

Figure 3.9: Hess diagram for Sagittarius dIrr using VLT data.

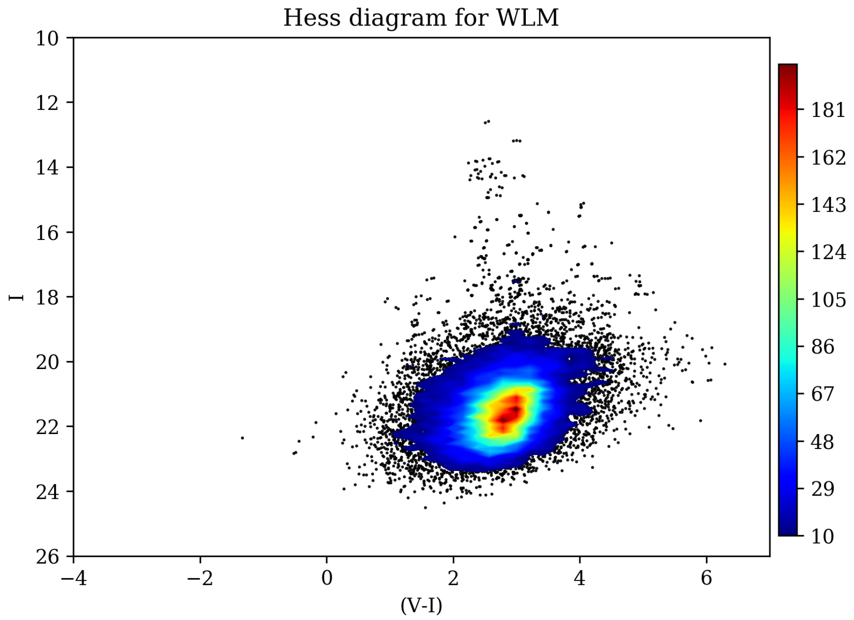

Figure 3.10: Hess diagram for WLM using VLT data.

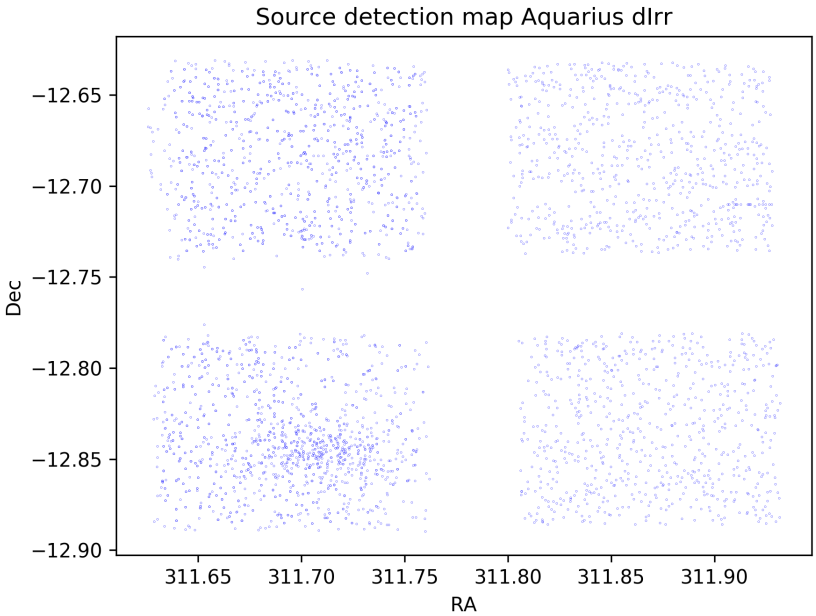

Figure 3.11: Source detection map for Aquarius dIrr after aperture photometry extraction. Axes are both represented in degrees.

3.5 Observation Statistics

Due to the large number of source detections the main use of these observations is with statistical analysis to see general trends.

General statistics of the observations for each galaxy can be seen in Table 3.1. Source detection maps can be seen in Figures 3.11 to 3.18.

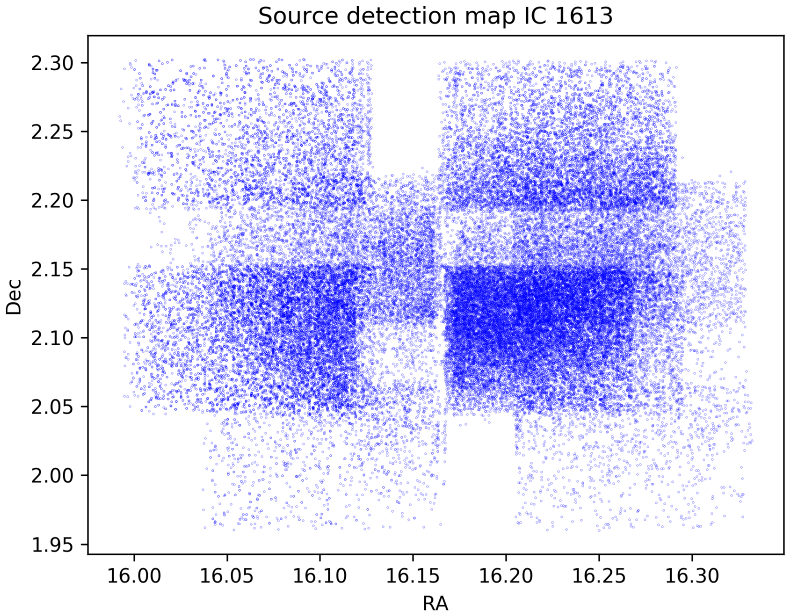

Figure 3.12: Source detection map for IC 1613 after aperture photometry extraction. Axes are both represented in degrees.

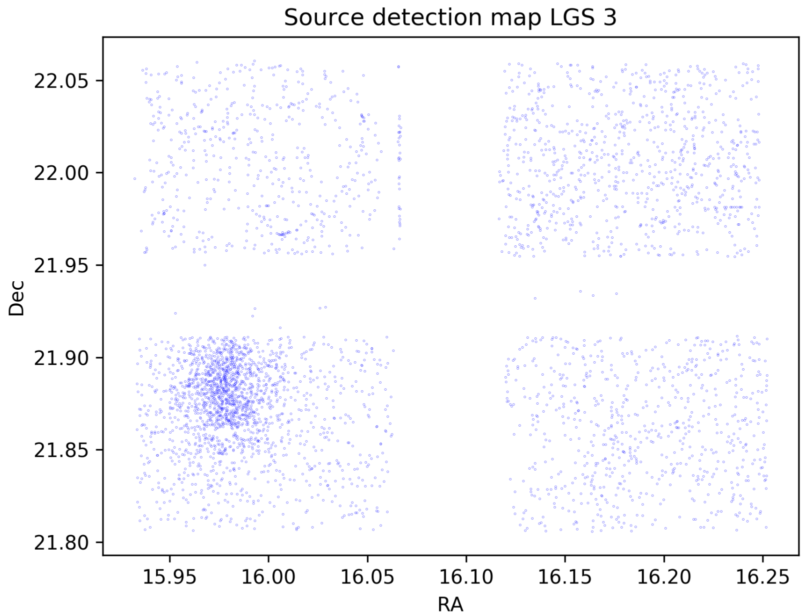

Figure 3.13: Source detection map for LGS 3 after aperture photometry extraction. Axes are both represented in degrees.

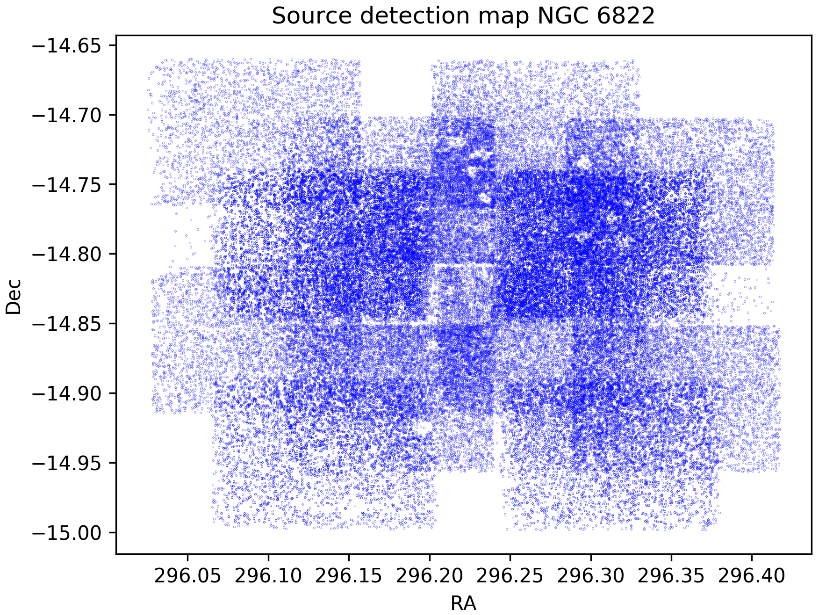

Figure 3.14: Source detection map for NGC 6822 after aperture photometry extraction. Axes are both represented in degrees.

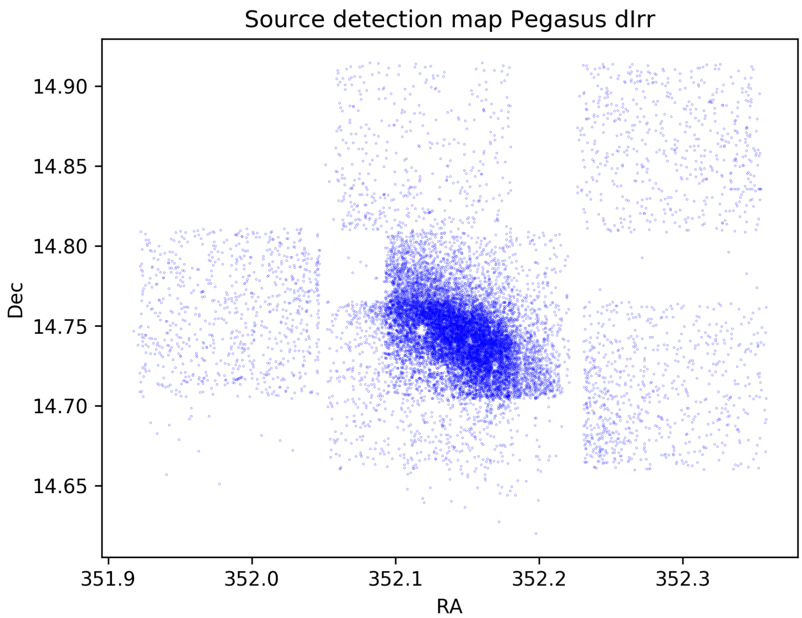

Figure 3.15: Source detection map for Pegasus dIrr after aperture photometry extraction. Axes are both represented in degrees.

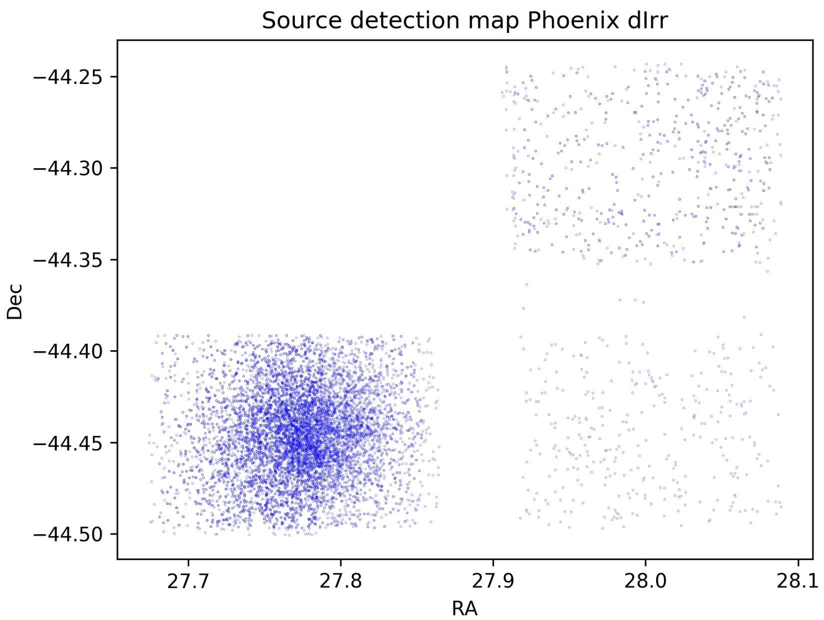

Figure 3.16: Source detection map for Phoenix dIrr after aperture photometry extraction. Axes are both represented in degrees.

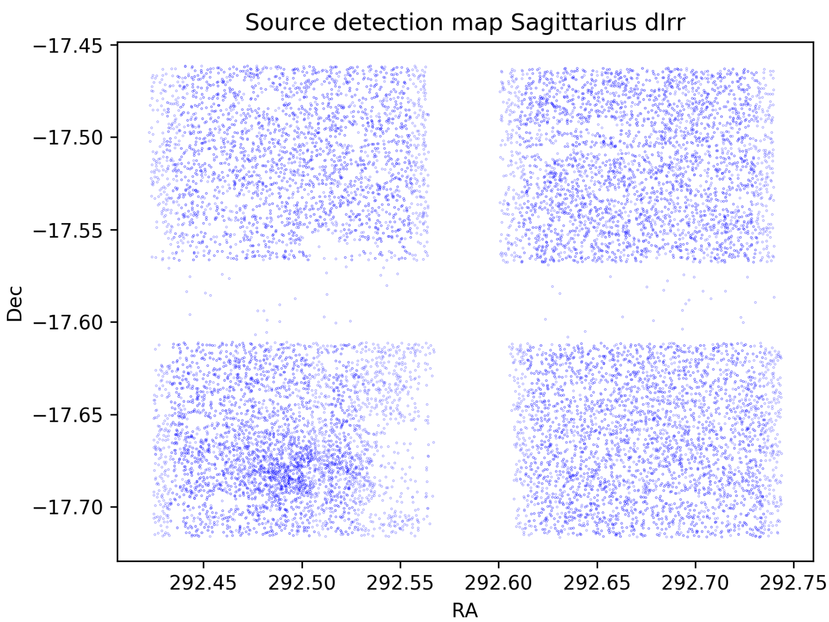

Figure 3.17: Source detection map for Sagittarius dIrr after aperture photometry extraction. Axes are both represented in degrees.

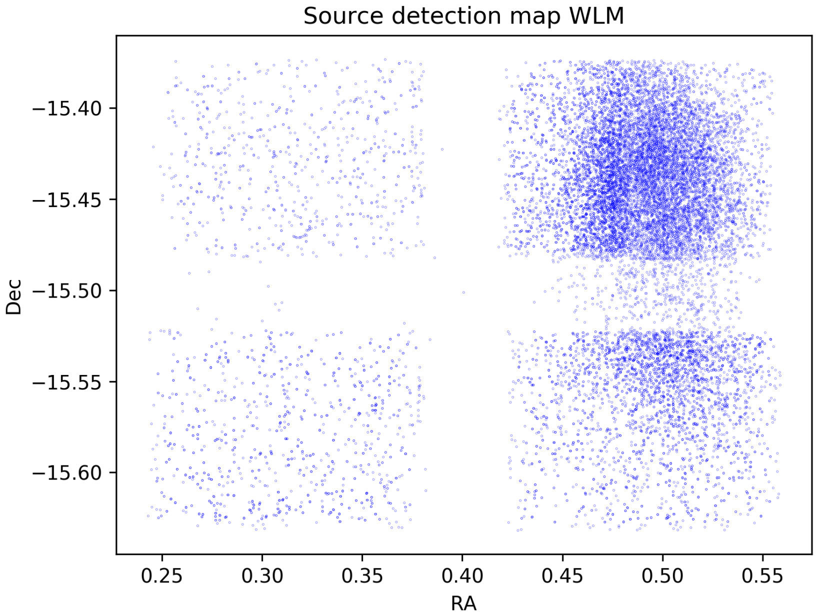

Figure 3.18: Source detection map for WLM after aperture photometry extraction. Axes are both represented in degrees.

Table 3.1: General statistics for the VLT observations of the eight dIrr galaxies.

Galaxy	Number of crossmatched sources	Mean m_I	Mean m_V
Aquarius dIrr	3860	22.631 ± 0.099	20.470 ± 0.097
IC 1613	69040	23.751 ± 0.17	22.153 ± 0.18
LGS 3	3922	24.530 ± 0.095	22.540 ± 0.73
NGC 6822	98737	22.889 ± 0.15	20.722 ± 0.15
Pegasus dIrr	16455	24.372 ± 0.058	22.576 ± 0.049
Phoenix dIrr	11518	23.798 ± 0.42	22.115 ± 0.050
Sagittarius dIrr	19706	22.939 ± 0.18	20.629 ± 0.33
WLM	18761	23.633 ± 0.33	21.837 ± 0.043

Chapter 4

Data in Context

While the data being discussed in this work consists of large data sets for each galaxy, it is still important to consider it in the context of the work that has come before and to consider where it will be useful in the future. The point-source catalogue produced in this work is intended to be useful in statistical analysis of metal-poor environments and analogues of the early Universe.

4.1 Stellar Populations

The [Fe/H] abundance is stellar population and age dependant. Here various stellar population isochrones are fitted to the VIMOS data in an attempt to illustrate the observed populations. This process provides a test of the observations made here and previous studies. If the reduction of this VIMOS data is good then the CMDs produced here should match those of previous studies. The isochrone fitting should also provide a good match, assuming the underlying assumptions are valid. The isochrones and stellar populations selected are not assumed to be exhaustive but are an attempt to draw together data from as many sources as possible in order to consider this data in the proper context.

It should also be noted that where the plotted isochrones do not fit well with the data, it is likely that sensitivity limits of the observations may prevent the

CMDs from extending much below the RGB tip where the isochrones terminate. In particular the isochrones used for the Sagittarius dIrr (Figure 4.7) are poor as they do not extend enough into the bright I-band region for the observed populations. It is also possible that the extinction corrections used here are insufficient or an incorrect distance modulus has been used. None of the sources in Table 4.1 provided their assumptions for [α/Fe] so it is also possible that their assumptions for this abundance is misaligned with the [α/Fe]$= +0.4dex$ assumed in the plotted isochrones.

Table 4.1: [Fe/H] quantities for the eight dIrr galaxies observed and relevant stellar populations. Each of the quantities are quoted with corresponding uncertainties, if available, and the source.

Name	Age (*Gyr*)	[Fe/H] (*dex*)	Reference
Aquarius dIrr	$\gtrsim 11.5$	-2.15	Cole et al. (2014)
Aquarius dIrr	$6-8$	-1.47	Cole et al. (2014)
Aquarius dIrr	$1-2$	-1.25	Cole et al. (2014)
IC 1613	15 (Blue edge, RGB)	-1.5	Dolphin et al. (2001)
IC 1613	10 (Red edge, RGB)	-1.1	Dolphin et al. (2001)
IC 1613	$0.01-0.5$ (Red Super Giants)	-1	Dolphin et al. (2001)
LGS 3	$11-13$	-1.94 ± 0.40	Miller et al. (2001)
LGS 3	$5-8$	-1.34 ± 0.25	Miller et al. (2001)
LGS 3	$1-2$	-1.24 ± 0.26	Miller et al. (2001)
NGC 6822	15	-1.53	Gallart, Aparicio & Vilchez (1996)
NGC 6822	6.3	-1.13	Gallart, Aparicio & Vilchez (1996)
NGC 6822	3 (RGB slope)	-1.0 ± 0.3[a]	Davidge (2003)
Pegasus dIrr	10	-1.53	Aparicio & Gallart (1995)
Pegasus dIrr	6.5	-1.13	Aparicio & Gallart (1995)
Pegasus dIrr	4	-0.53	Aparicio & Gallart (1995)
Phoenix dIrr	12.6 ± 0.4	-1.67 ± 0.21	Hidalgo et al. (2013)
Phoenix dIrr	5.9 ± 0.1	-1.54 ± 0.14	Hidalgo et al. (2013)
Phoenix dIrr	1.4	-1.08 ± 0.07	Hidalgo et al. (2013)
Sagittarius dIrr	10.5 ± 1.5	-1.3 ± 0.2	Layden & Sarajedini (2000)
Sagittarius dIrr	5.0 ± 1.0	-0.7 ± 0.2	Layden & Sarajedini (2000)
Sagittarius dIrr	$0.5-3$	-0.4 ± 0.3	Layden & Sarajedini (2000)
WLM	12	-2.18 ± 0.28	Dolphin (2000)
WLM	10 (Halo)	-1.4 ± 0.2	Minniti & Zijlstra (1996)
WLM	3	-1.34 ± 0.14	Dolphin (2000)

[a] This value may be underestimated by as much as 0.05 *dex* according to Davidge (2003).

4.1.1 Stellar Parameters

There are several parameters that will impact the tracks shown on the isocrhones. A shift to the positions of the isochrones is also caused by differing ages. As the isochrones are provided in absolute magnitude but the CMDs are given in apparent magnitude, a correction for the distance to each galaxy must be applied. This has the effect of decreasing the magnitude of the plotted isochrones. Extinction must also be taken into account when applying these isochrones as this will cause a reddening of the observations which must be corrected for in the isochrones.

4.1.2 Isochrone Parameters

Accurate placement of isochrones on the CMD requires several corrections beyond the specific stellar paramters of the isochrones. The distance modulus used in fitting these isochrones to each galaxy are shown in Table 4.2. Extinction must also be corrected for when plotting these isochrones. Data for these modulii are found in Schlafly & Finkbeiner (2011) and are taken from a recalibration of previous infrared dust maps. The extinction corrections used are shown in Table 4.3.

Table 4.2: Distance modulus quantities for the eight dIrr galaxies observed. Each of the quantities are quoted with corresponding uncertainties and the source.

Name	Distance Modulus, μ (Mag)	Reference
Aquarius dIrr	25.02 ± 0.08	Tully et al. (2013)
IC 1613	24.26 ± 0.07	Bhardwaj et al. (2016)
LGS 3	24.05 ± 0.06	Tully et al. (2013)
NGC 6822	24.43 ± 0.06	Bhardwaj et al. (2016)
Pegasus dIrr	25.41 ± 0.06	Tully et al. (2013)
Phoenix dIrr	23.13 ± 0.06	Tully et al. (2013)
Sagittarius dIrr	25.17 ± 0.10	Tully et al. (2013)
WLM	24.92 ± 0.07	Bhardwaj et al. (2016)

The specific stellar parameters used were chosen due to the expected properties of the environments being studied. Therefore, in order to ascertain if the fit is a good one, and the parameters assumed are appropriate, the RGB tip shown in CMDs should be matched to the tip of the isochrones. The parameters that were assumed are $Y = 0.25$ and [α/Fe]= 0.40. [α/Fe]= 0.40 was chosen due to the metal poor nature of the evnironments being observed. The [α/Fe] depends on the frequencies of type Ia and II supernovae. Type Ia will generally produce more iron peak elements and reduce the ratio of α to Fe elements. Whereas, Type II supernovae will produce more α elements and have the reverse effect to Type Ia. It is not believed that enough Type Ia supernovae have occured in these environments to have a significant impact.

Table 4.3: V and I-band extinction corrections. All corrections are taken from the re-calibration of previous infrared based dust maps and are found in Schlafly & Finkbeiner (2011).

Name	Assumed A_V (mag)	Assumed A_I (mag)
Aquarius dIrr	0.138	0.076
IC 1613	0.068	0.038
LGS 3	0.111	0.061
NGC 6822	0.646	0.355
Pegasus dIrr	0.187	0.102
Phoenix dIrr	0.044	0.024
Sagittarius dIrr	0.388	0.186
WLM	0.104	0.057

4.1.3 Final Isochrones

Taking the previous arguments into account, the Dartmouth Stellar Evolution Program (DSEP)[1] isochrones were used as they allow variations to Y and [α/Fe] to be considered. However, a potential drawback in using these isochrones is they do not show evolutionary stages beyond the RGB tip, whereas the data used here

[1]DSEP data used is present at http://stellar.dartmouth.edu/models.index.html

do not show much below the RGB tip. This is due to the sensitivity limit for these data of $V \sim 24$ mag and $I \sim 22$ mag.

4.1.4 Isochrone Plots

Using the data in Table 4.1, isochrones were plotted for each galaxy. The isochrones chosen are not considered to be exhaustive but rather to highlight periods of interest, such as peaks in star formation, where larger differences in [Fe/H] occur. These plots are seen in Figures 4.1 to 4.8.

It is clear that, even with the corrections applied to the dataset and the isochrones, there is not a good fit with these isochrones. Specifically, Figure 20 in Gallart, Aparicio & Vilchez (1996) compared to Figure 4.4 shows an obvious offset when comparing the isochrone locations. Some basic modelling was attempted by varying the values for [Fe/H] for the oldest observed populations but this did not correct the isochrone fit to the bulk population, it is also possible that [α/Fe] could be less that +0.4 which would also shift the isochrones to the left of these plots. This would require further investigation and quatification with external datasets. The remaining isochrone parameters are unlikely to be severely incorrect due to the environments in which these populations are present. Therefore, the most obvious assumption is that the magnitude corrections applied to the catalogue are insufficient. Upon closer investigation, this is also unlikely as the positions of key features on the Hess diagram of IC 1613 are consistent with other datasets, such as those in work by Skillman et al. (2014). It is also possible that the literature contains poor values for the population analysis used in Table 4.1. This is reinforced by the sparsity of data for this kind of stellar population analysis for these galaxies in the literature. The poor values could be in terms of [Fe/H] or [α/Fe], Therefore this poor fitting requires deeper investigation in the future.

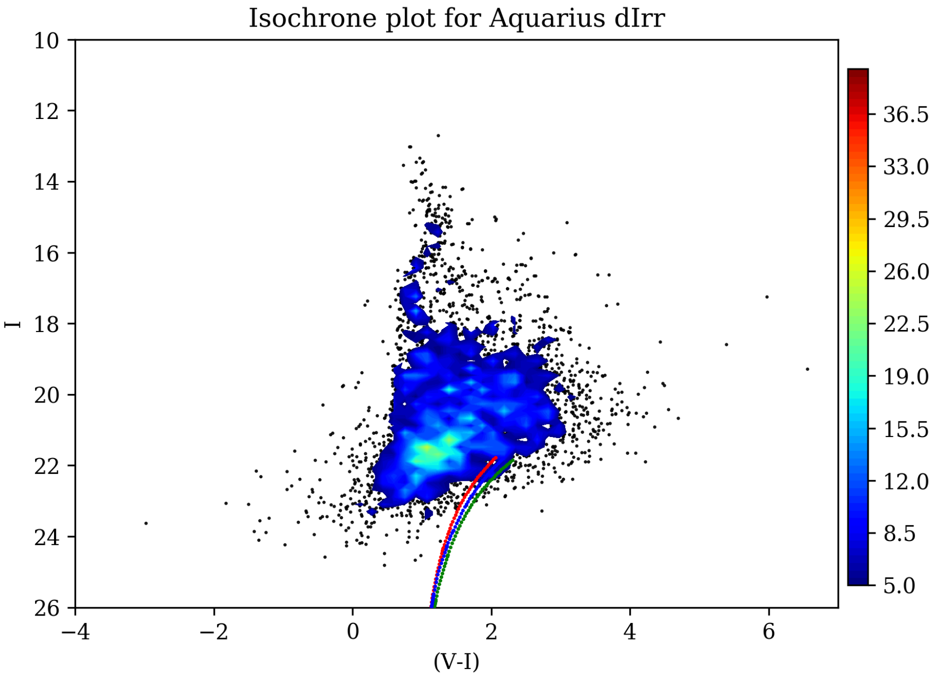

Figure 4.1: Hess (density) diagram of stars in the Aquarius dIrr galaxy. Isochrones are shown at [Fe/H] = –2.15 *dex* and 11.5 *Gyr* (red), –1.47 *dex* and 7 *Gyr* (green), and –1.25 *dex* and 1.5 *Gyr* (blue). References and other assumed parameters are given in Tables 4.1 to 4.3.

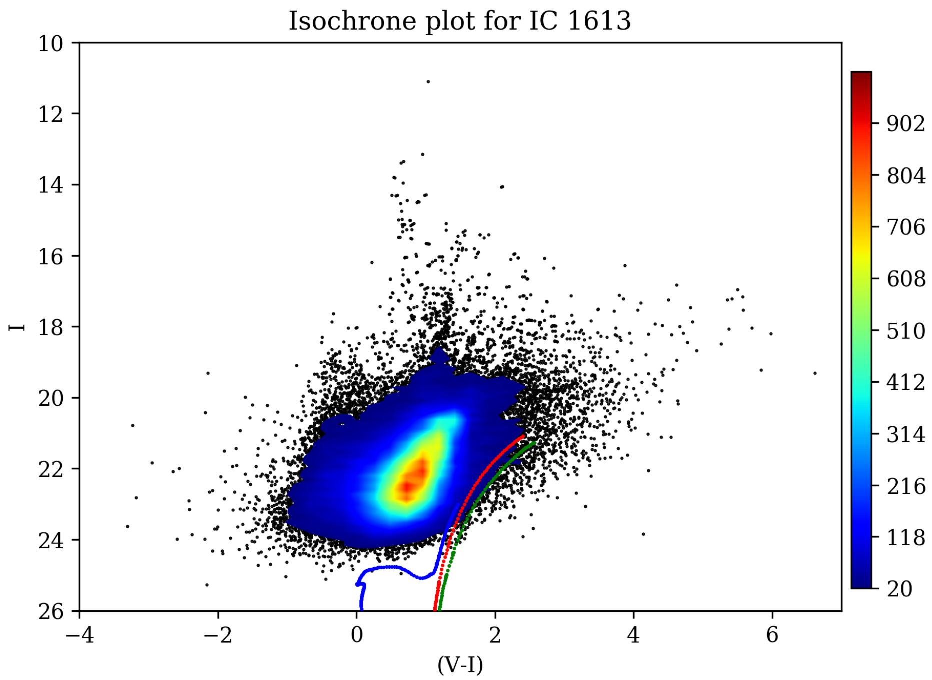

Figure 4.2: Hess diagram for IC 1613 using VLT data. Isochrones are shown at [Fe/H] = –1.5 *dex* for 15 *Gyr* (red), –1.1 *dex* for 10 *Gyr* (green), and –1 *dex* for 1 *Gyr* (blue). References and other assumed parameters are given in Tables 4.1 to 4.3. Note that 1 *Gyr* is outside the range stipulated in Table 4.1 however no younger isochrones were available from DSEP.

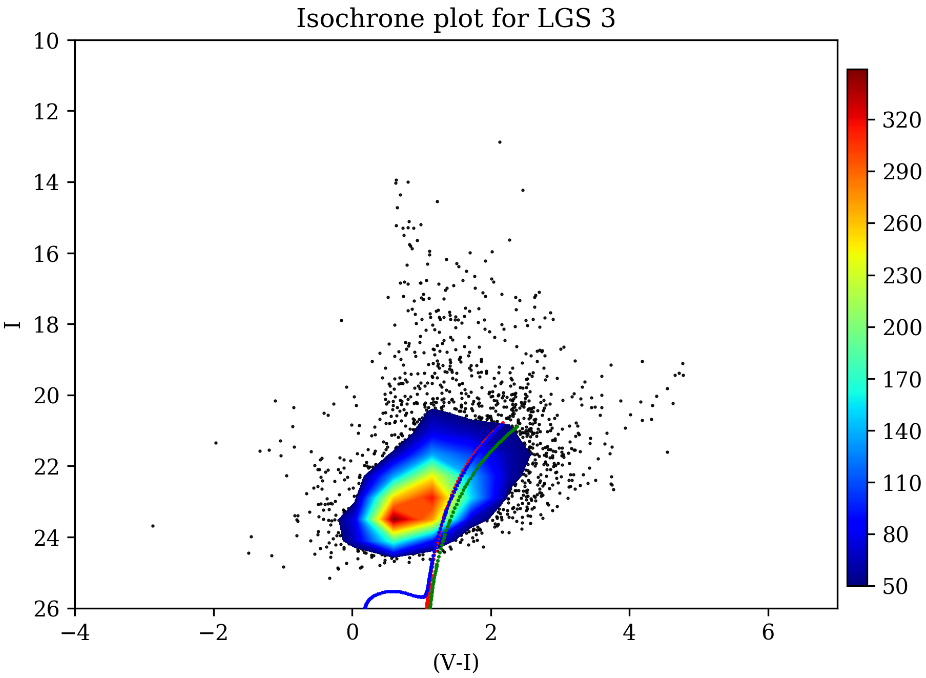

Figure 4.3: Hess diagram for LGS 3 using VLT data. Isochrones are shown at [Fe/H] = –1.94 *dex* for 13 *Gyr* (red), –1.34 *dex* for 8 *Gyr* (green), and –1.24 *dex* for 2 *Gyr* (blue). References and other assumed parameters are given in Tables 4.1 to 4.3.

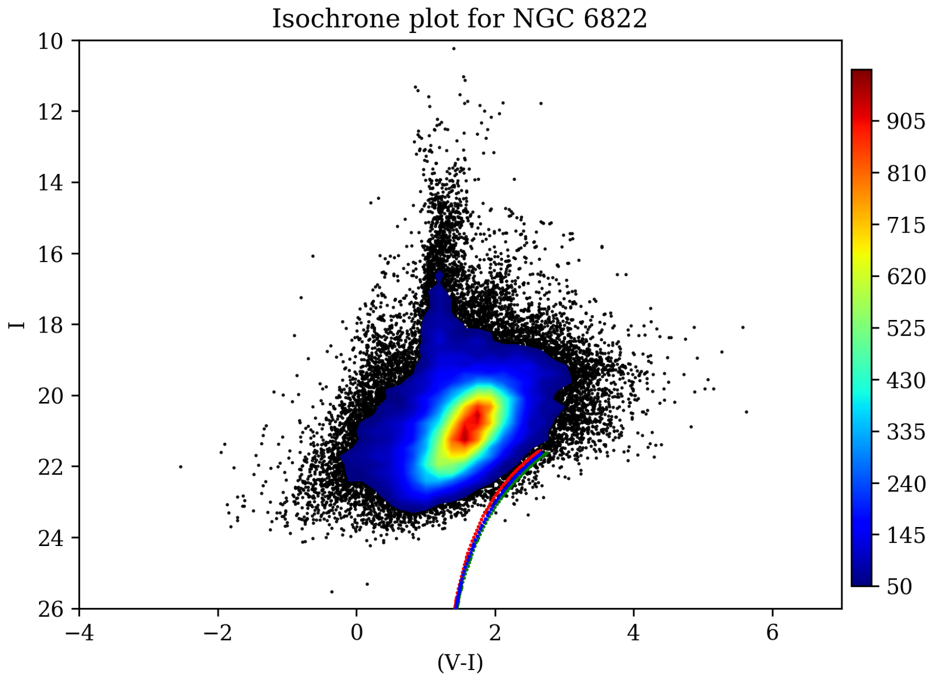

Figure 4.4: Hess diagram for NGC 6822 using VLT data. Isochrones are shown at [Fe/H] = –1.53 *dex* for 15 *Gyr* (red), –1.13 *dex* for 6.3 *Gyr* (green), and –1.0 *dex* for 3 *Gyr* (blue). References and other assumed parameters are given in Tables 4.1 to 4.3.

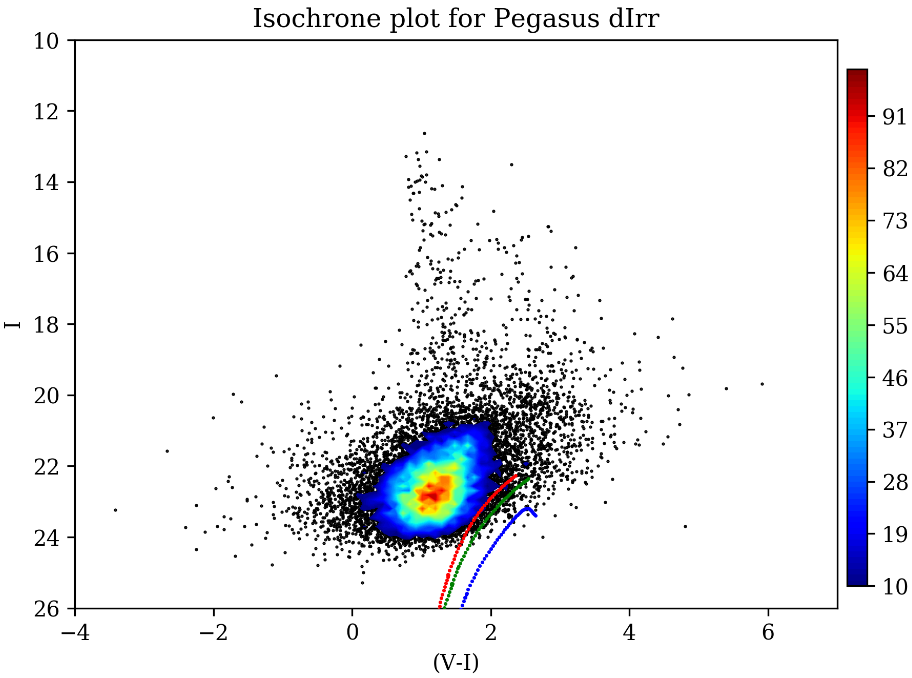

Figure 4.5: Hess diagram for Pegasus dIrr using VLT data. Isochrones are shown at [Fe/H] = –1.53 *dex* for 10 *Gyr* (red), –1.13 *dex* for 6.5 *Gyr* (green), and –0.53 *dex* for 4 *Gyr* (blue). References and other assumed parameters are given in Tables 4.1 to 4.3.

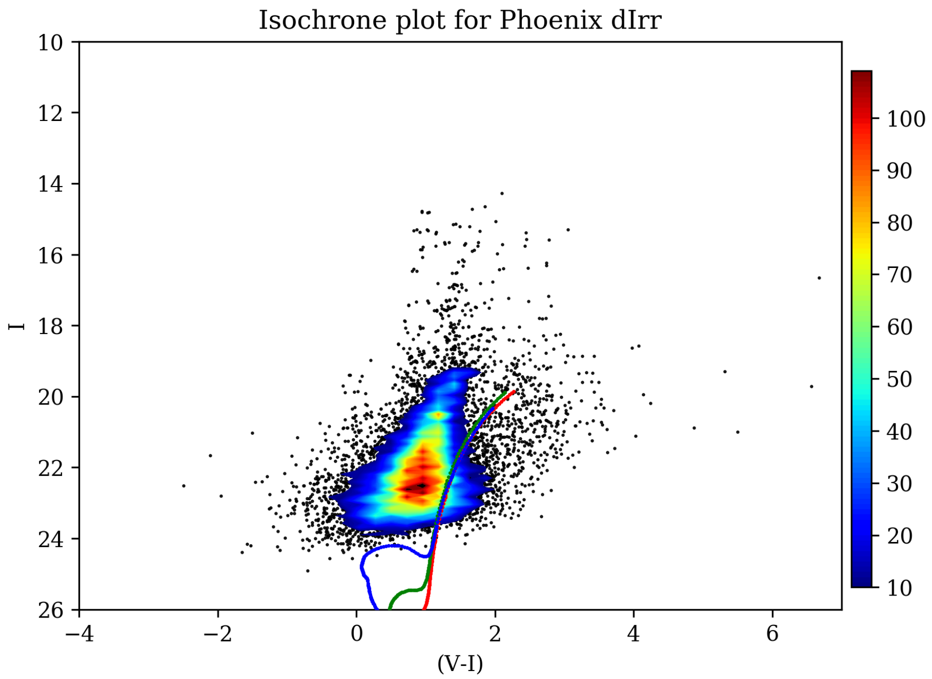

Figure 4.6: Hess diagram for Phoenix dIrr using VLT data. Isochrones are shown at [Fe/H] = –1.67 *dex* for 12.6 *Gyr* (red), –1.54 *dex* for 5.9 *Gyr* (green), and –1.08 *dex* for 1.4 *Gyr* (blue). References and other assumed parameters are given in Tables 4.1 to 4.3.

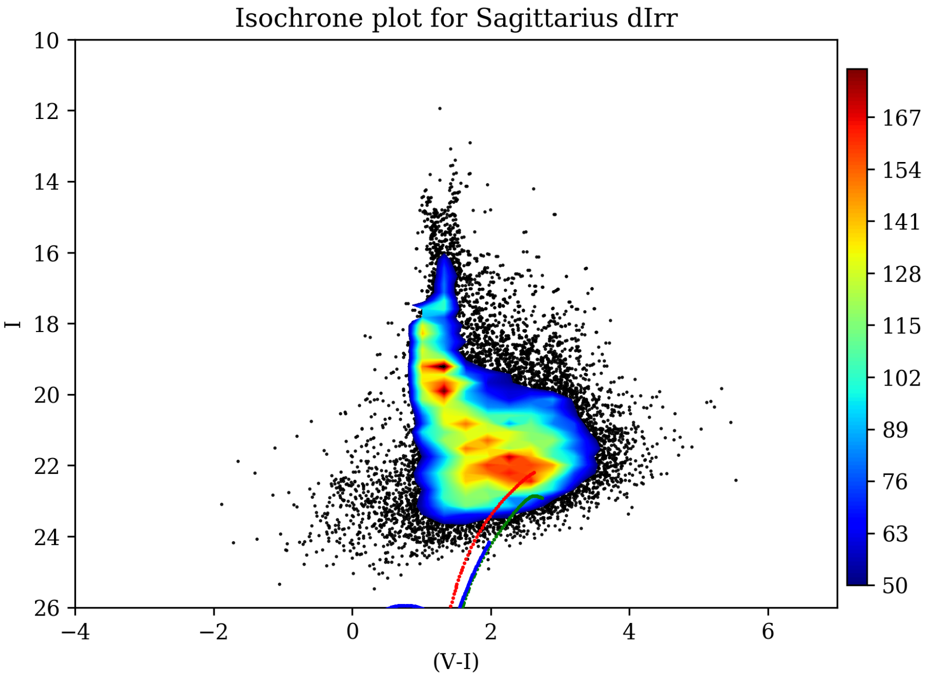

Figure 4.7: Hess diagram for Sagittarius dIrr using VLT data. Isochrones are shown at [Fe/H] = –1.3 *dex* for 10.5 *Gyr* (red), –0.7 *dex* for 5.0 *Gyr* (green), and –0.4 *dex* for 1.0 *Gyr* (blue). References and other assumed parameters are given in Tables 4.1 to 4.3.

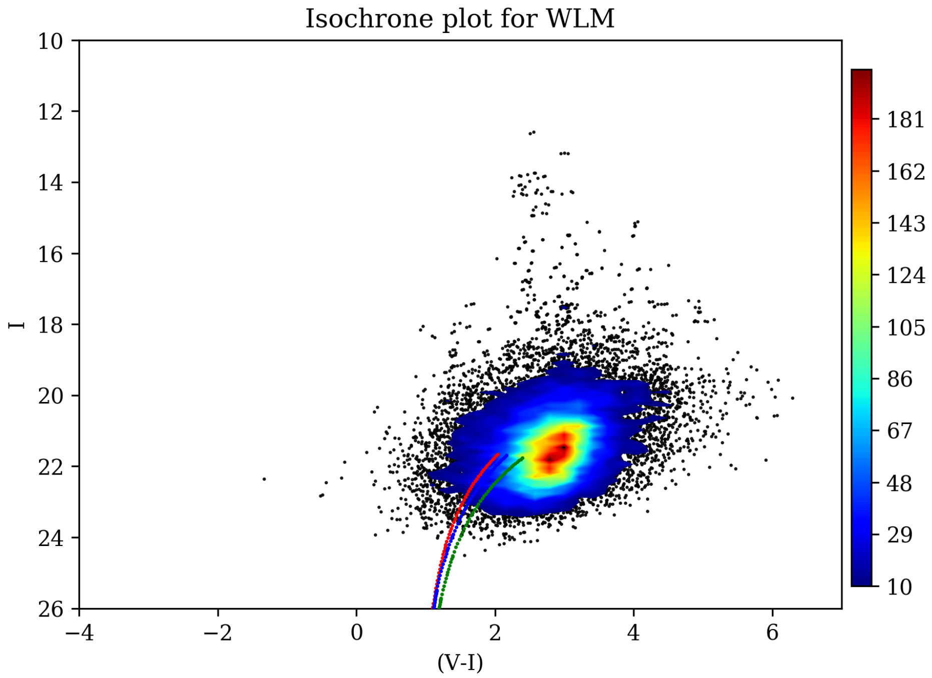

Figure 4.8: Hess diagram for WLM using VLT data. Isochrones are shown at [Fe/H] = –2.18 *dex* for 12 *Gyr* (red), –1.4 *dex* for 10 *Gyr* (Halo) (green), and –1.34 *dex* for 3 *Gyr* (blue). References and other assumed parameters are given in Tables 4.1 to 4.3.

4.2 DUSTiNGS

Dust in Nearby Galaxies with *Spitzer* (DUSTiNGS) is a survey designed to detect evolved stars as they are producing dust (Boyer et al. 2015b). The survey covered 50 dwarf galaxies, seven of which were also observed with VIMOS for this work.

DUSTiNGS made observations of these galaxies at $3.6\mu m$ and $4.5\mu m$ using the InfraRed Array Camera (IRAC) aboard the *Spitzer Space Telescope*. The survey produced two catalogues of point-sources, the full catalogue and the Good Source catalogue (GSC). For the crossmatching with this data only the GSC was used. This has the benefit of removing many of the false positives or errors that may have occured in the the full catalogue. However, using the reduced dataset may also adversely impact data completeness.

4.2.1 Data Crossmatch

All of the galaxies observed with VIMOS outlined in this work were also observed with *Spitzer* during this survey with the exception of NGC 6822. The aim of this data crossmatch is to identify known variable sources and reddened sources that may indicate a carbon star. The locations of these crossmatched sources are shown in Figures 4.9 to 4.15. In order to crossmatch this data an expanded radius of $2''$ was used to more closely match of the point-spread function size of the IRAC instrument. The angular resolution of IRAC is $1.2'' \times 1.2''$ (Caltech 2015).

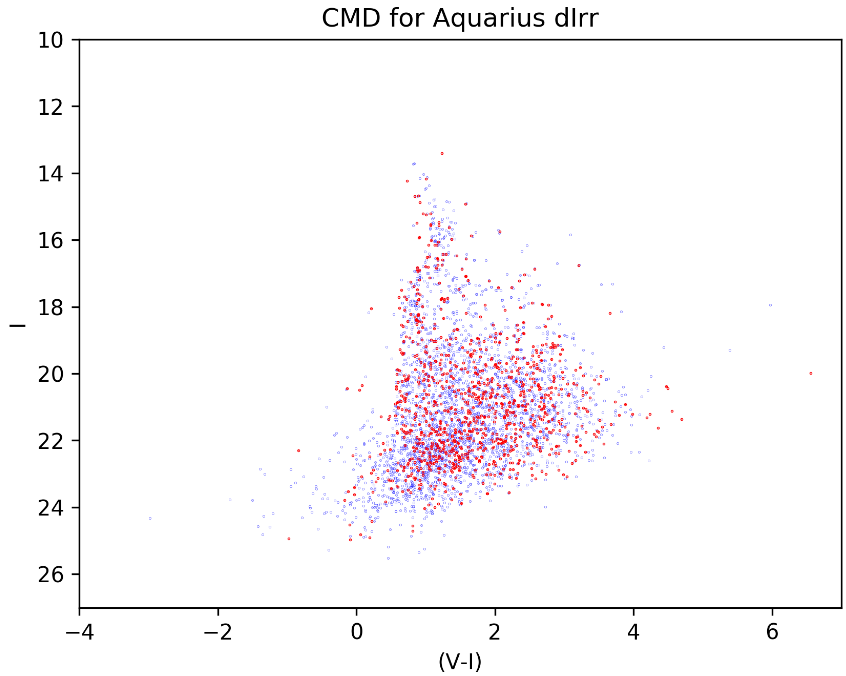

Figure 4.9: CMD for Aquarius dIrr VLT data (blue) with Spitzer GSC crossmatch (red).

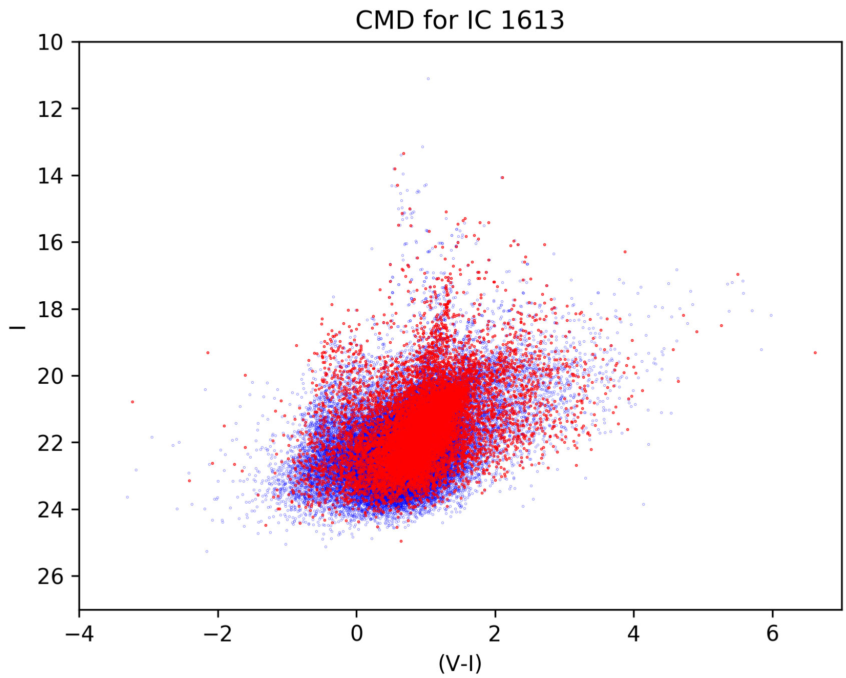

Figure 4.10: CMD for IC 1613 VLT data (blue) with Spitzer GSC crossmatch (red).

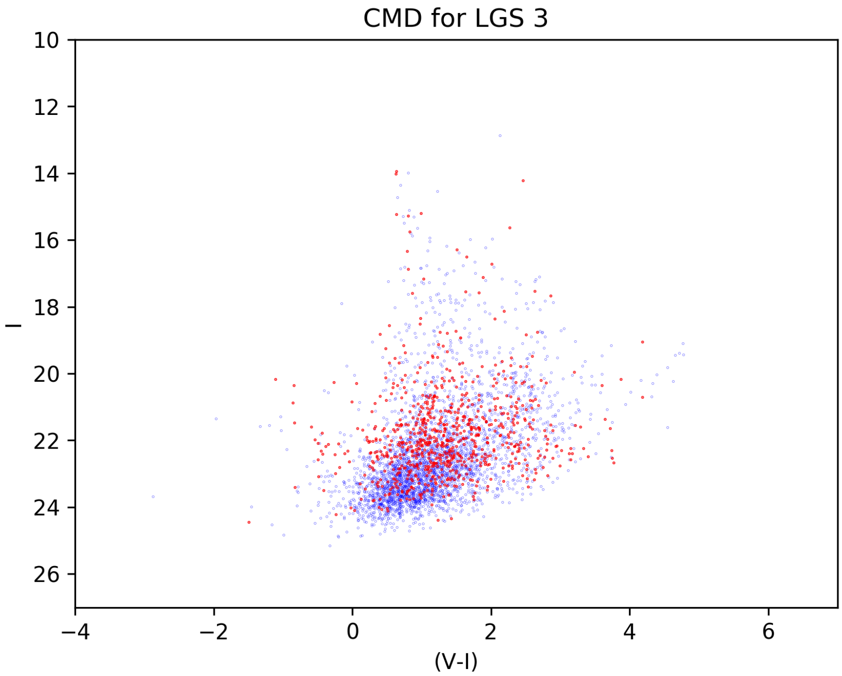

Figure 4.11: CMD for LGS 3 VLT data (blue) with Spitzer GSC crossmatch (red).

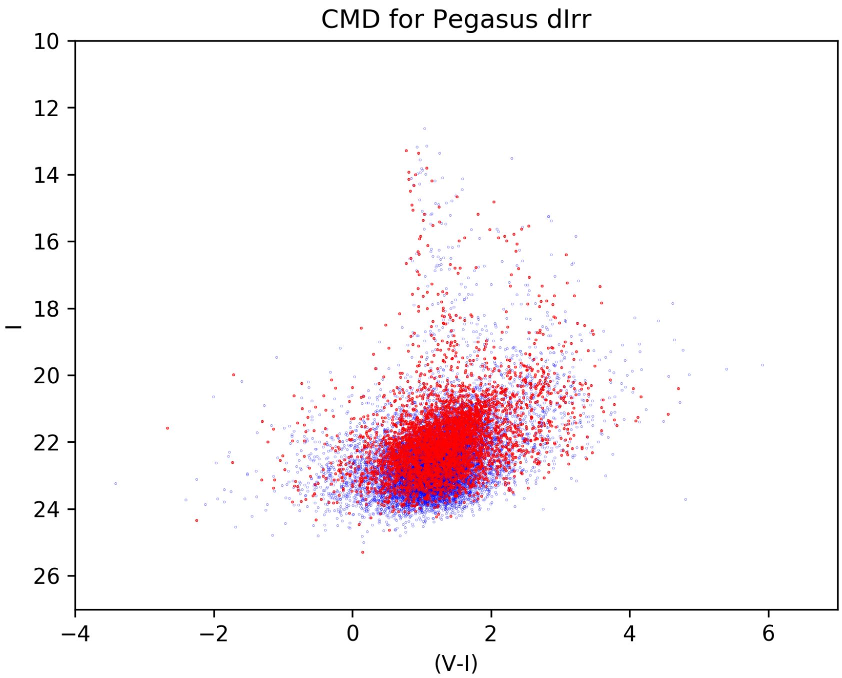

Figure 4.12: CMD for Pegasus dIrr VLT data (blue) with Spitzer GSC crossmatch (red).

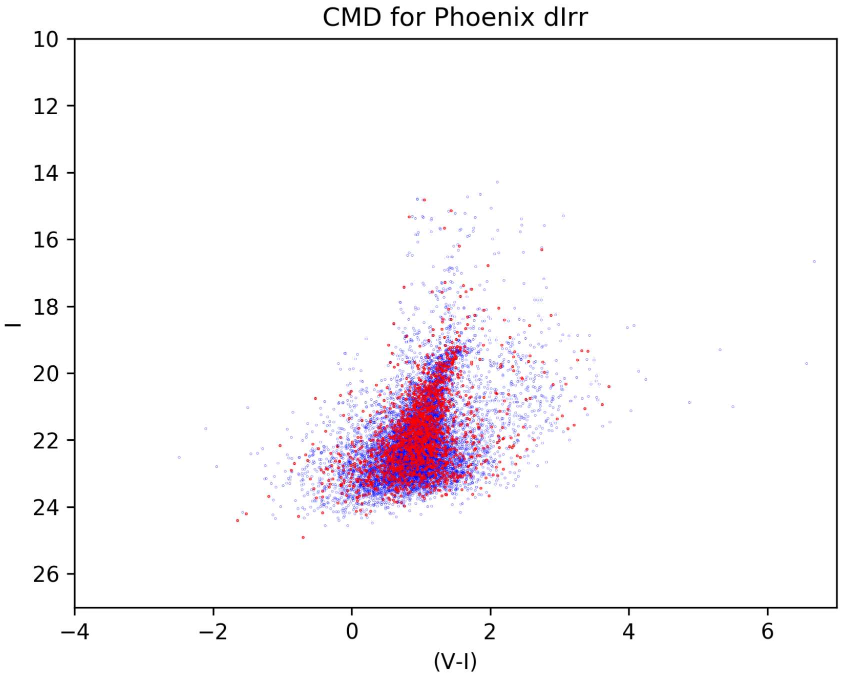

Figure 4.13: CMD for Phoenix dIrr VLT data (blue) with Spitzer GSC crossmatch (red).

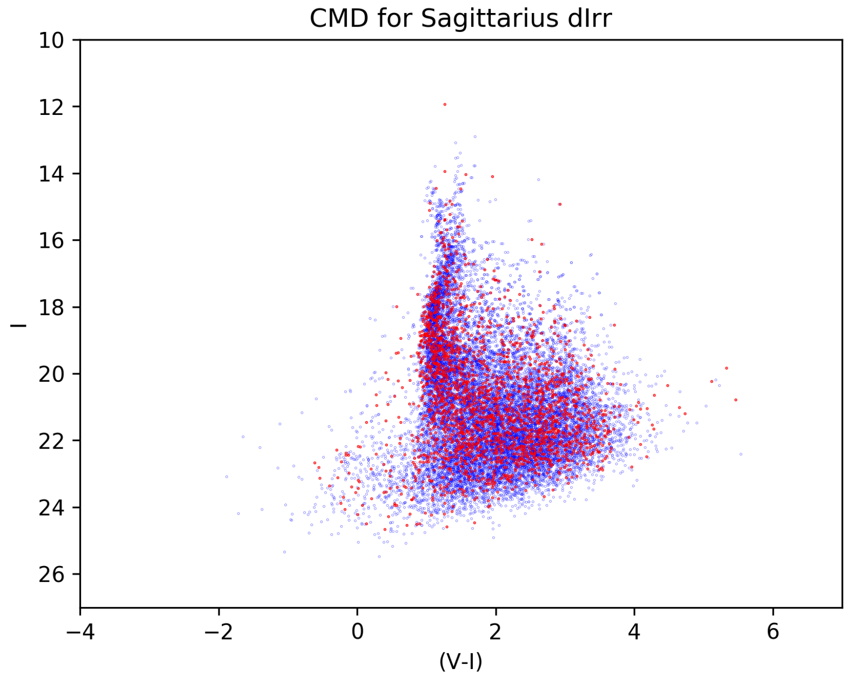

Figure 4.14: CMD for Sagittarius dIrr VLT data (blue) with Spitzer GSC crossmatch (red).

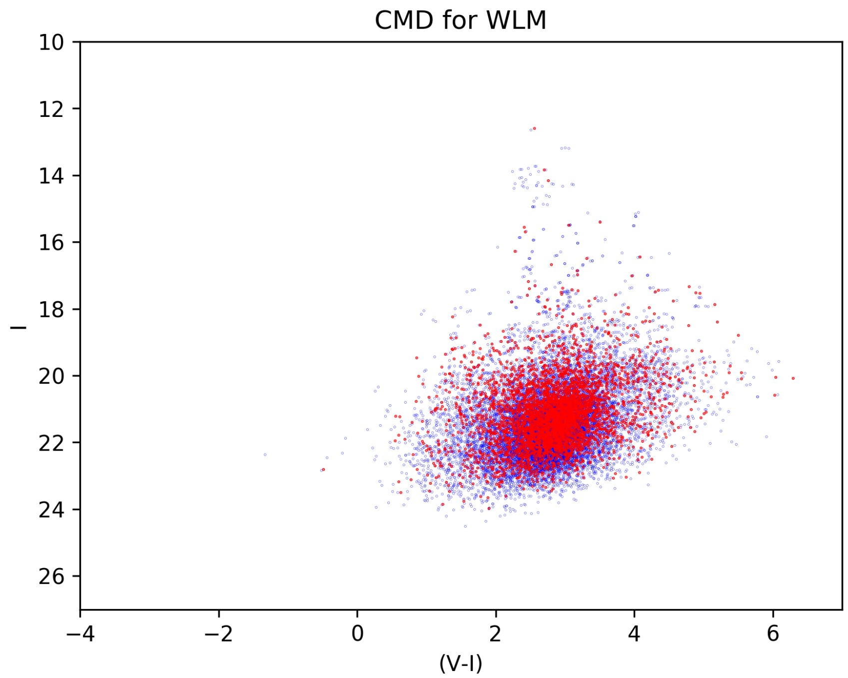

Figure 4.15: CMD for WLM VLT data (blue) with Spitzer GSC crossmatch (red).

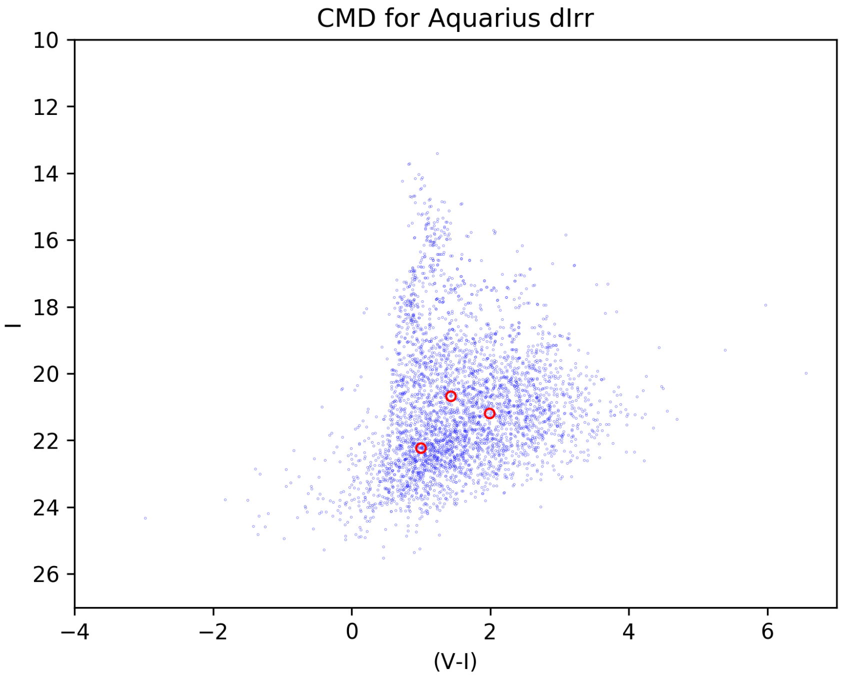

Figure 4.16: CMD for Aquarius dIrr VLT data (blue) with Spitzer variable sources (red).

A reduced dataset taken from the GSC of identified variable stars and AGB stars was also crossmatched taken from Boyer et al. (2015a). These data are presented in Figures 4.16 to 4.22.

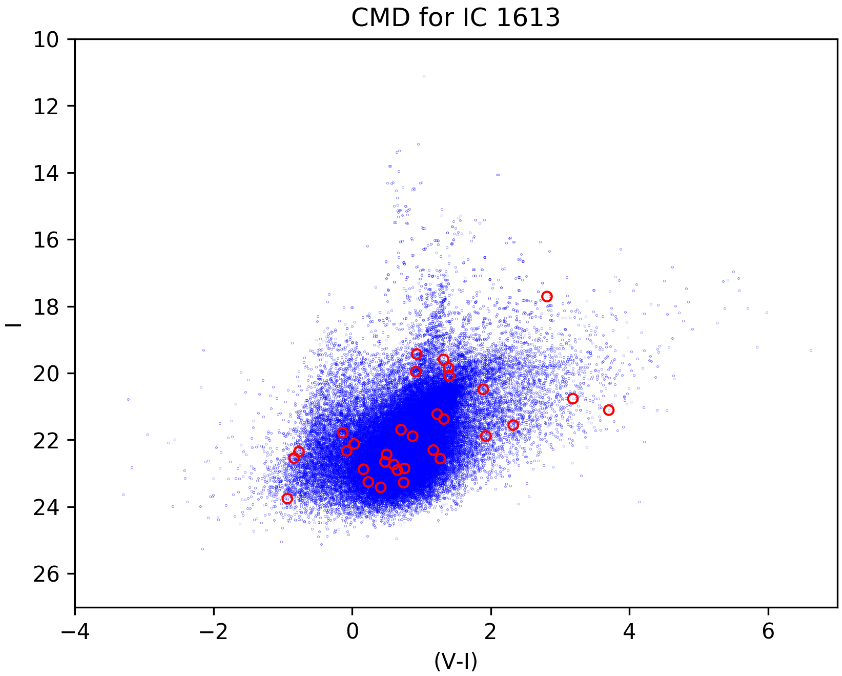

Figure 4.17: CMD for IC 1613 VLT data (blue) with Spitzer variable sources (red).

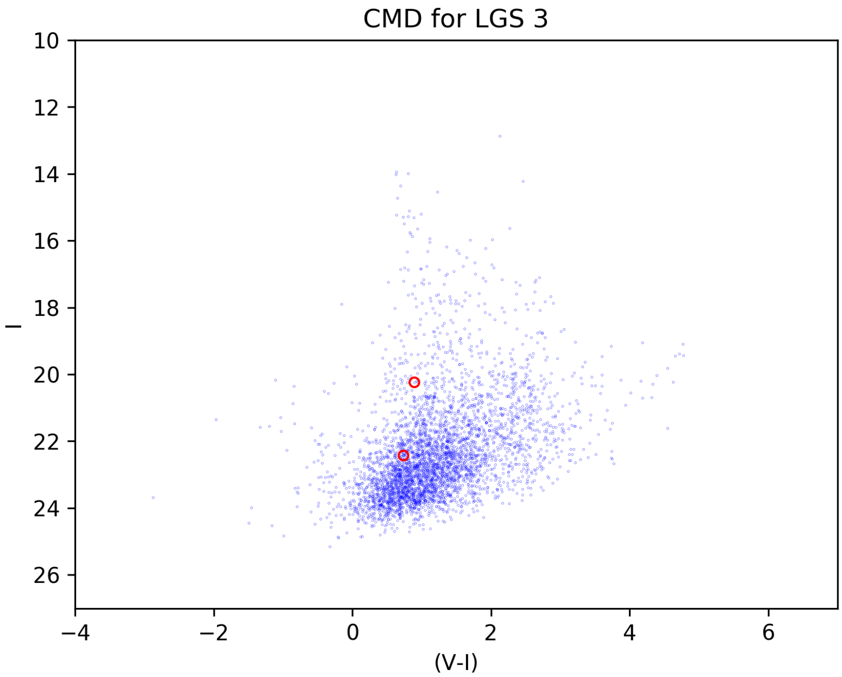

Figure 4.18: CMD for LGS 3 VLT data (blue) with Spitzer variable sources (red).

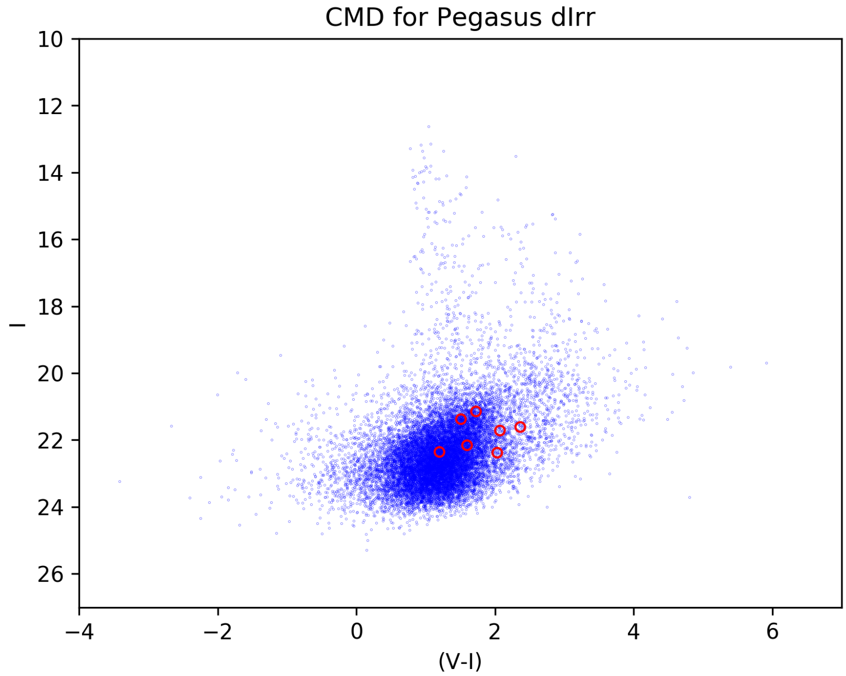

Figure 4.19: CMD for Pegasus dIrr VLT data (blue) with Spitzer variable sources (red).

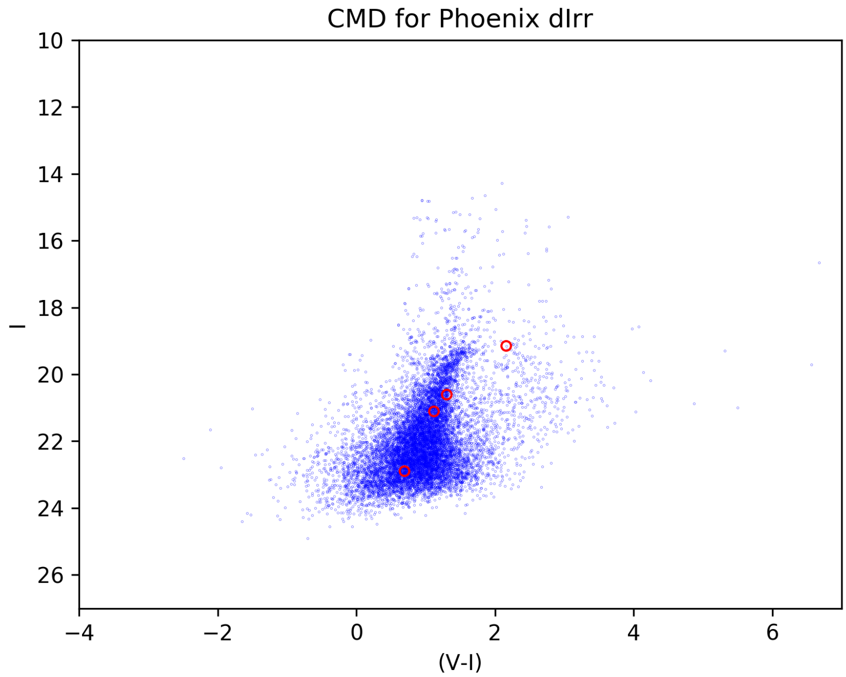

Figure 4.20: CMD for Phoenix dIrr VLT data (blue) with Spitzer variable sources (red).

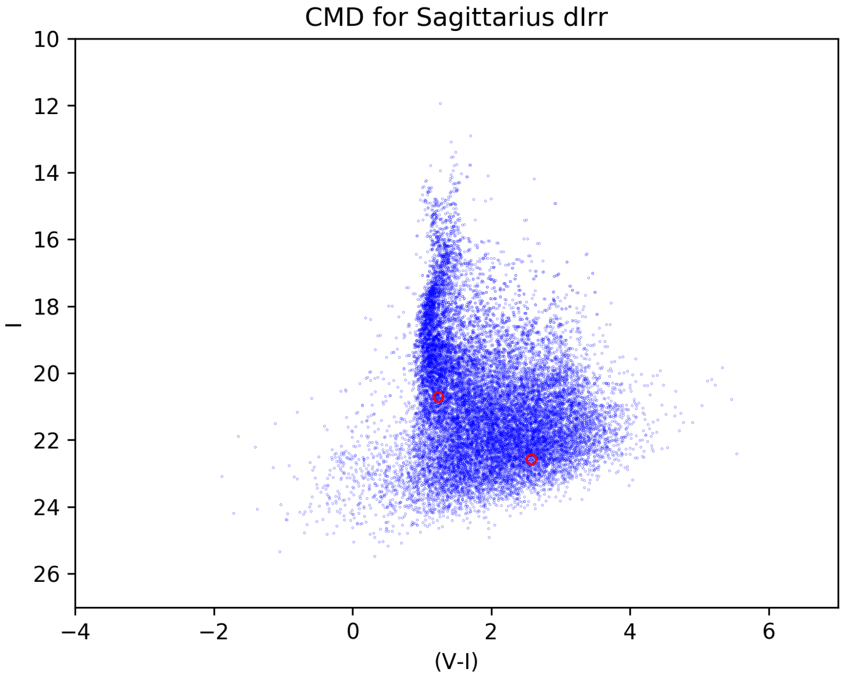

Figure 4.21: CMD for Sagittarius dIrr VLT data (blue) with Spitzer variable sources (red).

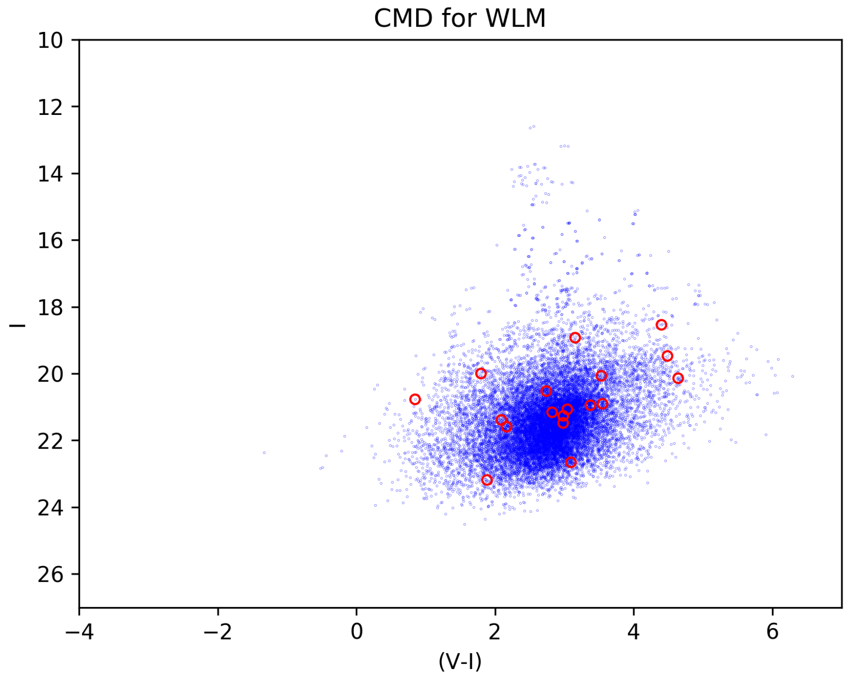

Figure 4.22: CMD for WLM VLT data (blue) with Spitzer variable sources (red).

It is possible that the variability of these sources placed them below the sensitivity limit for the VIMOS instrument at the time of the observations. This high variability may explain the large spread of these variable sources in the diagrams. Variable source data from Menzies, Whitelock & Feast (2015) was used to check if large variability could explain this spread in IC 1613 (Figure 4.17). Data for these sources are shown in Table 4.4. Note that the second item in Table 4.4 is identified as carbon rich.

Table 4.4: Data for large variability sources in IC 1613. Data presented is from this survey, but the sources were crossmatched with Menzies, Whitelock & Feast (2015) to verify this variability.

RA (Degrees)	Dec (Degrees)	I-band (mag)	V-band (mag)
16.223565	2.1343505	23.474	25.018
16.181785	2.088517	23.078	24.042

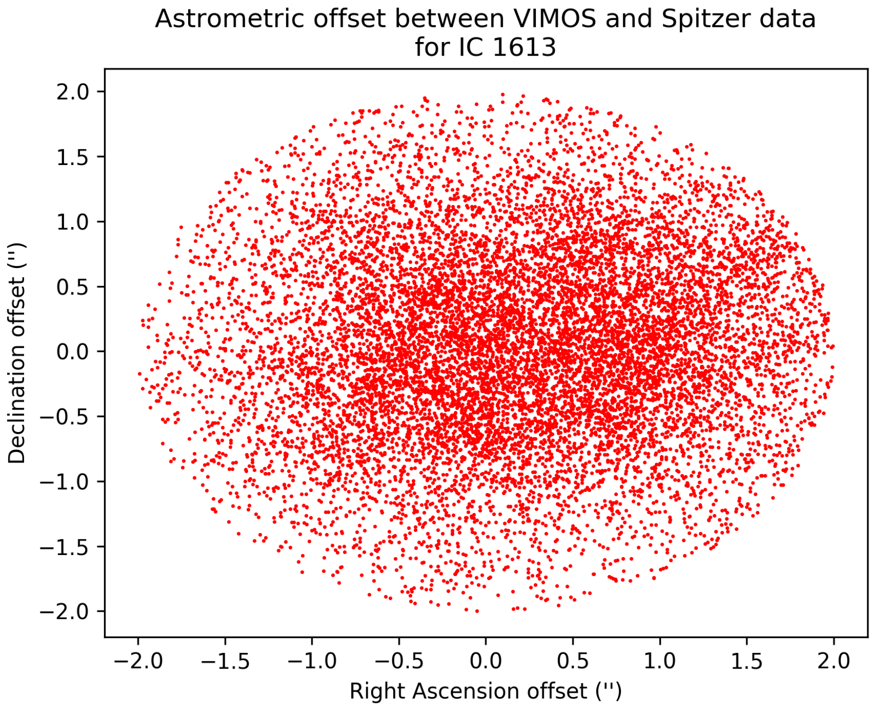

Figure 4.23: Astrometric offset comparison for crossmatched VLT and *Spitzer* data for IC 1613. Both axes are represented in arcseconds.

4.2.2 Astrometry with External Datasets

Comparing this data to an external dataset would provide a more reliable estimation of any astrometric offset. This was performed with the crossmatched VLT-*Spitzer* dataset (Figures 4.23 to 4.24). It is possible to see from these plots that the two astrometric calibrations are in good agreement within the order of approximately $0.2''$ to $0.5''$. This compares well to the offset in the V and I-band data. The substantial scatter in the offsets of individual stars of Figures 4.23 and 4.24 is primarily due to the large PSF of the *Spitzer* IRAC instrument and source blending within the galaxies.

Any astrometric offset will impact crossmatching processes internally in the VLT dataset and with any external catalogues. As the offset is relatively small when comparing the VLT and *Spitzer* data it is unlikely to have caused any severe source mismatching with these two datasets.

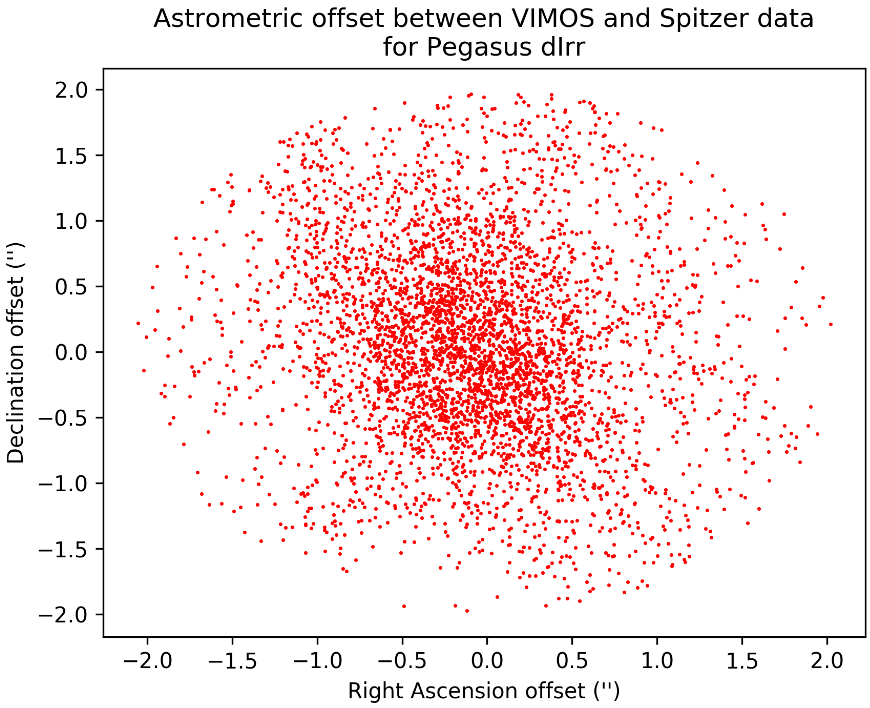

Figure 4.24: Astrometric offset comparison for crossmatched VLT and *Spitzer* data for Pegasus dIrr. Both axes are represented in arcseconds.

Comparing the VLT data coordinates to a further reliable external dataset was also carried out to verify this comparison. The Sloan Digital Sky Survey (SDSS) (Alam et al. 2015) was chosen as the reliable external dataset for this comparison. This data was crossmatched with the VIMOS dataset in the same way as with the *Spitzer* data, albeit with a reduced radius of $0.7''$. It is clear that the plots for IC 1613 (Figure 4.25) and Pegasus dIrr (Figure 4.26) agree well with the previous offset comparisons. Confirmation of the offset of approximately $0.2''$ with such an astrometrically accurate dataset indicates that the coordinates retrieved for the VLT data are accurate enough to be used in comparison to other data sets. This reliability is important in order to achieve the main aim of this project as it allows the results to be compared at other wavelengths or even in follow up studies with other missions.

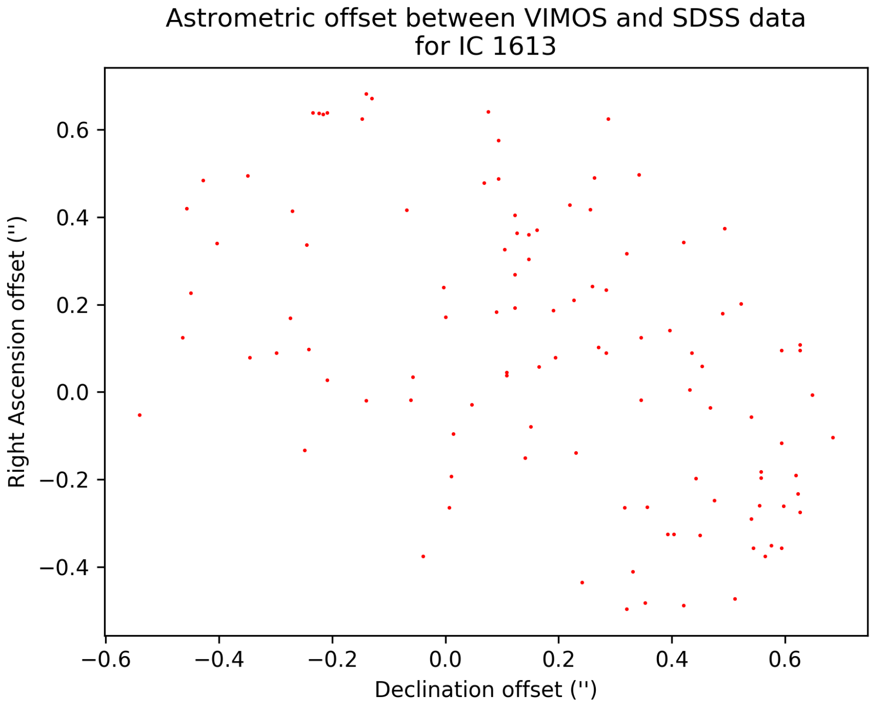

Figure 4.25: Astrometric offset comparison for crossmatched VLT and SDSS data for IC 1613. Both axes are represented in arcseconds.

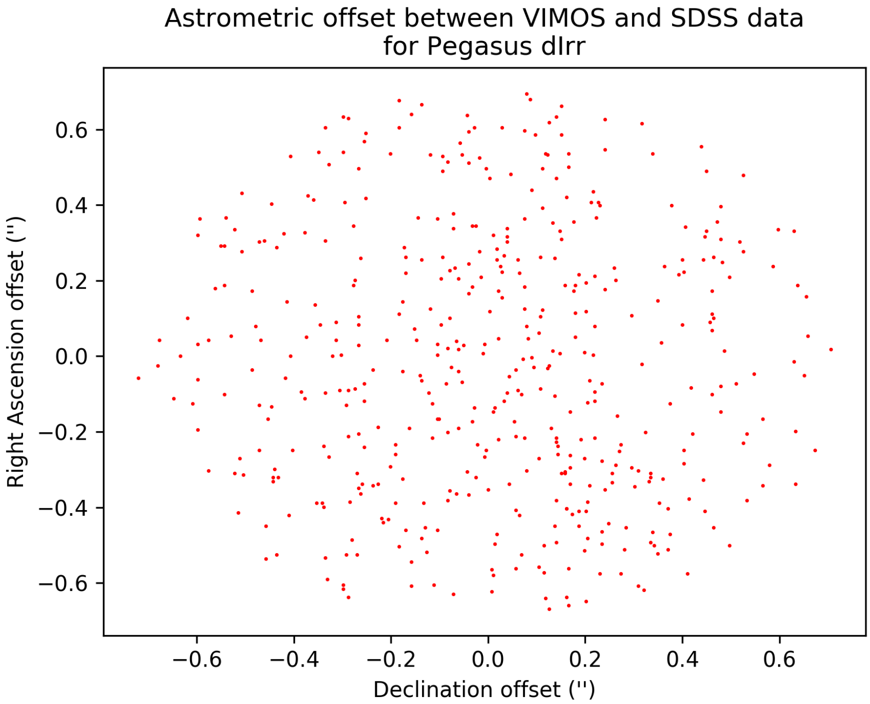

Figure 4.26: Astrometric offset comparison for crossmatched VLT and SDSS data for Pegasus dIrr. Both axes are represented in arcseconds.

4.3 Survey Depth

In order to assess the depth of this survey, histograms of objects counts were plotted against both I-band and V-band magnitude. In order to make direct comparisons to other data sets they were also plotted with the crossmatched DUSTiNGS data. These histograms are shown in Figures 4.27 and 4.28. Note that for NGC 6822 there was no DUSTiNGS data available. It is possible to see in all cases that more data for each galaxy was collected with the VLT compared to *Spitzer* with respect to the target fields. For Sagitarius we can see another demostration of the foreground detection probelm as there are greater number of brighter stars than in most other galaxies.

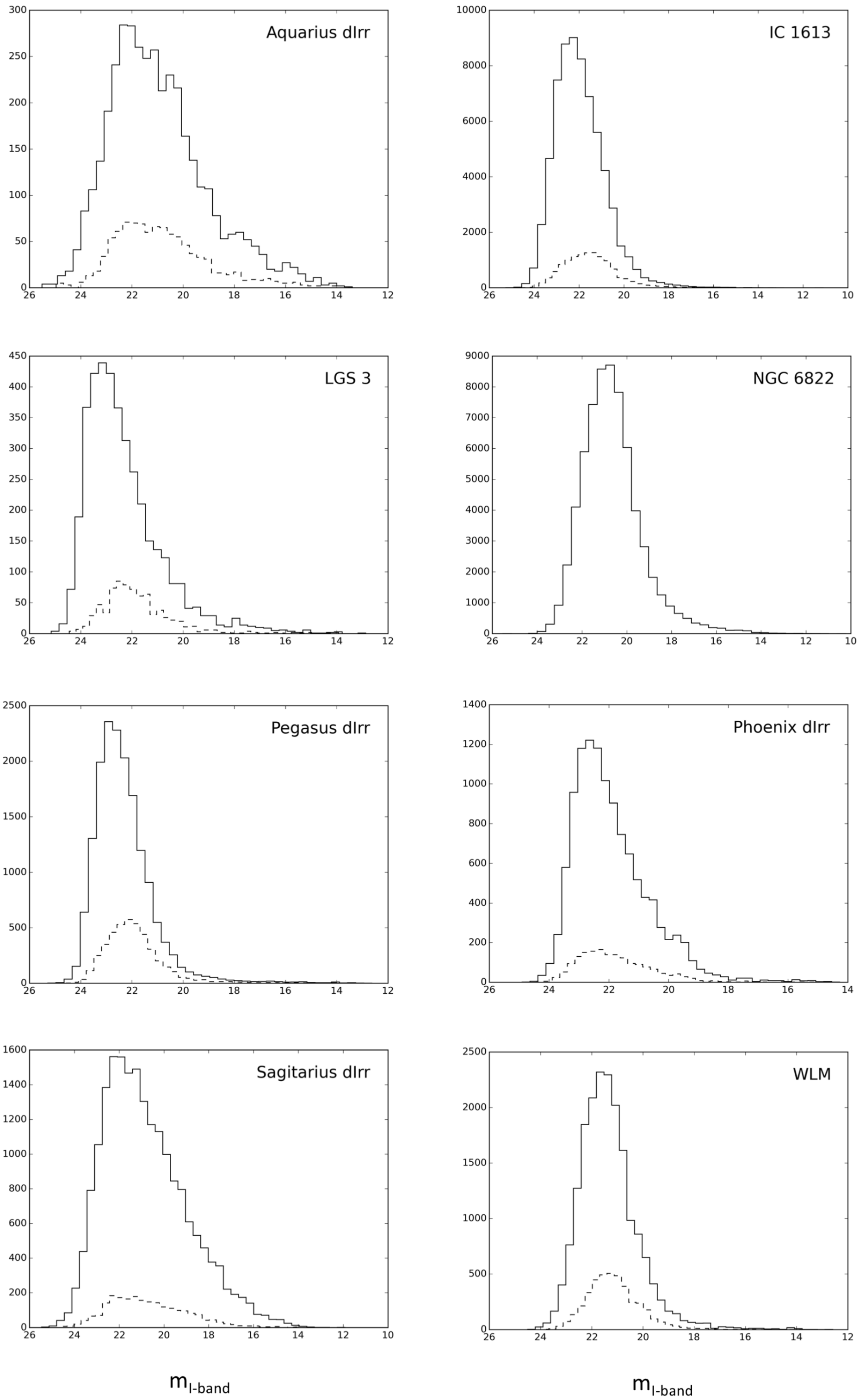

Figure 4.27: VLT survey depth for I-band data (solid line). Also shown is the cross-matched *Spitzer* data (dashed line).

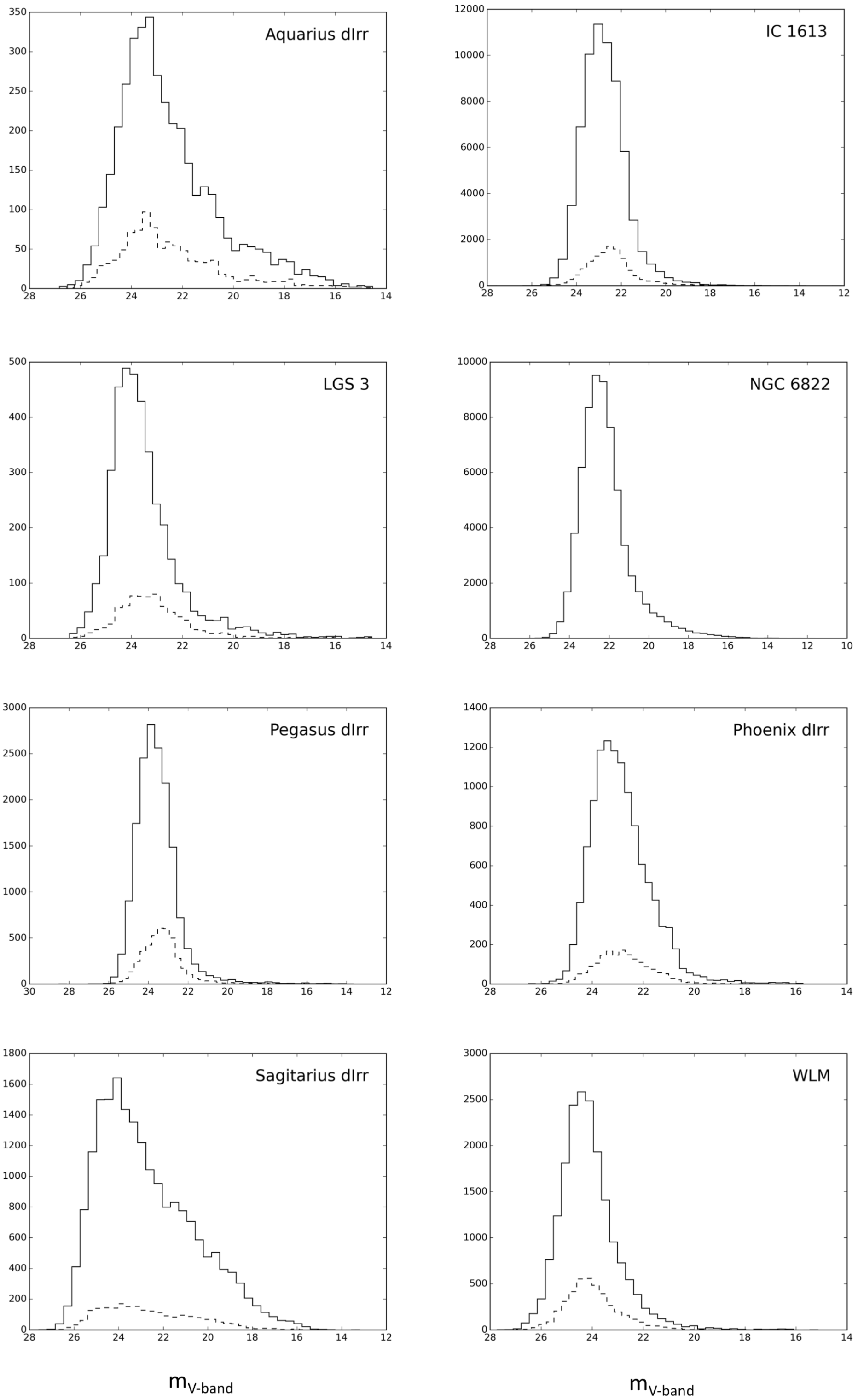

Figure 4.28: VLT survey depth for V-band data (solid line). Also shown is the cross-matched *Spitzer* data (dashed line).

Chapter 5

Conclusions

The observations carried out in this work will greatly assist those wishing to understand the aforementioned environments, in the form of a catalogue of 241,999 point sources. For all of the observed galaxies, with the exception of NGC 6822, data was cross-matched with that from *Spitzer* taken by the infrared *Spitzer* DUSTiNGS survey. This has allowed checks for variable and reddened stars in the VIMOS dataset. Sensitivity limits in these observing bands are estimated to be $V \sim 24$ mag and $I \sim 22$ mag. Astrometric offsets were calculated to be approximately $0.2''$ between the V and I-band data and when compared to external datasets. Data were photometrically calibrated against existing surveys and were in good agreement when compared to each other.

Selection effects and errors are important, and discussed in regards to this data set. Photometry would be improved by the use of point-spread function (PSF) photometry. Further quantification of sensitivity and false detections, via false star tests, would help to refine the techniques used and may indicate where improvements can be made.

The difficulties of making observations of metal-poor stars are largely overcome by using nearby dwarf galaxies where stars are easily resolvable and where their host galaxies are undergoing slow chemical evolution. The large populations of giant branch stars in dwarf galaxies will help us to better understand these poorly understood stages, and develop an understanding of how early galaxies evolved. By extension, these observations will allow us to better understand the metal-production processes that occurred in the early Universe, further increasing our understanding of how our modern Universe evolved.

Overall, this work, and by extension the catalogue produced here, will further our understanding of late-stage stellar evolution in metal-poor environments. Those wishing to study high-redshift environments and their evolution will also gain use from this data as an analogue of galaxies in the early Universe. This data would also be useful when used in conjunction with further studies such as an input to spectral energy distribution analysis of AGB stars, comparing the evolution of mass loss and third dredge-up in AGB stars, or as a catalogue for follow up studies with the highly anticipated *James Webb Space Telescope*.

References

Alam S. et al., 2015, The Astrophysical Journal Supplement Series, 219, 12

Aparicio A., Gallart C., 1995, The Astronomical Journal, 110, 2105

Bertin E., Arnouts S., 1996, Astronomy & Astrophysics Supplement, 117, 393

Bhardwaj A., Kanbur S. M., Macri L. M., Singh H. P., Ngeow C.-C., Wagner-Kaiser R., Sarajedini A., 2016, The Astronomical Journal, 151, 88

Bianchi L., Efremova B., Hodge P., Massey P., Olsen K. A. G., 2012, The Astronomical Journal, 143, 74

Bladh S., Höfner S., Nowotny W., Aringer B., Eriksson K., 2013, Astronomy & Astrophysics, 553, A20

Boyer M. L. et al., 2015a, The Astrophysical Journal, 800, 51

Boyer M. L. et al., 2015b, The Astrophysical Journal Supplement Series, 216, 10

Boyer M. L., Skillman E. D., van Loon J. T., Gehrz R. D., Woodward C. E., 2009, The Astrophysical Journal, 697, 1993

Burbidge E. M., Burbidge G. R., Fowler W. A., Hoyle F., 1957, Reviews of Modern Physics, 29, 547

Busso M., Gallino R., Wasserburg G. J., 1999, Annual Review of Astronomy and Astrophysics, 37, 239

Busso M., Wasserburg G. J., Nollett K. M., Calandra A., 2007, The Astrophysical Journal, 671, 802

Caltech, 2015, IRAC Instrument Handbook

Chattopadhyay T., Debsarma S., Karmakar P., Davoust E., 2015, New Astronomy, 34, 151

Cole A. A., Weisz D. R., Dolphin A. E., Skillman E. D., McConnachie A. W., Brooks A. M., Leaman R., 2014, The Astrophysical Journal, 795, 54

Danilovich T. et al., 2015, Astronomy & Astrophysics, 581, A60

Davidge T. J., 2003, Publications of the Astronomical Society of the Pacific, 115, 635

de Boer T. J. L. et al., 2012, Astronomy & Astrophysics, 544, A73

de Boer T. J. L., Tolstoy E., Lemasle B., Saha A., Olszewski E. W., Mateo M., Irwin M. J., Battaglia G., 2014, Astronomy & Astrophysics, 572, A10

Dell'Agli F., Di Criscienzo M., Boyer M. L., García-Hernández D. A., 2016, Monthly Notices of the Royal Astronomical Society, 460, 4230

Dolphin A. E., 2000, The Astrophysical Journal, 531, 804

Dolphin A. E. et al., 2001, The Astrophysical Journal, 550, 554

ESO, 2015, VIMOS User Manual

ESO, 2016, VIMOS Pipeline User Manual

ESO, 2018, VIMOS trending system: FULL report

Fishlock C. K., Karakas A. I., Stancliffe R. J., 2014, Monthly Notices of the Royal Astronomical Society, 438, 1741

Gallart C., Aparicio A., Bertelli G., Chiosi C., 1996, The Astronomical Journal, 112, 2596

Gallart C., Aparicio A., Vilchez J. M., 1996, The Astronomical Journal, 112, 1928

Graham A. W., 2013, Planets, Stars and Stellar Systems, Oswalt T. D., Barstow M. A., eds., Vol. -1. Springer Netherlands, Dordrecht, pp. 91–140

Grebel E. K., Gallagher III J. S., Harbeck D., 2003, The Astronomical Journal, 125, 1926

Han M., Hoessel J. G., Gallagher, J. S. I., Holtsman J., Stetson P. B., 1997, The Astronomical Journal, 113, 1001

Herwig F., 2000, Astronomy & Astrophysics, 08, 19

Herwig F., 2005, Annual Review of Astronomy and Astrophysics, 43, 435

Hidalgo S. L., Aparicio A., Martínez-Delgado D., Gallart C., 2009, Astrophysics and Space Science, 284, 595

Hidalgo S. L. et al., 2011, The Astrophysical Journal, 730, 14

Hidalgo S. L. et al., 2013, The Astrophysical Journal, 778, 103

Higgs C. R. et al., 2016, Monthly Notices of the Royal Astronomical Society, 458, 1678

Hunter D. A., Elmegreen B. G., 2004, The Astronomical Journal, 128, 2170

Kahn F. D., 1983, IN: Planetary nebulae; Proceedings of the Symposium, 305

Karakas A. I., Lattanzio J. C., 2014, Publications of the Astronomical Society of Australia, 31, e030

Karttunen H., 2007, Fundamental Astronomy, Karttunen H., Kröger P., Oja H., Poutanen M., Donner K. J., eds., Vol. 261. Springer Berlin Heidelberg, Berlin, Heidelberg, p. 510

Kippenhahn R., Weigert A., Weiss A., 2012, Stellar Structure and Evolution, Astronomy and Astrophysics Library. Springer Berlin Heidelberg, Berlin, Heidelberg, p. 468

Kirby E. N., Bullock J. S., Boylan-kolchin M., Kaplinghat M., Cohen J. G., 2014, Monthly Notices of the Royal Astronomical Society, 439, 1015

Kirby E. N., Cohen J. G., Guhathakurta P., Cheng L., Bullock J. S., Gallazzi A., 2013, The Astrophysical Journal, 779, 102

Kirby E. N., Rizzi L., Held E. V., Cohen J. G., Cole A. A., Manning E. M., Skillman E. D., Weisz D. R., 2016, The Astrophysical Journal, 834, 9

Lattanzio J. C., Wood P. R., 2004, in Asymptotic Giant Branch Stars, Habing H. J., Olofsson H., eds., Springer New York, New York, NY, pp. 23–104

Layden A. C., Sarajedini A., 2000, The Astronomical Journal, 119, 1760

Leaman R., Cole A. A., Venn K. A., Tolstoy E., Irwin M. J., Szeifert T., Skillman E. D., McConnachie A. W., 2009, The Astrophysical Journal, 699, 10

Maercker M. et al., 2012, Nature, 490, 232

Marigo P., Girardi L., Bressan A., Groenewegen M. A. T., Silva L., Granato G. L., 2008, Astronomy & Astrophysics, 482, 883

Mateo M., 1998, Annual Review of Astronomy and Astrophysics, 36, 435

Matrozis E., Stancliffe R. J., 2017, Astronomy & Astrophysics, 606, A55

McDonald I. et al., 2011, Monthly Notices of the Royal Astronomical Society, 417, 20

McDonald I., Zijlstra A. A., 2015, Monthly Notices of the Royal Astronomical Society, 448, 502

McDonald I., Zijlstra A. A., 2016, The Astrophysical Journal, 823, L38

Menzies J. W., Whitelock P. a., Feast M. W., 2015, Monthly Notices of the Royal Astronomical Society, 452, 910

Meynet G., Maeder A., 2002, Astronomy & Astrophysics, 390, 561

Miller B. W., Dolphin A. E., Lee M. G., Kim S. C., Hodge P., 2001, The Astrophysical Journal, 562, 713

Minniti D., Zijlstra A. A., 1996, The Astrophysical Journal, 467, L13

Momany Y., Held E. V., Saviane I., Rizzi L., 2002, Astronomy & Astrophysics, 384, 393

Norris B. R. M. et al., 2012, Nature, 484, 220

Ohyama Y., Hota A., 2013, The Astrophysical Journal, 767, L29

Oswalt T. D., Barstow M. A., 2013, Planets, stars and stellar systems volume 4: Stellar structure and evolution. pp. 1–794

Prialnik D., 2009, An Introduction to the Theory of Stellar Structure and Evolution. Cambridge University Press, p. 276

Roederer I. U., Karakas A. I., Pignatari M., Herwig F., 2016, The Astrophysical Journal, 821, 1

Ryan S. G., Norris J. E., Beers T. C., 1996, The Astrophysical Journal, 471, 254

Schaye J. et al., 2015, Monthly Notices of the Royal Astronomical Society, 446, 521

Schlafly E. F., Finkbeiner D. P., 2011, The Astrophysical Journal, 737, 103

Schruba A. et al., 2017, The Astrophysical Journal, 835, 278

Skillman E. D. et al., 2014, The Astrophysical Journal, 786, 44

Sweigart A. V., Mengel J. G., 1979, The Astrophysical Journal, 229, 624

Szigeti L. et al., 2018, Monthly Notices of the Royal Astronomical Society, 474, 4810

Tatton B., Cioni M.-r., Irwin M., 2011, ASP Conference Series, 445, 2004

Taylor M. B., 2006, Astronomical Data Analysis Software and Systems XV - ASP Conference Series, 351, 666

Tully R. et al., 2013, The Astronomical Journal, 146, 86

Udalski A., Wyrzykowski, Pietrzyński G., Szewczyk O., Szymański M., Kubiak

M., Soszyński I., Zebruń K., 2001, Acta Astronomica, 51, 221

Valenti E., Ferraro F. R., Origlia L., 2004, Monthly Notices of the Royal Astronomical Society, 354, 815

Willson L. A., 2000, Annual Review of Astronomy and Astrophysics, 38, 573

Young L. M., Lo K. Y., 1997, The Astrophysical Journal, 490, 710

The End